Single-electron charging using atomic force microscopy

a dissertation presented
by
Antoine Roy-Gobeil
to
The Department of Physics

in partial fulfillment of the requirements
for the degree of
Doctor of Philosophy
in the subject of
Physics

McGill University
Montréal, Québec, Canada
December 2016

Thesis advisor: Professor Peter Grütter Antoine Roy-Gobeil

Single-electron charging using atomic force microscopy

Abstract

The ability of nanostructures to confine electrons at discrete energy levels makes them a promising platform for novel applications in chemistry, optics and information processing. However, these new exciting possibilities come with huge challenges associated with accessing and characterizing objects at the nanometer scale. The general objective of this thesis is to extend the use of atomic force microscopy (AFM), a technique known for resolving the force of individual atoms on a surface, to investigate single-electron charging of various nanostructures. My specific goal was to develop a technique to measure the electronics properties of nanostructure through tunnelling rate measurements, starting with (i) large metallic grains, where the charge becomes discrete although the electron energy level spacing is negligible, to (ii) quantum dots (QDs), where the reduced dimensionality leads to clear energy level spacing, and finally to (iii) organometallic molecules, where the system reorganizes to a different configuration upon the addition of an electron.

In the first chapters, I review the theoretical background of single-electron charging of a quantum dot electrostatically coupled with a mechanical oscillator and provide an efficient algorithm to calculate the response of the coupled electro-mechanical system using linear response theory. I then show that such system can be realized experimentally by using a low-temperature AFM operating at a temperature of 4 K. A simple design using a single-fiber to both excite a cantilever beam and detect its motion by interferometry is proposed. I also show that a calibration of the transfer function of the excitation system is necessary in order to accurately measure forces from measured spectra. Moreover, I demonstrate that nanostructures need to be embedded in a single tunnel junction to adequately examine them with AFM. The description of a low cost, wet lab approach developed to electrically insulate gold nanoparticles from a gold back-electrode by chemisorbing them on a self-assembled monolayer of alkanethiols is also included in this thesis.

One of the key contributions of the present work resides in chapter 5. In this chapter, theoretical and experimental studies of the effect of the density of states of a QD on the rate of single-electron tunneling that can be directly measured by electrostatic force microscopy (e-EFM) experiments are then exposed. In e-EFM, the motion of a biased atomic force microscope cantilever tip modulates the charge state of a QD in the Coulomb blockade regime. The charge dynamics of the dot, which is detected through its back-action on the capacitively coupled cantilever, depends on the tunneling rate of the QD to a back-electrode. The density of states of the QD can therefore be measured through its effect on the energy dependence of tunneling rate. Experimental data on individual 5 nm colloidal gold nanoparticles that exhibit a near continuous density of state at 77 K are presented. In contrast, analysis of already published data on self-assembled InAs QDs at 4 K clearly reveals discrete degenerate energy levels.

In the last chapter of this thesis, I exhibit early results showing for the first time that the reorganization energy of nanostructures upon charging can be measured through its unique effect on the response of the AFM at different oscillation amplitudes of the cantilever. First experimental accounts of that effect are provided by performing single-electron charging of ferrocene ($Fe(C_5H_5)_2$) molecules.

Thesis advisor: Professor Peter Grütter Antoine Roy-Gobeil

Single-electron charging using atomic force microscopy

RÉSUMÉ

La capacité des nanostructures à confiner des électrons à des niveaux discrets d'énergie leur confère un attrait prometteur de nouvelles applications en chimie, en optique et dans le traitement de l'information. Cependant, ces nouvelles possibilités ne sont pas exemptes de défis colossaux liés à l'accession et à la caractérisation d'objets à l'échelle nanométrique. L'objectif général de cette thèse est d'étendre l'utilisation de la microscopie à force atomique (MFA), une technique connue pour résoudre la force d'atomes individuels sur une surface, au chargement d'un électron célibataire à des nanostructures variés. Mon but spécifique était de développer une technique pour mesurer par effet tunnel les propriétés électroniques de nanostructures constituées : (i) de larges grains métalliques, où la charge devient discrète bien que l'espacement des niveaux d'énergie de l'électron soit négligeable, (ii) de points quantiques (PQ), où les dimensions réduites mènent à une séparation nette des niveaux d'énergie, et finalement (iii) de molécules organométalliques, où le système se réorganise en une configuration différente suite à l'addition d'un électron.

Dans les premiers chapitres, je revois les fondements théoriques du chargement d'un électron individuel sur un PQ couplé de manière électrostatique à un oscillateur mécanique et propose un algorithme efficace pour calculer la réponse de ce système couplé en utilisant la théorie de la réponse linéaire. Je montre en outre qu'un tel système peut être réalisé expérimentalement avec un MFA à basse température opéré à une température de 4 K. Un montage simple dans lequel une seule fibre optique est utilisée pour exciter un cantilever et détecter son mouvement par interférométrie est proposé. Je montre de plus qu'une calibration de la fonction de transfert du système en excitation est nécessaire pour mesurer adéquatement les forces à partir des spectres obtenus. Par ailleurs, je démontre que les nanostructures doivent être incorporées à une jonction tunnel individuelle pour être examiné adéquatement par MFA. La description d'une approche peu couteuse, réalisable en laboratoire humide, pour isoler électriquement des nanoparticules d'or d'une contre-électrode d'or par sorption chimique sur une monocouche auto-assemblée d'alcanethiols est en outre incluse dans cette thèse.

Une des contributions importantes du présent travail se retrouve au chapitre 5. Dans ce chapitre, des études expérimentales et théoriques de l'effet de la densité des états d'un PQ sur le taux tunnel d'un électron individuel pouvant être mesurée directement par microscopie à force électrostatique (e-MFE) sont exposés. En e-MFE, le mouvement de la pointe d'un cantilever d'un microscope à force atomique biaisé module l'état de charge d'un PQ dans un régime de blocage de Coulomb. La dynamique de charge du point, lequel est détecté par rétroaction sur le cantilever capacitivement couplé, dépend du taux tunnel du PQ à la contre électrode. La densité des états du PQ peut ainsi être mesurée par son effet sur la dépendance d'énergie du taux tunnel. Des données expérimentales sur des nanoparticules constituées de colloïdes d'or individuels de 5 nm qui exhibent une densité d'état continue à 77 K sont présentées. Par contre, l'analyse de données publiées antérieurement pour des PQ auto-assemblés d'InAs à 4 K révèle des niveaux discrets d'énergie dégénérés.

Dans le dernier chapitre de cette thèse, je présente des résultats préliminaires qui montrent pour la première fois que l'énergie de réorganisation de nanostructures suite à un chargement peut être mesurée par son effet unique sur la réponse du MFA à différentes amplitudes d'oscillation. Des données expérimentales originales témoignant de cet effet sont obtenues par le chargement d'un électron individuel sur des molécules de ferrocène ($Fe(C_5H_5)_2$).

Acknowledgments

First and foremost, I sincerely thank my supervisor, Professor Peter Grütter, for giving me the opportunity to join his laboratory and to work on exciting research projects. I am particularly grateful for his constant support and for the freedom he gave me to extend my scientific knowledge and develop my intellectual and technical skills set. It's always been stimulating to discuss with you, Peter, especially during our regular Monday morning meetings. I greatly benefit from your vast expertise in science and technology and from your advices that go beyond science. I will never forget them.

I express my deepest appreciation to Dr. Yoichi Miyahara, with whom I had the tremendous pleasure to work on a daily basis since I joined the Grütter group. The countless stimulating scientific discussions we had greatly contributed to keep me interested and motivated throughout the years. You've been, Yoichi, an indispensable collaborator when the time came to comment my documents and to repair or improve the low-temperature atomic force microscope. Even during difficult times, your positive attitude was the one constant I could always count on.

My acknowledgment also goes to Professor Paul McEuen from Cornell University, and to Professors Aashish Clerk, Mark Sutton, Thomas Szkopek, and David Hanna from McGill, who took the time to review and comment my thesis and to challenge me during my defence. This was very much appreciated. I want to give special thanks to Professor Aashish Clerk for his relevant critical comments of my theoretical interpretation of some of my experimental results.

I am grateful to Professor Hanadi Sleimann and to her Ph.D. student, Kai Lin Lau, for sharing their expertise in self-assembly and welcoming me to their laboratory in the Chemistry Department. I also acknowledge the NSERC's CREATE Training Program in Bionanomachines from which I received a scholarship grant during the course of my doctoral studies.

The help and encouragement of my early colleagues at McGill, Lynda Cockins, Aleks Labuda and William Paul, were also extremely precious. At the beginning of my work, Lynda taught me with patience how to operate the home-built low-temperature AFM, which truly intimidated me at first, and Aleks identified instrumental artefacts that proved important in my work. William has always provided me invaluable advices, encouragements and friendship. I also thank all the other members of the Grütter group, present and past, with whom I had the pleasure to work and to share numerous enjoyable moments and social activities.

The technical support of dedicated people behind the scene was key to the success of my experiments, particularly John Smeros and Robert Gagnon, who helped me with the maintenance of the vacuum systems, the evaporation of gold thin films and the installation of a glovebox in the Rutherford building. Two visiting students, Tomohisa Shinozaki and Masaki Oishi, contributed to the preparation of a large number of high quality optic fibers for the microscope's interferometer, and four undergraduate students from McGill, Peter Zhi, Sebastian Bramberger, Xin Yuan Zhang and Junan Lin, participated actively to my experimental work. Many thanks to them!

Lastly, I sincerely express my gratitude to Karl, Andrée, and Frédéric, my dear brother, for their indefectible support, as well as to my mom and dad for all their love and encouragement.

Antoine
McGill University
December 2016

Statement of originality

The following aspects of this thesis represent original knowledge advancements. So far, one of these findings has been published.

- Tunneling rate spectroscopy using atomic force microscopy was performed to extract information on the density of states of individual Au nanoparticles (classical dots) as well as orbital degeneracies and shell filling of individual InAs quantum dots (Roy-Gobeil A., Y. Miyahara Y. and P. Grutter, 2015, Nano Letters, 15(4):2324– 2328, doi: 10.1021/nl504468a; chapter 5).
- Photothermal excitation and cantilever detection were integrated in a single optical fiber to perform low-temperature AFM experiments (chapter 3).
- The theory of single-electron force microscopy was extended to account for the reorganization energy of organometallic molecules (chapter 6). Early results show for the first time the unique effect of the reorganization energy of an organometallic nanostructure ($Fe(C_5H_5)_2$) upon charging on the response of the AFM at different oscillation amplitudes of the cantilever (chapter 6).
- An efficient algorithm to calculate the response of the coupled electro-mechanical system using linear response theory is proposed (chapter 2).

Contributions of co-authors

This thesis is based on a published article prepared with co-authors Yoichi Miyahara (Y.M.) and Peter Grütter (P.G) and on results that have not yet been published. I conducted the sample preparation, data collection and data analysis, and I am the lead author of all chapters. I gratefully acknowledge the support and assistance of P. G. and Y.M. whose contributions are summarized below:

- In Section 2.3, Y.M. was involved in developing the numerical algorithm and testing my various implementations.
- In Chapter 3, Y.M. implemented the electronic circuit to perform photothermal excitation and cantilever detection in a single optical fiber design. Both Y.M. and P.G. were involved in data analysis and discussions regarding the design of the system. P.G. supervised the project.
- In Chapter 4, Y.M. was involved in data collection and provided technical support on the experimental apparatus. Both Y.M. and P.G. were involved in data analysis and discussions regarding the experimental protocol and presentation of data. P.G. supervised the project.
- The text in Chapter 5 is based a published article (Antoine Roy-Gobeil, Yoichi Miyahara, and Peter Grutter, Revealing Energy Level Structure of Individual Quantum Dots by Tunneling Rate Measured by Single-Electron Sensitive Electrostatic Force Spectroscopy, *Nano Letters*, **15(4)**, pp 2324–2328, **2015**). Y.M. provided technical support on the experimental apparatus. Both Y.M. and P.G. were involved in discussions regarding the research concepts, presentation of data as well as manuscript preparation. P.G. supervised the project.
- In Chapter 6, Y.M. provided technical support on the experimental apparatus. Both Y.M. and P.G. were involved in discussions regarding the research concepts, presentation of data as well as manuscript preparation. P.G. supervised the project.

Contents

Listing of figures

Je dédie cette thèse à mes chers parents Françoise et Charles.

...I wish to give an account of some investigations which have led to the conclusion that the carriers of negative electricity are bodies, which I have called corpuscles, having a mass very much smaller than that of the atom of any known element, and are of the same character from whatever source the negative electricity may be derived

Joseph John Thomson from his Nobel Prize Award Address, 1906

1

Introduction

The granularity of electrons was discovered at the end of the 19th century by Joseph John Thomson for which he was awarded a Nobel Prize in 1906. Thomson made the first estimates of both the charge and the mass of single electrons which he referred to as "corpuscles". However, it took until the 1980's before the possibility to control the movement and the position of a single electron was demonstrated in a solid state system[100]. By confining electrons in a small region of space, which we refer to as a dot, Coulomb repulsion become appreciable thus enabling precise control of the number of electrons in the dot. By reducing the size of the dot further, it becomes zero-dimensional and its electronic states are discrete just like those in atoms. The emergence of single-electron charging effects and of atom-like discrete energy levels at the nanoscale has huge potential for novel applications in optics, chemistry and information processing.

Tremendous progress has been made in the ability to control electron transport in mesoscopic or low dimensional system (Grabert and Devoret[40], Sohn et al.[84]), thanks in part to the relentless miniaturization of lithographic techniques which enables the patterning of sub-micron size electrodes. On the other hand, much less measurements of single-electron charging of self-assembled nanostructures such as small metallic grains, quantum dots (QD) and individual molecules have been performed. The main challenge in the experimental investigation of those nanostructures lies in the ability to probe them individually because of their small size (< 5 nm) which makes it difficult to place electrodes nearby. However, there is a huge potential upside to self-assembly which promises high throughput fabrication of structures smaller than what is achievable with standard lithographic technique. The smaller sizes attainable lead to large charging energies enabling potential single-electronics devices to operate at ambient temperature.

The difficulty associated with measurements of electron transport in small nanostructures is alleviated by the use of scanning probe microscopy (SPM) in which a sharp tip can be brought near a surface with sub-nm precision to both image individual QDs and perform spectroscopy at the nanoscale. By using the probe as an electrode to measure tunneling current, a technique called scanning tunneling microscopy, conductance measurements on individual QDs can be performed using a double tunnel barrier setup as illustrated in Figure 1.1 (left panel). The drawback of this technique is that the tip must be brought extremely close to the QD to achieve appreciable tunnel current, thus perturbing the QD. Another approach is to measure forces instead of a current, a technique called atomic force microscopy (AFM). Using AFM, charge sensing can be performed from larger distances by measuring the capacitive force between the QD and a mechanical oscillator. This approach is less invasive, and, contrarily to STM, can

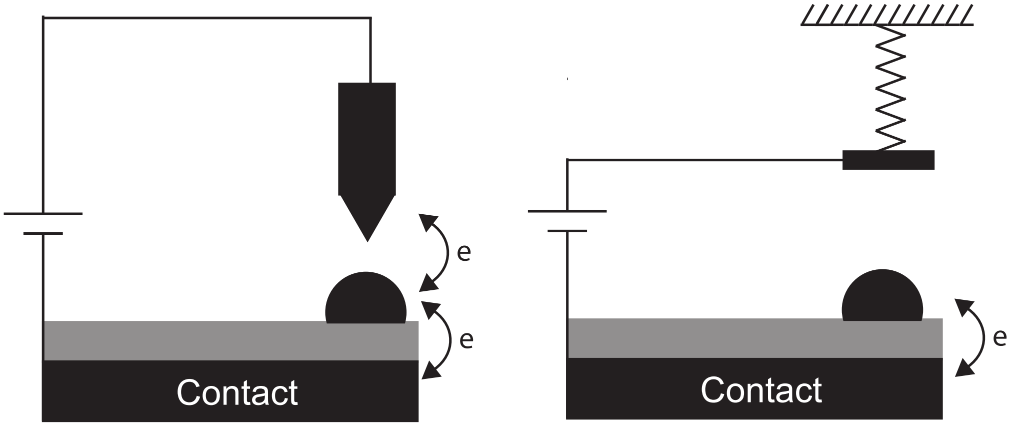

Figure 1.1: Schematic of scanning probe microscopy techniques. Gray layers are tunnel barriers and black arrows illustrate electron tunneling. Left) Schematic of transport measurements performed by scanning tunneling microscopy. A sharp tip can be scanned on a surface and brought extremely close to a nanostructure of interest to perform transport measurement. Right) Schematic of charge sensing measurements performed by atomic force microscopy. A tip is brought in the vicinity of a nanostructure and confined charges are detected through capacitive force acting on a mechanical oscillator.

be used to study buried QDs underneath dirty surfaces as well imaging non-conductive surfaces. By using the probe as a local movable gate and a local electrometer to detect single-electron, the experimental scheme only requires a single tunnel barrier as shown in Figure 1.1 (right panel). Single-electron was first detected with force microscopy by Schönenberger and Alvarado[82] and was later used in a spectroscopic mode to determine the energies by Woodside[105].

The general objective of this work is to advance the capability of atomic force microscopy to quantitatively measure electronic properties of a wide range of nanostructures which are hard to study through conventional transport measurements. My specific goal was to develop a technique to measure the electronic properties of nanostructures through tunneling rate measurements, starting with large metallic grains, where single-electron charging effects become appreciable, to quantum dots, where the reduced dimensionality leads to clear energy level spacing, and finally to molecules, where the electronic structure reorganizes to a different configuration upon the the addition of an electron. In particular, I demonstrate how the energy-dependent tunneling rate can be measured and thus used to determine the energy levels of the QD. Surprisingly, the tunneling rate can be determined by using a well known force measurement method in non-contact AFM by measuring the conservative and dissipative force acting on an oscillating cantilever. This thesis is organized as follows:

- Chapter 2 is a review of the theoretical background of single-electron charging of a quantum dot electrostatically coupled with a mechanical oscillator. As a very useful result, I provide an efficient algorithm to calculate the response of the coupled electro-mechanical system using linear response theory.

- Chapter 3 demonstrates important aspects to experimentally determining the relevant quantities using a low-temperature AFM operating at temperatures down to 4 K. A simple design using a single-fiber to both excite a cantilever beam and detect its motion by interferometry is proposed. I also show in chapter 3 that a calibration of the transfer function of the excitation system is necessary in order to accurately measure force and dissipation from measured spectra. Moreover, I demonstrate that nanostructures need to be embedded in a single tunnel junction to adequately examine them with AFM.

- Chapter 4 then describes a low cost, wet lab approach developed to electrically insulate gold nanoparticles from a gold back-electrode by chemisorbing them on a self-assembled monolayer of alkanethiols.

- Chapter 5 reveals that performing tunneling rate spectroscopy with AFM allows to measure the density of states of self-assembled metallic grains and QDs.

- Chapter 6 presents early results showing for the first time that the reorganization energy of nanostructures upon charging can be measured through its unique effect on the response of the AFM at different oscillation amplitudes of the cantilever. Original experimental accounts of that effect are provided by performing single-electron charging of ferrocene ($Fe(C_5H_5)_2$) molecules.
- Chapter 7 is a summary of the main findings with suggestions for future work in the field.

2

Theory of sequential tunneling

The purpose of this chapter is to present the known body of theory that underlies our experiments in a coherent and comprehensive manner. I will direct the reader to key references but for sake of completeness and clarity I will derive the main equations specific to our experiments. I introduce the relevant concepts, discuss the necessary conditions to observe single-electron charging phenomena and provide the theoretical framework used to understand and analyze experimental data.

2.1 Single-electron charging

Let's consider a cluster of atoms, hereafter referred to as a dot, a grain or a quantum dot, weakly coupled by a tunnel barrier to an electron reservoir in thermal equilibrium. In order to observe the discreteness of electrons and precisely control the number of electrons on the grain, N, two general conditions need to be satisfied.

- Firstly, quantum fluctuations of N must be small for electrons to be well localized on the dot. This is achieved by decoupling the dot from the reservoir with a tunnel resistance, R_T, larger than the quantum resistance, R_K:

  $$R_T \gg R_K = \frac{h}{e^2} \approx 25813\ \Omega \tag{2.1}$$

  where h is the Planck constant and e is the elementary charge.

- Secondly, thermal fluctuations of N must be negligible. This condition if fulfilled if the electrochemical potential of the dot, μ_{dot}, is much larger than the thermal energy:

  $$\mu_{dot} \gg k_B T \tag{2.2}$$

  where k_B is the Boltzmann constant and T is the temperature of the system.

In thermal equilibrium with a large reservoir, the probability to find N electrons in a grain, $P_{eq}(N)$, is given by the grand canonical distribution function[74]:

$$P_{eq}(N) = Z^{-1} \exp(-\frac{1}{k_B T}(F(N) - N\,\mu_{res})) \tag{2.3}$$

where $F(N)$ is the free energy of the grain, μ_{res} is the electrochemical potential of the reservoir and Z is the partition function normalizing the probabilities (i.e. $\sum_N P_{eq}(N)$).

Computing $F(N)$ from first principles can be quite complicated so we resort to several deceptively reasonable assumptions to describe the electrons on the dot which I will outline below.

2.1.1 Electronic description

A quantum-mechanical view is, of course, necessary to describe a system of electrons. Electrons must be considered as intrinsically indistinguishable particles when enumerating the possible quantum states of the system. This is the correct description since statistical behavior of systems of distinguishable particles violates the second law of thermodynamics, a result known as the Gibbs paradox.

The first drastic approximation we make is the assumption that N electrons on the grain can be described as a system of non-interacting quasi particles by lumping all the electron-electron interactions into an electrostatic energy, $U(N)$. This allows the many-particle system to be described in terms of single-particle states k, also referred to as levels, with energies E_k. Levels are labelled in ascending order of energy measured relative to the bottom of the confinement potential. The Hamiltonian of the grain is then:

$$H_{dot} = \sum_k E_k \, c_k^\dagger \, c_k + U(N) \tag{2.4}$$

where $c_k^\dagger$ and c_k are respectively creation and annihilation operators for level k[7]. Because electrons are fermions (particles with half-integer spin), they respect Pauli exclusion principle stating that two identical fermions cannot occupy the same quantum state simultaneously. Therefore, each level can only contain either one or zero electrons ($n_k = 0, 1$). Spin degeneracy can be included by counting each level twice and orbital degeneracies can be included similarly. Therefore, a specific state of the QD is fully specified by the mere enumerations of its occupation numbers $\{n_1, n_2, n_3, ...\} \equiv \{n_i\}$.

We adopt the simple approximation of the orthodox model which treats the electrostatic energy macroscopically in terms of the dot capacitance, C, and an external applied bias, V_B:

$$U(N) = \frac{(N\,e)^2}{2C} + (N\,e)\alpha V_B \tag{2.5}$$

where α is the fraction of the applied bias which drops between the dot and the reservoir[8].

2.1.2 COULOMB BLOCKADE

Single-electron charging are present even if only the electrostatic energy is taken into account in the calculation of the free energy of the dot ($F(N) \approx U(N)$). It is then straightforward to evaluate the average number of electrons on the dot:

$$\langle N \rangle = \sum N P_{eq}(N) \tag{2.6}$$

where P_{eq} is defined in equation 2.3. When the charging energy, E_C, defined as:

$$E_C \equiv e^2/2C \tag{2.7}$$

is much larger than $k_B T$, $P_{eq}(N)$ is non-zero for at most two values of N (see Figure 2.1). In metallic spheres with small radius (and hence small capacitance), Coulomb repulsion results in a large electrostatic energy barrier that must be overcome in order to bring a charge from the reservoir to the dot. This suppression of charge transfer at low bias was first observed in solids by Gorter[38] with small metallic grains and is known as Coulomb blockade of single-electron tunneling.

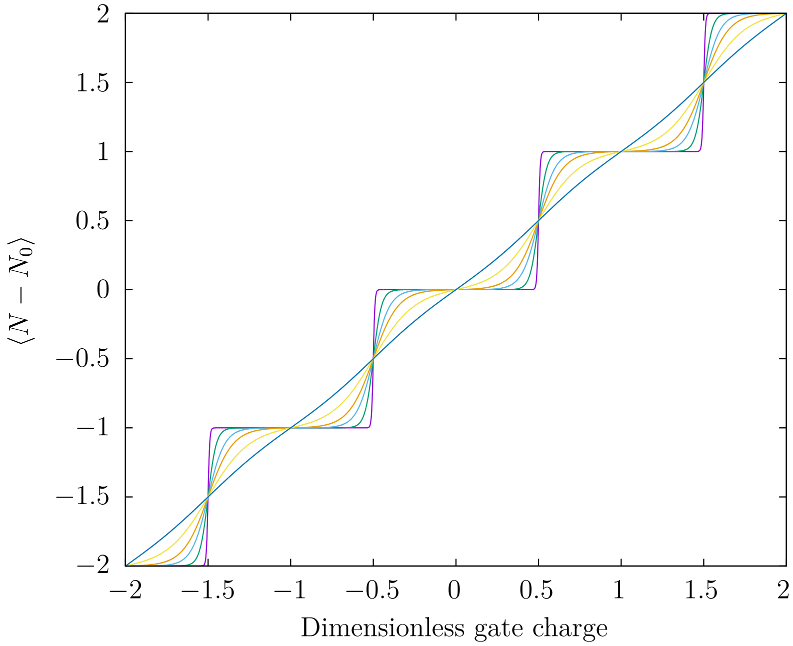

Figure 2.1: Number of electrons $\langle N - N_0 \rangle$ on a metallic grain with charging energy E_C as a function of a gate voltage for different thermal energy ($k_B T$) varying from 0.01 to 0.5 E_C. N_0 is the number of electrons at zero bias.

2.1.3 STATISTICS

The simplicity of the equations in Section 2.1.2 comes from the description of the grain in terms of charge states defined by N. However, in the quantum-mechanical picture, many different states on the grain have N electrons.

The probability of occupation of a particular quantum state of the grain, $\{n_i\}$, with energy, $\varepsilon_{\{n_i\}}$, is, again, given by the grand canonical distribution:

$$P(\{n_i\}) = Z^{-1} \exp\left[\frac{1}{k_B T}\varepsilon_{\{n_i\}} - N\mu_{res}\right]. \tag{2.8}$$

Considering the Hamiltonian of the dot defined in equation 2.4, the partition function, Z, can be written as a sum over all possible realizations of occupation numbers $\{n_i\}$:

$$Z = \sum_{\{n_i\}} \exp\left[-\frac{1}{k_B T}\left(\sum_{k=1}^{\infty} E_k n_k + U(N) - N\mu_{res}\right)\right] \tag{2.9}$$

where $N = \sum_i n_i$. The probability of having N electrons in the dot at equilibrium is then given by the following sum over all possible dot states:

$$P_{eq}(N) = \sum_{\{n_i\}} P(\{n_i\})\delta_{\sum_k n_k, N} \tag{2.10}$$

where δ is the Kronecker delta. By computing $P_{eq}(N)$ for different gate voltages, the periodicity of charging peaks is obtained. Second, the conditional probability of occupation of level k when N electrons are in the dot is:

$$F_{eq}(E_k|N) = \frac{1}{P_{eq}(N)} \sum_{\{n_i\}} P(\{n_i\})\delta_{n_k,1}\delta_{N,\sum_i n_i}. \tag{2.11}$$

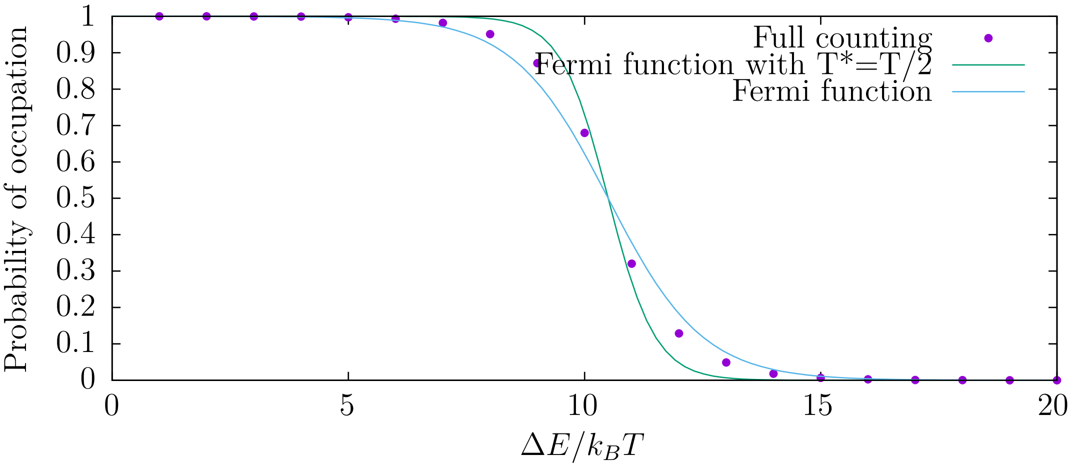

Figure 2.2: Conditional probability of occupation of 20 single-electron states k=1..20 with energies $E_k = k\, k_BT$ when there are 10 electrons in the dot.

The problem of computing the infinite summations in equations 2.10 and 2.11 greatly simplifies when different limits are considered. In the limit of high temperature, where the average energy level spacing between eigenstates, ΔE_{level}, is much smaller than k_BT, the probability of occupation of energy level E_i is given by the Fermi function[74]

$$f(E_i - \mu) = \left[1 + \exp\left(\frac{E_i - \mu}{k_BT}\right)\right]^{-1}. \tag{2.12}$$

Electrons in the reservoir are described in this limit. In the limit of low temperature, i.e. $\Delta E_{level} \gg k_BT$, all the levels below the Fermi level are filled. However, in intermediate temperature regime, a full counting of the states is necessary. In such cases, the Fermi function still coincides well with the full counting albeit with a different effective temperature. An example of such system is shown in Figure 2.2.

2.1.4 Tunneling rate

The dynamic of charge transfer between the dot and the reservoir will now be explored. Because it is already assumed that the tunnel coupling is weak (see Eq. 2.1), the tunneling Hamiltonian is treated as a perturbation and the electron transition rates are given by Fermi's golden rule[100]. The transition rates between a level i in the reservoir and a level k in the dot are given by

$$\Gamma_{i\to k} = \frac{2\pi}{\hbar}|T_{ik}|^2\,\delta(E_i - E_k - \Delta E) \tag{2.13}$$

$$\Gamma_{k\to i} = \frac{2\pi}{\hbar}|T_{ik}|^2\,\delta(E_k - E_i + \Delta E) \tag{2.14}$$

where T_{ik} is the tunnel transmission coefficient, δ is the Dirac delta function enforcing energy conservation, and ΔE is the change in electrostatic energy upon tunneling. The latter is defined by:

$$\Delta E \equiv U(N+1) - U(N) = E_C + \alpha e V_B. \tag{2.15}$$

By assuming that $|T_{ik}|$ is constant over all levels i around the Fermi level, the tunneling rates on, Γ_+, and off the dot, Γ_-, can then be expressed by a single summation over the levels k of the dot. Taking into account Pauli's exclusion principle, they are given by:

$$\Gamma_{+,N}(\Delta E) = \sum_k \frac{2\pi}{\hbar}|T_{ik}|^2 \underbrace{f(E_k + \Delta E)}_{\text{Occupied lead state}} \overbrace{[1 - F_{eq}(E_k|N)]}^{\text{Empty dot state}} \tag{2.16}$$

$$\Gamma_{-,N+1}(\Delta E) = \sum_k \frac{2\pi}{\hbar}|T_{ik}|^2 \underbrace{F_{eq}(E_k|N+1)}_{\text{Occupied dot state}} \overbrace{[1 - f(E_k + \Delta E)]}^{\text{Empty lead state}} \tag{2.17}$$

where $F_{eq}(E_k|N)$ is the conditional probability of occupation of energy level k when N electrons are contained in the QD at equilibrium and $f(E)$ is the Fermi function.

2.1.5 MASTER EQUATION

Previous section provides equations describing the tunneling rate of a single electron across a barrier but does not inform about the statistics of many electrons tunneling. By making two assumptions about the physical process of single electron tunneling, a kinetic equation describing the time evolution of the probability of occupation of the grain out of equilibrium can be obtained.

The first assumption is that electrons have no memory of the past and thus that their tunneling rate only depends on the current state of the system[*]. The second assumption is that the system evolves at random times in a jump like fashion and relaxes quickly to equilibrium. Such system can be described with a master equation[100]:

$$\frac{\partial P_i(t)}{\partial t} = \sum_j [\Gamma_{j\to i} P_j(t) - \Gamma_{i\to j} P_i(t)] \tag{2.18}$$

where $\Gamma_{i\to j}$ denotes the transition rate from state i to state j and $P_i(t)$ is the time dependent occupation probability of state i. Because transitions between states are only possible if they differ by one electron, the non-equilibrium probability, $P(N)$, can be compactly written as:

$$\begin{aligned}\frac{\partial P(N)}{\partial t} =& - P(N)[\Gamma_{+,N}(\Delta E) + \Gamma_{-,N}(\Delta E)] \\ &+ P(N+1)\Gamma_{-,N+1}(\Delta E) \\ &+ P(N-1)\Gamma_{+,N-1}(\Delta E).\end{aligned} \tag{2.19}$$

---

[*] Also known as a Markov process

where the tunneling rates are defined by equations 2.16 and 2.17.

2.1.6 SIMPLIFIED MASTER EQUATION

The problem of solving equation 2.19 can be greatly simplified when only a few values of N are statistically probable. Since the electrochemical potential of the dot, μ_{dot}, is large compared to the thermal energy (see section 2.1), states with different number of charge are well separated in energy. Therefore, under any gating conditions, the number of electrons on the dot can only take two values. Formally, this implies that the tunneling rates leading away from those two charge states are small in comparison to the rates leading towards either states. Naming the two relevant charge states n and $n-1$, it is required that:

$$\begin{aligned} \Gamma_{-,n} &> \Gamma_{+,n} && \text{if } n > N+1 \\ \Gamma_{-,n} &\gg \Gamma_{+,n} && \text{if } n = N+1 \\ \Gamma_{+,n} &\gg \Gamma_{-,n} && \text{if } n = N-2 \\ \Gamma_{+,n} &> \Gamma_{-,n} && \text{if } n > N-2 \end{aligned}$$

which implies that the occupation probabilities $P(N)$ are non-zero only for $N = n, n-1$. By dropping the subscripts N, we can write the simplified master equation describing the time evolution of the probability of having an extra electron on the dot, p, as:

$$\frac{\partial p}{\partial t} = -\Gamma_{-}(\Delta E)\, p + \Gamma_{+}(\Delta E)\,(1-p) \tag{2.20}$$

$$= -p\,\Gamma_{\Sigma}(\Delta E) + \Gamma_{+}(\Delta E) \tag{2.21}$$

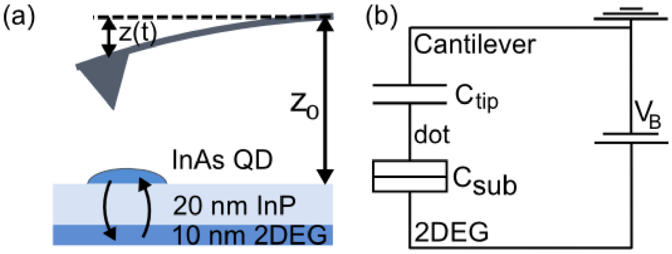

Figure 2.3: a) Schematic of the experimental setup showing the oscillating cantilever above a QD. b) Single-electron box circuit (adapted from[24])

where $\Gamma_+ \equiv \Gamma_{+,n-1}$ and $\Gamma_- \equiv \Gamma_{-,n}$ are the tunneling rates on and off the dot, respectively, and $\Gamma_\Sigma = \Gamma_+ + \Gamma_-$. Thus, we are left with a single ordinary differential equation (ODE) which relates the probability of occupation of the dot, p, with the energy-dependent tunneling rates. It is straightforward to solve this equation numerically for a given energy trajectory in time using one of the many families of ODE solvers such as the Runge-Kutta family of algorithms.

2.2 Force detection

2.2.1 Single-electron box

The nanosystem investigated in the present work involves the tip of an AFM sitting above a QD separated from an electrode by an opaque tunnel barrier (see Figure 2.3a). It turns out that this system is very well modelled by the single-electron box (SEB) shown in Figure 2.3b. A SEB is the simplest circuit in which the effects of single charge tunneling are important to consider[55]. In this circuit, the tip of the cantilever is grounded and acts as a movable gate electrode. It forms a classical capacitor with the dot and is described by a capacitance, C_{tip}. The dot is separated from a metallic electrode by an insulating barrier thus forming a tunnel junction characterized macroscopically by a capacitance, C_{sub}, and a tunnel resistance, R_T. The metallic electrode is connected to a voltage source with bias V_B. In the regime of Coulomb blockade, the charge on the dot, $q = q_{sub} - q_{tip}$, is fixed and the tunnel barrier can be treated as a capacitor. The circuit can then be analyzed using Kirchhoff's laws. The potential drop between the dot and the reservoir is:

$$\phi_{ext}(q) \equiv V_{sub} = \frac{q}{C_\Sigma} + \frac{C_{tip}}{C_\Sigma} V_B \tag{2.22}$$

where

$$C \equiv C_\Sigma = C_{tip} + C_{sub} \tag{2.23}$$

and α, the lever-arm parameter, is defined as:

$$\alpha = \frac{C_{tip}}{C_\Sigma}. \tag{2.24}$$

Note that α is an important experimental parameter since it determines the fraction of V_B that is applied to the dot.

The free electrostatic energy of the system as a function of N and the applied bias, V_B, is given by[79,84,87,32]:

$$F_{el}(N) = \frac{(Ne)^2}{2C_\Sigma} - Ne\frac{C_{tip}}{C_\Sigma}V_B - \frac{1}{2}V_B^2\frac{C_{tip}C_{sub}}{C_\Sigma} \tag{2.25}$$

where $C_\Sigma = C_{tip} + C_{sub}$.

2.2.2 Electrostatic force

One of the unconventional aspect of using AFM to detect single-electron transport lies in the fact that a force is measured instead of a current as is traditionally done in transport measurements or STM. The AFM tip is also used as a gate to control single-electron charging in the experiments. To obtain the force acting on the cantilever, F, all we need to do is to take the derivative of the free energy (Eq. 2.25) with respect to the tip-QD distance, z:

$$\begin{aligned} F &= = \frac{1}{2}\frac{C_{sub}^2}{C_\Sigma^2}\frac{\partial C_{tip}}{\partial z}\left(V_B - \frac{q}{C_{sub}}\right)^2 && (2.26) \\ &= \frac{1}{2}\frac{\partial C_{series}}{\partial z}\left(V_B - \frac{q}{C_{sub}}\right)^2 && (2.27) \end{aligned}$$

It is clear from this expression that single-electron charging of QDs is detectable through a shift of the contact potential difference (i.e. the voltage for which the force is minimal). This is the basis of Kelvin probe microscopy (KPFM) and single-electron charging was experimentally measured this way.

The approach favored in this thesis differs appreciably from KPFM since, instead of detecting static charges ($\Gamma = 0$), a resonant tunneling of electrons between a QD and the electrode is detected. Under perturbation, the dynamic response of the charge sitting on the nanostructure reveals information of its electronic structure as demonstrated experimentally in Chapter 5.

2.2.3 Electromechanical coupling

Let's now turn attention to the description of the dynamics of the cantilever capacitively coupled to the QD. Although the theoretical problem of nanoelectromechanical systems can be formidable, it is much simpler in the context of our AFM experiments. Indeed, for small cantilever motion compared to the tip-dot distance, C_{tip} varies linearly with z and the interaction Hamiltonian can be linearized with respect to z to obtain[†]

$$\mathcal{H}_{\text{int}} = -A\,\hat{N} \cdot \hat{z} \tag{2.28}$$

where $\hat{z}$ is the position of the oscillator and A is the coupling strength. The latter is given by:

$$A = \frac{\partial \alpha}{\partial z} = -2\frac{E_c}{e}V_B(1-\alpha)\frac{\partial C_{tip}}{\partial z}. \tag{2.29}$$

In the limit of weak coupling, back-action effects can be directly related to the quantum noise of the uncoupled QD[20,21]. The origin of back-action damping in such system can be understood in a semi-classical picture, which is adopted here for simplicity. Note that the results are exactly the same to what is found from a perturbative quantum-mechanical calculation performed to lowest non-vanishing order[21].

First, the cantilever can be modelled classically by a simple damped harmonic oscillator considering there are billions of harmonic oscillator quanta excited during experiments. Its motion follows the dynamic equation

$$m\frac{d^2 z(t)}{dt^2} + m\gamma\frac{dz(t)}{dt} + k(z(t) - z_0) = F_{\text{drive}}(t) + F(t) \tag{2.30}$$

where m is the mass, k the spring constant, γ the internal damping and z_0 the equilibrium position of the cantilever. During experiments, the cantilever oscillates on resonance $\omega/2\pi$ and at constant amplitude, a, through real-time control of $F_{\text{drive}}(t)$.

[†] The term coupling z to N^2 is neglected since it is of higher order in $\alpha \ll 1$.

The motion of the cantilever modulates the energy of the dot:

$$\Delta E(t) = \Delta E_{dc} + A\,a\cos(\omega t). \tag{2.31}$$

Because of the finite tunneling rate of electrons, the dynamic response of the number of electron on the dot, $p(t)$, will be slightly out-of-phase with respect to the motion of the cantilever. By disregarding momentarily the granularity of the electron, the number of electrons on the dot is treated as a continuous variable and the AFM responds as if it was driven by a force

$$F(t) = A\,p(t). \tag{2.32}$$

The in-phase component of the resulting back-action force changes the resonance frequency of the cantilever while the out-of-phase component changes its dissipation. Assuming the motion of the cantilever remains sinusoidal, the back-action force due to electron tunneling will result in frequency shift , $\Delta f = \Delta\omega/2\pi$, and dissipation, $\Delta\gamma$[51,49,36]:

$$\Delta\omega = -\frac{\omega_0}{ka}\frac{\omega_0}{2\pi}\int_0^{2\pi/\omega_0} dt\cos(\omega_0 t)\,F(t) \tag{2.33}$$

$$\Delta\gamma = \frac{2\omega_0}{ka}\;\frac{\omega_0}{2\pi}\int_0^{2\pi/\omega_0} dt\sin(\omega_0 t)\,F(t) \tag{2.34}$$

The only quantum mechanical feature that enters this simple semi-classical picture is the tunneling rate of electrons through the simplified master equation 2.20 which determines $p(t)$, hence $F(t)$. Note that this result is also mathematically identical to a mean-field approximation describing the problem of strong coupling[13].

2.3 Numerical solution

I present an efficient approach to evaluate Eqs. 2.33-2.34 for any given functional form of tunneling rates and energy modulation. This is particularly useful to fit experimental data. Let's consider the case of a sinusoidal modulation of ΔE with fundamental frequency $\omega/2\pi$:

$$\Delta E(t) = \Delta E_{dc} + \Delta E_{\omega} \cos(\omega t)\,. \tag{2.35}$$

The time evolution of the tunneling rates also becomes periodic and can be expressed in Fourier series as:

$$\Gamma_{\pm}(t) = \sum_{n=-\infty}^{\infty} \Gamma_{\pm,n\omega}\, \mathrm{e}^{in\omega t} \tag{2.36}$$

where $\Gamma_{\pm,n\omega}$ are complex Fourier series coefficient. Using the simplified master equation 2.20, we can relate the Fourier components of the probability of occupation of the dot, $p_{n\omega}$, to those of the tunneling rates by a matrix multiplication

$$\boldsymbol{A}\,\boldsymbol{p_{n\omega}} = \boldsymbol{\Gamma_{+,n\omega}} \tag{2.37}$$

where $\boldsymbol{p_{n\omega}}$ and $\boldsymbol{\Gamma_{+,n\omega}}$ are column vectors of Fourier coefficients and $\boldsymbol{A}$ is a matrix with elements:

$$A_{n,k} = \Gamma_{\Sigma,(n-k)\omega} + in\omega\delta_{n,k}. \tag{2.38}$$

The frequency shift and dissipation are then obtained using Eqs.2.33-2.34 in which the integrals can be expressed in terms of the real and imaginary parts of the Fourier coefficient p_{ω}:

$$\Delta\omega = -\frac{\omega_0 A}{ka} \mathrm{Re}\, p_{\omega} \tag{2.39}$$

$$\Delta\gamma = \frac{2\omega_0 A}{ka}\mathrm{Im}\, p_\omega. \tag{2.40}$$

Note that $p_{n\omega} = p_{-n\omega}*$ since $p(t)$ is real-valued.

2.3.1 Linear response

For small energy modulation ΔE_ω, the problem is simplified because only a few Fourier components are non-zero. For example, if the tunneling rates vary linearly with ΔE, only three Fourier coefficients are non-zero:

$$\Gamma_\pm(t) = \overbrace{\Gamma_\pm(\Delta E_{dc})}^{\Gamma_{\pm,0}} + \overbrace{\Gamma'_\pm(E_{dc})\,\Delta E_\omega}^{\Gamma_{\pm,\omega}+\Gamma_{\pm,\omega}*}\cos(\omega t) \tag{2.41}$$

where $'$ denotes derivative with respect to energy. The system of linear equations 2.37 becomes:

$$\underset{\boldsymbol{A}}{\begin{pmatrix} \Gamma_{\Sigma,0} - i\omega & \Gamma_{\Sigma,\omega} & 0 \\ \Gamma_{\Sigma,\omega} & \Gamma_{\Sigma,0} & \Gamma_{\Sigma,\omega} \\ 0 & \Gamma_{\Sigma,\omega} & \Gamma_{\Sigma,0} + i\omega \end{pmatrix}} \underset{\boldsymbol{p_{n\omega}}}{\begin{pmatrix} p_{-\omega} \\ p_0 \\ p_\omega \end{pmatrix}} = \underset{\boldsymbol{\Gamma_{+,n\omega}}}{\begin{pmatrix} \Gamma_{+,-\omega} \\ \Gamma_{+,0} \\ \Gamma_{+,\omega} \end{pmatrix}} \tag{2.42}$$

where we used the fact that $\Gamma_{\pm,n\omega} = \Gamma_{\pm,-n\omega}$. From the second linear equation, we find that

$$p_0 \approx \frac{\Gamma_{+,0}}{\Gamma_{\Sigma,0}} \tag{2.43}$$

which can be used to solve the third equation yielding

$$p_\omega = \frac{\Gamma_{+,\omega}\,\Gamma_{\Sigma,0} - \Gamma_{+,0}\Gamma_{\Sigma,\omega}}{\Gamma_{\Sigma,0}(\Gamma_{\Sigma,0} + i\omega)}\,. \tag{2.44}$$

This last result is important because it directly relates the response of p to a periodic excitation in terms of the tunneling rates and their first derivatives. The frequency shift and dissipation are then:

$$\Delta\omega = -\frac{\omega_0 A}{ka}\frac{(\Gamma_{+,\omega}\,\Gamma_{\Sigma,0} - \Gamma_{+,0}\Gamma_{\Sigma,\omega})}{(\Gamma_{\Sigma,0}^2 + \omega^2)} \tag{2.45}$$

and

$$\Delta\gamma = \frac{2\omega_0 A}{ka}\frac{\omega}{\Gamma_{\Sigma,0}}\frac{(\Gamma_{+,\omega}\,\Gamma_{\Sigma,0} - \Gamma_{+,0}\Gamma_{\Sigma,\omega})}{(\Gamma_{\Sigma,0}^2 + \omega^2)}. \tag{2.46}$$

Finally, a key result in this linear regime is that the ratio of the frequency shift and dissipation (Eqs. 2.45 and 2.46) is directly related to the total tunneling:

$$\Gamma_\Sigma = 2\omega_0\frac{\Delta\omega}{\Delta\gamma}. \tag{2.47}$$

In Chapter 5, I take advantage of the equations given above to perform energy level spectroscopy. Note that equations 5.4-5.5 are strictly equivalent to Eqs. 2.45-2.46 since

$$\Gamma_{\pm,\omega} = \frac{1}{2}Aa\Gamma'_{\pm}. \tag{2.48}$$

2.3.2 Strong coupling

If the tunneling rates do not vary linearly with the motion of the cantilever, more Fourier components must be taken into account to properly describe the time evolution of the tunneling rates. This is the case, for example, when the energy modulation ΔE_ω is larger than the thermal energy. This can efficiently be taken into account numerically.

First, the Fourier components $\boldsymbol{\Gamma}_{\pm,\boldsymbol{n\omega}}$ are computed using a fast Fourier transform, an extremely fast operation on modern computers. Second, the matrix $\boldsymbol{A}$ defined by Eq. 2.38 is loaded in memory[‡]. Finally, the Fourier components $\boldsymbol{p}_{\boldsymbol{n\omega}}$ are obtained

---

[‡] This operation can be cached in advance to speed up the execution time.

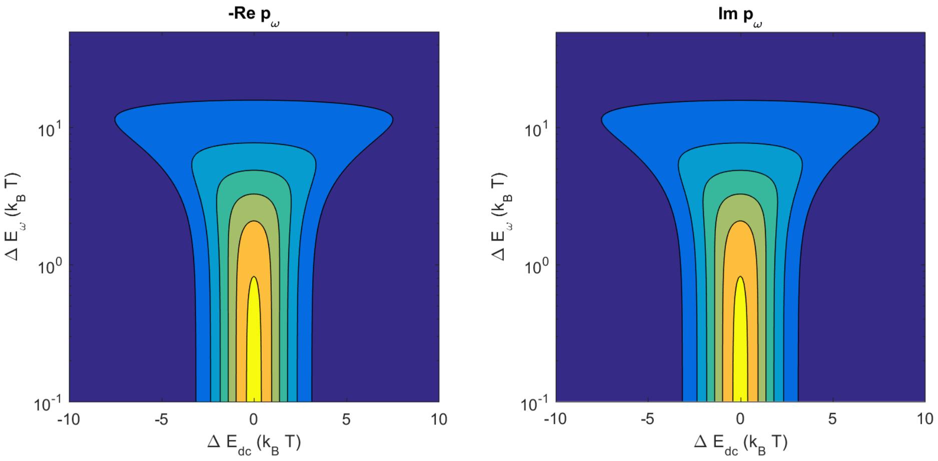

Figure 2.4: Real and imaginary parts of p_ω as a function of ΔE_{dc} and ΔE_ω considering tunneling into a single-non degenerate level. 256 Fourier coefficients were taken into account for the calculation of each point. Each grid is made up of 200 by 200 points.

by performing a matrix inversion of Eq. 2.37. By using an optimized library such as LAPACK[4] or specialized hardware, this operation can be performed quickly.

In Figure 2.4, the real and imaginary part of p_ω are plotted as a function of ΔE_{dc} and ΔE_ω considering tunneling in and out of a single-non degenerate level in the dot. In this case, the tunneling rates on and off the dot are respectively $\Gamma_+(\Delta E) = f(\Delta E)$ and $\Gamma_-(\Delta E) = (1 - f(\Delta E))$ where $f(\Delta E)$ is the Fermi function. By taking into account 2^8 Fourier coefficients, a 200 by 200 grid of points is computed using Matlab in less than a minute using a single-core Intel Core i5 processor. The results are in complete agreement with a full Monte Carlo simulation (see Ref. 13 for details).

In summary, the proposed numerical algorithm computes the response of AFM for any given functional form of tunneling rates whether they vary linearly or not with the motion of the cantilever. The trade off between speed and accuracy can be conveniently controlled by a single parameter which is the number of Fourier coefficients to take into account.

3

Instrumentation

Scanning probe microscopy (SPM) is a branch of microscopy that was founded in 1981 with the invention of the scanning tunneling microscope (STM) by Gerd Binnig and Heinrich Rohrer[14]. In SPM, images are produced by scanning a sharp probe above a surface and regulating its distance using a feedback loop. In the case of STM, the probe and the sample are conductive and tunneling current is measured. Because the tunneling rate falls off exponentially with distance, slight variations in the tip-sample gap result in a large change in current which is used to perform sensitive feedback control using a piezoelectric scanner. By shaping the electrode as a tip, the current practically flows only from the front atoms of the tip thus providing lateral resolution of atomic dimension. In concert, these two properties allowed STM to produce topographic images with atomic resolution, an unprecedented feat[14]. The success of STM was highlighted in 1986 when its inventors were awarded the Nobel Prize in physics.

In 1986, Binnig, Quate, and Gerber combined the principles of STM with a stylus profilometer to create the atomic force microscope[15]. While STM can only be used to image conductive samples, AFM measures forces, which are ubiquitous, and can spatially map properties of a surface regardless of its conductivity. It has become a standard laboratory tool because of its commercial availability and ease of use. It is widely used to image not only inorganic materials but also biological samples such as individual proteins and DNA. It has even been demonstrated that AFM can be utilized to do atomic manipulation and even sense chemical bonds between atoms[43].

In this chapter, I overview the challenges and opportunities offered by low temperature AFM and detail some aspects of the McGill home-built low-temperature atomic force microscope (LT-AFM). I present the main modes of operation of AFM and discuss how to accurately measure dissipative forces, a subject not well-covered in the numerous reviews on AFM[36,37,67].

3.1 The Low-temperature AFM

The ability to operate AFM at low temperature has several benefits such as signal-to-noise ratio improvements, better instrument stability, reduced thermal drift, as well as providing access to low temperature physical phenomena. This last point is especially important since, as discussed in section 2.1, single-electron charging effects disappear at elevated temperature.

The McGill LT-AFM was built to operate at 4.2 K[75]. The original design and construction is described in the PhD thesis of Mark Roseman[76]. It was further improved by Romain Stomp[85] and Lynda Cockins[24]. The schematic of the current design of the

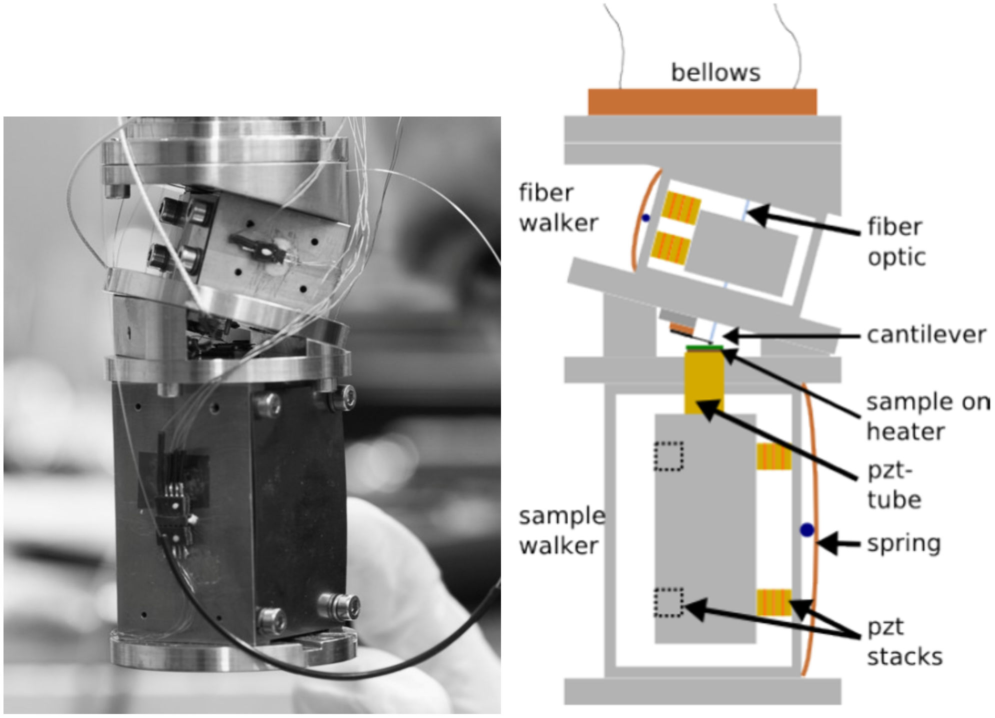

Figure 3.1: Photo of the LT-AFM head is shown beside a schematic showing the components of the microscope. The bottom plate in the schematic is 5 x 52 mm.

instrument is provided in Figure 3.1.

3.1.1 Force probe

The force detection system is the central part of any AFM. In our LT-AFM, microfabricated silicon cantilevers are used as a mechanical transducer to convert force into displacement. For small displacements, the relation between force and displacement is well modeled by a simple damped harmonic oscillator.

The cantilevers are bought from Nanosensors (model PPP-NCLR) and they typically have a force constant, k_0, of about 40 N/m, a resonance frequency, $\omega/2\pi$, varying between 146 and 236 kHz, and a quality factor, Q, varying between 500 and 100,000

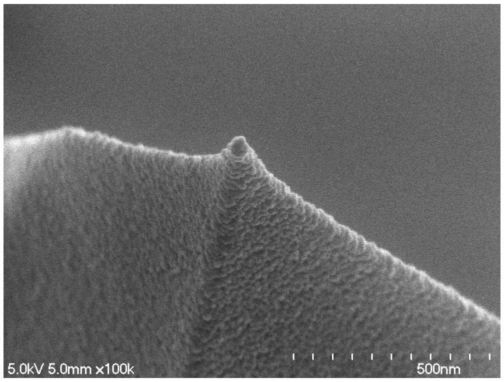

Figure 3.2: SEM image of the tip of a PPP-NCLR cantilever from Nanosensor coated with a 5 nm Ti layer and a 10 nm Pt layer.

depending on pressure and temperature. For charging experiments, the tip is coated with a 10 nm layer of platinum to make them conductive. A 5 nm titanium layer is first deposited to ensure good adhesion of the platinum. Deposition of both layers is done with an electron beam evaporator. The tip is subsequently imaged using scanning electron microscopy to make sure they are not damaged and therefore adequate for experiments. The tip radius is usually around 25 nm as shown in the scanning electron microscope (SEM) image in Figure 3.2.

3.1.2 Fiber optic interferometer

The displacement of the cantilever is measured via a fiber optic interferometer[78]. We use a single-fiber design in which an optical cavity is formed with the cantilever, the latter acting as a mirror because of its reflective coating. In this setup (Figure 3.3), the fraction of the light reflected at the end of the fiber interferes with the light coming from the cantilever and is detected by a photodiode outside the microscope. The interference pattern then allows precise measurements of changes in fiber-cantilever distance.

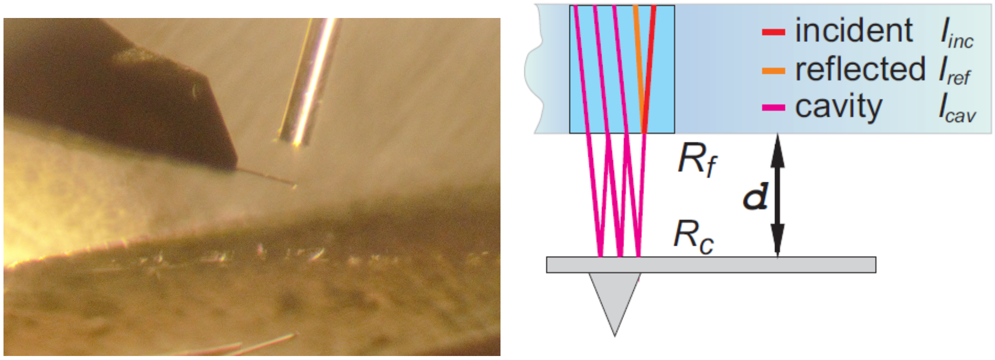

Figure 3.3: Left) Photo of fiber hovering the micro-fabricated silicon cantilever. A reflection of the cantilever can be seen on the gold surface at the very bottom of the picture. Right) Schematic of the optical cavity. The end of the fiber and the cantilever are both acting as mirrors (adapted from Ref.[96])

Overview

In order to optimize the sensitivity of the interferometer, the optical fiber is glued to a walker that moves along piezo-electric stacks using stick-slip motion. As it moves closer to the cantilever, the signal measured at the photodiode shows peaks with a periodicity of $\lambda_{\text{laser}}/2$, where λ_{laser} is the wavelength of the laser. For large fiber-cantilever distances, the interference pattern is simply sinusoidal as in a Michelson interferometer[78]. However, at smaller distances, multiple reflections between the cantilever and the fiber occur and the cavity behaves like a Fabry-Pérot interferometer[47]. The exact shape of the interference pattern depends on various parameters such as the coupling loss[*], the absorption of light by the mirrors and the angular misalignment between the cantilever and the fiber. Since a slight change in the geometry of the system can have a huge effect on the interference pattern[103], the sensitivity of the system can change dramatically after thermal cycling. Figure 3.4 shows the complex features of a cavity misaligned due

---

[*] The coupling loss is the amount of reflected light from the cantilever that doesn't couple back into the fiber.

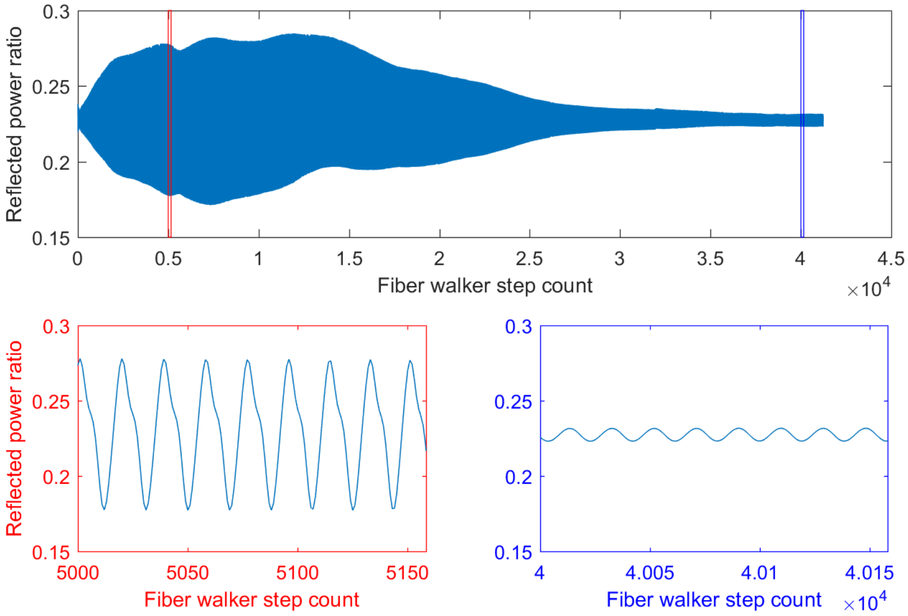

Figure 3.4: Power of the reflected light as a function of the number of fiber walker steps away from the cantilever. The signal is normalized with respect to the power of the incoming light. The measurement was performed at 77 K in a vacuum of 10^{-5} mbar. Top) The peak to peak value of the the interference fringes varies in a complex way with respect to the fiber-cantilever distance. Bottom left) Zoomed signal in the region delimited by the red rectangle in the top panel. Close to the cantilever, the peak shape of the interference fringes is clearly asymmetric. Bottom right) Zoomed signal delimited by the blue box in the top panel. Far away from the cantilever, the peak shape is symmetric much like in a Michelson interferometer.

to strain and stress associated with cooling to 77 K. At room temperature, this cavity had much simpler response to change of the cavity length. Most notably, the peak to peak value of the fringes monotonically increased when approaching the fiber. Because the peak shape of the interference fringes are practically unpredictable in our instrument, it is necessary to characterize the cavity whenever the cantilever is replaced or the system's temperature modified.

CALIBRATION

The sensitivity of the interferometer, S, is simply given by the slope of the measured voltage V_{PD} with respect to the fiber-cantilever distance z:

$$S = \frac{dV_{\mathrm{PD}}(z)}{dz}. \tag{3.1}$$

It can be obtained by converting the number of fiber walker steps (see Figure 3.5) into distance. Since the distance between successive peaks is known, the stepping size of the walker, Δz, can be approximated by counting the number of steps between successive peaks. It turns out to be surprisingly constant over a few fringes. In Figure 3.5 (top panel), the number of steps between fringes is 24.8 ± 0.7 which yields a step size $\Delta z \approx 31.3$ nm. By taking the derivative of the photodiode signal versus fiber-cantilever distance, which is plotted in Figure 3.5 (bottom panel), we obtain S in units of nm with precision better than a few percent by dividing it by Δz.

IMPROVING BACK-REFLECTIVITY

The sensitivity of the system is greatly limited by the weak back-reflection of bare cleaved fibers which reflect only 3-4 % of the incident light power. However, by coating the fiber's end, its back-reflection can be greatly increased. Following the procedure suggested by Subba-Rao et al.[88], multiple optic fibers were coated with a TiO_2 reflective layer. The deposition of the film is performed by dipping the fiber end in a solution of titanium-(IV)-2-ethylhexoxide diluted five times in xylene and by firing it to high temperature using a propane torch light. The optimal time of annealing is less than a second. The fiber is in only introduced to the outer part of the flame to prevent it from burning or curling up. The back-reflection can be monitored in real-time during the

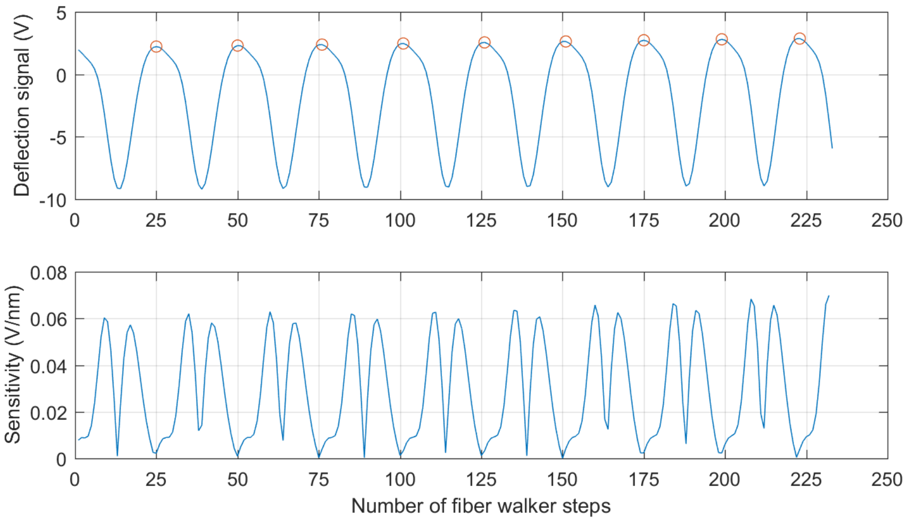

Figure 3.5: Top panel) Photodiode signal as a function of the number of fiber walker steps towards the cantilever. The summit of the peaks are indicated by red circles whose position are used to compute the number of steps between each fringes. The step size is constant to better than ± 3 %. Bottom panel) The sensitivity S is obtained by taking the derivative of the photodiode signal and dividing it by the average step size of 31.3 nm.

annealing to assess the quality of the film. Back-reflection up to 30-40 % were obtained. Tens of fiber were produced using this method early in my PhD work and were later spliced onto the LT-AFM.

Displacement noise

The displacement noise obtained with TiO2-coated fibers is almost one order of magnitude better than that previously reported (60 fm/Hz$^{1/2}$) by Cockins[24] with bare fibers limited by shot noise. As shown in Figure 3.6, the noise floor around the thermal peak of the cantilever is roughly 7 fm/Hz$^{1/2}$. The sensitivity used for calibrating the noise spectrum corresponds to the last measured value in Figure 3.5 (bottom panel; S=0.069 V/nm).

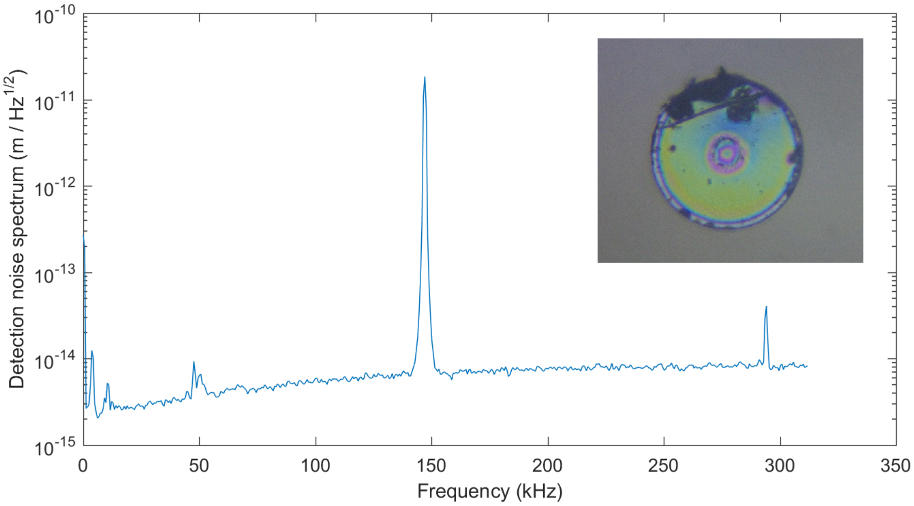

Figure 3.6: Displacement noise of the interferometer. The thermal motion of the cantilever is clearly observed at around 150 kHz. The low detection noise is achieved due to the use of a TiO_2 reflective coating at the end of the optic fiber which improves its back-reflectivity from 3 % to 30 %. The inset shows a picture of the fiber end.

3.1.3 EXCITATION SYSTEM

The other essential part of any AFM is its excitation system. This is because dynamic mode AFM, which relies on an excitation system to keep the cantilever oscillating, has tremendous advantages over static AFM. The most popular method to excite the cantilever is by mounting it onto a piezoelectric stack. By applying a voltage to the stack, the non-inertial frame of reference of the cantilever is moved up and down which is equivalent to applying a force on the the cantilever. This can be used to efficiently excite the motion of the cantilever and this capability is implemented in our LT-AFM. The cantilevers are glued with silver paint to a cantilever holder epoxy-bonded to a piezo stack.

As I will explain in details in the next section, the interpretation of frequency-modulation AFM (FM-AFM) data is greatly simplified if the transfer function of the excitation system is constant. Although it is assumed to be the case in the seminal theory of frequency-modulation AFM of Hölscher et al.[49], this is hardly the case experimentally. This shortcoming of the theory is well recognized in the context of operation of AFM in liquid environments[56]. but its importance in vacuum was only fully appreciated recently by my colleagues Labuda et al.[58].

Photothermal excitation[72] is an alternative to piezoacoustic excitation which is known to have a flatter transfer function in liquid environments[56]. The principle of operation is to modulate the power of an incident light to photo-induce a force to drive the cantilever. We integrated this capability into the LT-AFM in a non-invasive way by sending the excitation laser light into the optic fiber already used for detection. This is achieved by using the optical circuit illustrated in Figure 3.7. The detection laser, shown in blue (λ=1550 nm), and the excitation laser, shown in red (λ=1310 nm), are combined into the common port but filtered on their way back by a specialized wavelength-division multiplexer. Finally, an optical circulator sends the detection laser light to the photodiode. This is to our knowledge, the first implementation of a low-temperature AFM using a single-fiber design to perform both detection and excitation. We hope that the simple design will renew interest for interferometer-based low-temperature AFM.

An easy way to assess the transfer function of the excitation system is to perform constant excitation of the cantilever and measure the response using lock-in measurement. By sweeping the frequency, the transfer function of the cantilever, which is Lorentzian, is expected to be observed. Deviations from this lineshape are indicative of a non-flat excitation transfer function. The data plotted in Figure 3.8 compares the response of a cantilever driven by photothermal and piezoacoustic systems in high vacuum at 4 K. In this particular instance, it is clear that the photothermal excitation scheme is much cleaner that the piezoacoustic system.

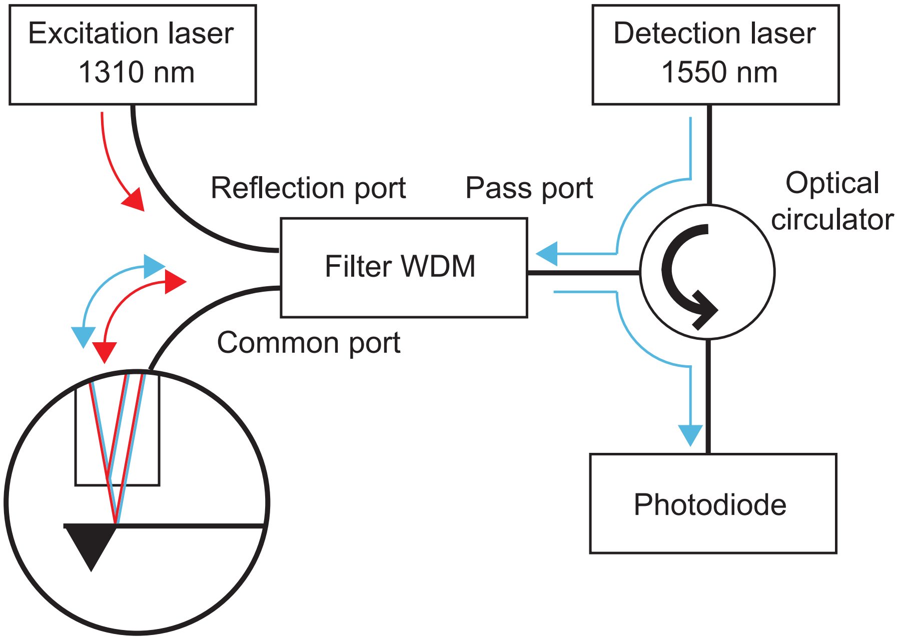

Figure 3.7: Diagram of the optical circuit used to perform detection and excitation in a single-fiber design. Detection is perform by interferometry using the light shown in blue (λ=1550 nm) whereas excitation is performed by modulating the power of the light shown in red (λ=1310 nm). Both lasers are combined into the common port but are filtered on their way back by a specialized wavelength-division multiplexer. Finally, an optical circulator, in which light entering any port exits from the next, sends the detection laser light to the photodiode.

Realizing a clean excitation system is of key importance to establish a reference against which other excitation schemes can be calibrated for accuracy. In the event that photothermal excitation is not available, one can use electrostatic excitation through capacitive coupling between the tip and a conductive sample to cleanly excite the cantilever. I have implemented a calibration technique based on this approach for the commercial SPM controller developed by Nanonis. Further details can be found in our patent[57].

3.2 Theory of AFM

In this section, I present different force measurement methods used in atomic force microscopy. Since this thesis is mostly concerned with frequency-modulation AFM (FM-AFM), more emphasis will be put on this particular operation mode. However, I present precursory methods as they are conceptually simpler and naturally brings the idea of FM-AFM.

3.2.1 Cantilever dynamics

Atomic force microscopy is conceptually simple: it relies on the idea that the displacement of a spring can be converted into a force. Assuming damping is velocity-dependent, its position $z(t)$ is related to force $F(t)$ according to Newton's second law:

$$m\frac{d^2z(t)}{dt^2} = -kz(t) - m\gamma\frac{dz(t)}{dt} + F(t) \tag{3.2}$$

where m is its mass, k its spring constant and γ is its internal damping. In the following, I often refer to the quality factor which is defined $Q \equiv \omega_0/\gamma$.

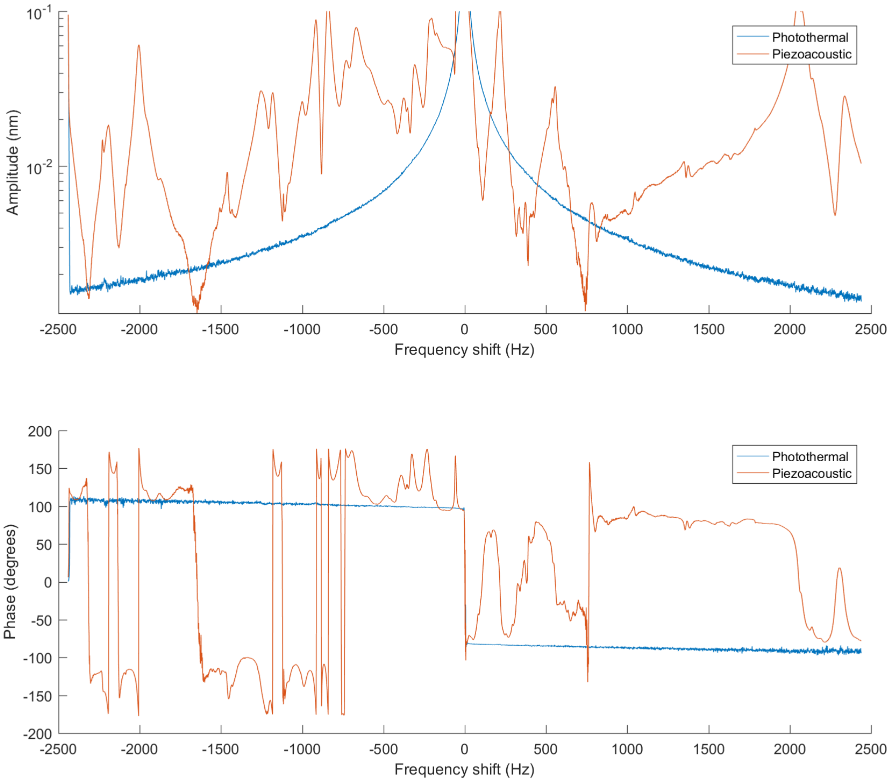

Figure 3.8: Constant excitation frequency sweep with photothermal and piezoacoustic excitation. Drive amplitude is tuned to obtain 10 nm oscillation on resonance $\omega/2\pi$ =144.617 kHz (i.e. zero frequency shift) and kept constant throughout. Top panel is the amplitude response and bottom panel is the phase response.

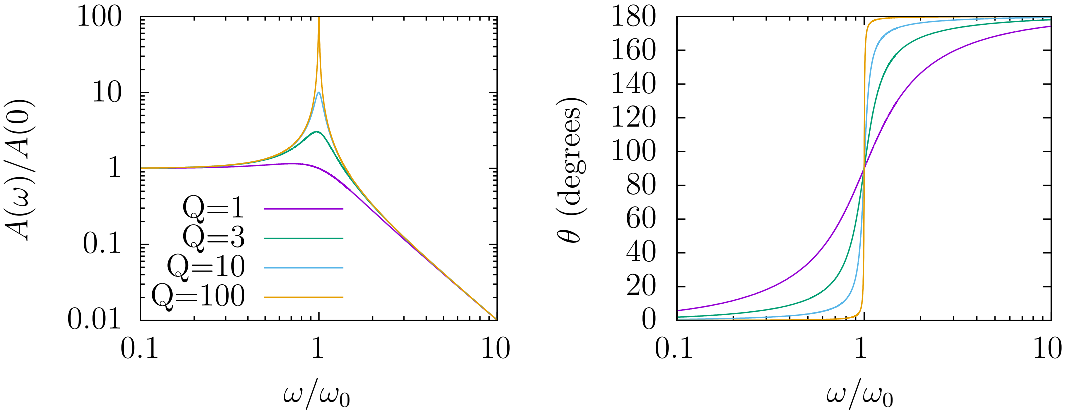

Figure 3.9: Transfer function of a damped simple harmonic oscillator. (Left) Amplitude transfer function for Q=1,3,10 and 100. Right) Phase transfer function for same set of quality factor.

Static AFM In the static mode of operation, the force is given by $F = -k(z - z_0)$, where z_0 is the spring's equilibrium position. The physical interpretation of static AFM images is therefore extremely simple. However, because static AFM consists in doing a DC measurement of the position, it is particularly affected by $1/f$ noise existing in any electronic system. Realizing a low-noise implementation of static AFM is therefore experimentally challenging.

Dynamic AFM In dynamic AFM, the cantilever is driven at a controlled frequency and forces are measured through their effects on the dynamics of the cantilever. Through phase sensitive measurements, forces can be detected with much higher signal to noise ratio than in static AFM. The downside is that it implies an understanding of the dynamic of the system in order to relate the motion of the cantilever in time to forces.

Steady-state solution Let's first look at the the steady-state solution (when $t \to \infty$) of Eq. 3.2 for periodic forcing $F(t) = F_0 \cos(\omega t)$ given by[34]:

$$z(t) = A(\omega)\cos(\omega t - \theta) \tag{3.3}$$

where

$$A(\omega) = \frac{F_0/m}{[(\omega_0^2 - \omega^2)^2 + (\gamma\omega)^2]^{1/2}} and \tag{3.4}$$

$$\tan\theta = \frac{\gamma\omega}{\omega_0^2 - \omega^2} \tag{3.5}$$

are the amplitude and the phase lag respectively. For convenience, $A(\omega)$ and $\tan\theta$ are plotted for various Q factors in Figure 3.9. This result provides a simple way of measuring forces through changes in amplitude, a method called amplitude modulation AFM (AM-AFM). In AM-AFM, the cantilever is driven at a fixed frequency near resonance and upon a tip-sample interaction force $F(z(t)) = k_{ts}z(t)$, the resonance frequency of the cantilever shifts changing its oscillation amplitude. It follows that a cantilever with a high Q factor is more sensitive due its very narrow resonance.

Transient response The full solution to Eq. 3.2 under forced oscillation also contains a transient response which sets a limit on the measurement bandwidth of AM-AFM:

$$z(t) = \mathrm{e}^{-\gamma t}\cos(\omega_1 t + \beta) + A\cos(\omega t - \delta). \tag{3.6}$$

After a change in interaction force and of resonance frequency, it will take finite time for the oscillator to reach its new steady-state. The amplitude response time of the oscillator is inversely proportional to its Q factor[2]. This is illustrated in Fig.3.10 where the oscillator slowly reaches its steady state amplitude before slowly decaying after the

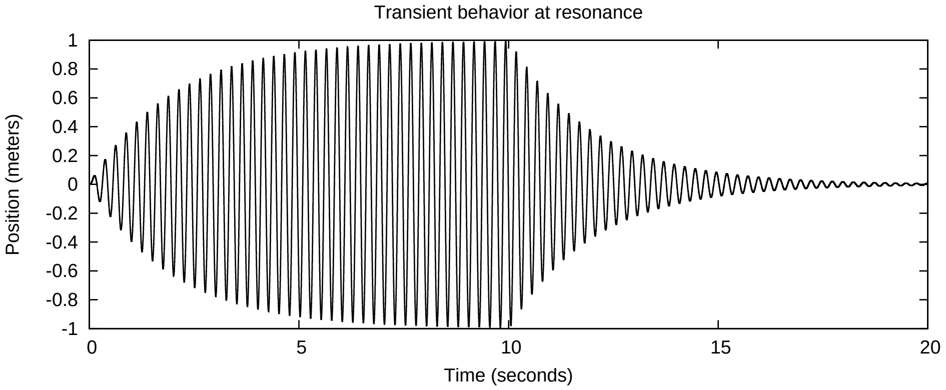

Figure 3.10: Transient behavior of a damped harmonic oscillator ($\omega = 1$, $Q = 25$) initially at rest. When driven exactly on resonance, its oscillation amplitude slowly grow towards its steady-state value. When the driving force is turned off after 10 seconds, its amplitude slowly decay. The amplitude response time of the oscillator is inversely proportional to its Q factor.

driving force F_0 is set to zero.

3.2.2 FM-AFM

As seen above, increasing the Q factor in AM-AFM reduces noise at the expense of bandwidth. To get around this undesirable compromise Albrecht et al.[2] proposed a new measurement mode called frequency-modulation AFM (FM-AFM) which benefits from the increase sensitivity of high Q factor cantilever without sacrificing measurement bandwidth.

The signal processing involved in FM-AFM is presented in the following paragraphs. It is of key importance to understand which assumptions are necessary to make in order to decouple conservative and dissipative force measurement in FM-AFM measurements. This allows to understand the origin of systematic error in experimental data and how to apply calibration to accurately measure forces.

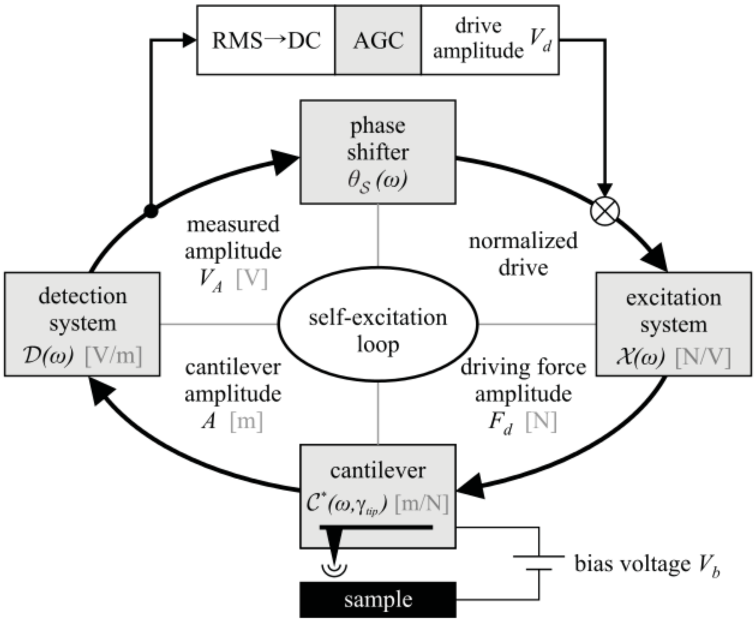

Figure 3.11: Schematic of self-oscillation system in FM-AFM as reported in[58].

PRINCIPLE

In order to get around the slow amplitude response of the cantilever, the oscillation amplitude is kept constant throughout the experiment in FM-AFM. Furthermore, the cantilever is always driven on resonance, contrarily to AM-AFM. Several different electronic systems, both analog and digital, can be used to perform this task. However, because of its simplicity and historical importance, I only overview below a self-oscillation scheme that uses the cantilever as the frequency determining element of the circuit.

SELF-OSCILLATION

The first FM-AFM experiments performed relied on self-oscillation to drive the cantilever[2]. In this scheme, the output of the oscillator was used as a feedback signal to drive the excitation system. By appropriate phase shifting and amplification of the detector output, steady amplitude can be achieved provided that the frequency selectivity of the oscillator is high enough (high Q factor)[31]. The transfer function of the closed-loop system (see Figure 3.11) is given by:

$$H(\omega) = \frac{X(\omega)C(\omega)}{1 - GX(\omega)C(\omega)} \tag{3.7}$$

where $C(\omega)$, $X(\omega)$ and G are complex gains representing the transfer function of the cantilever, the excitation system and the feedback amplifier respectively. Their phase are respectively denoted $\theta_C(\omega)$, $\theta_X(\omega)$ and θ_G. In order to sustain stable oscillations at frequency $\omega/2\pi$, the following conditions, known as Barkhausen criteria, have to be met:

$$|G||X(\omega)||C(\omega)| = 1 \tag{3.8}$$

$$\theta_G + \theta_X(\omega) + \theta_C(\omega) = 2n\pi. \tag{3.9}$$

where θ is the phase of a transfer function. Let's consider those conditions in the context of a cantilever described by Equation 3.2. Its transfer function $C(\omega, \omega_0, \gamma)$ is defined by its amplitude and phase[58]:

$$|C(\omega, \omega_0, \gamma)| = -\frac{\sin(\theta_C(\omega, \omega_0, \gamma))}{\omega \times \gamma} \tag{3.10}$$

$$\theta_C(\omega, \omega_0, \gamma) = \arctan \frac{\gamma\omega}{\omega_0^2 - \omega^2} \tag{3.11}$$

where ω_0 is the natural frequency of the cantilever and γ is its intrinsic velocity dependent damping. Note that those expressions are exactly equivalent to Equations 3.4 and

3.5.

The phase condition defined by Eq. 3.9 determines the frequency of oscillation. By assuming that the self-excitation system responds instantly, the cantilever phase is always defined by $\theta_C = -\theta_G - \theta_X$. This determines the oscillation frequency through Eq. 3.11:

$$\frac{\Delta\omega}{\omega} \simeq -\frac{1}{2Q\,\tan\theta_C}. \tag{3.12}$$

where $\Delta\omega \equiv \omega - \omega_0$. Note that if the Q factor changes because of dissipative interactions, the oscillation frequency also shifts mimicking the presence of a tip-sample force gradient. This undesirable effect can be eliminated by operating the instrument exactly at the resonance of the sensor by setting $\theta_C = \pi/2$ through θ_G adjustment at the beginning of the experiment. However, any additional phase shift coming from the system transfer function, $\Delta\theta_X(\omega) = \theta_X(\omega) - \theta_X(\omega_0)$, will couple dissipation to frequency shift. Note that high-Q oscillators are more tolerant in this respect but an additional phase shift of $\Delta\theta_X = \pm\pi/2$ can kill the oscillation regardless of the Q factor. Therefore, filters should be designed to avoid phase variations within the frequency range of operation of the oscillator. Physically realizing such a system can be extremely difficult due to the non-ideal behavior of the mechanical system (see bottom panel of Figure 3.8).

In order to fulfill the amplitude condition defined by Eq. 3.8, the gain factor $|G|$ is adjusted during experiments to ensure the amplitude is kept constant:

$$\overbrace{|G_0||X(\omega_0)|\frac{\sin(\theta_C(\omega_0))}{\omega_0\,\gamma}}^{\text{start of experiment}} = \overbrace{|G||X(\omega)|\frac{\sin(\theta_C(\omega_0) - \Delta\theta_X(\omega))}{\omega(\gamma + \gamma_{\text{tip}})}}^{\text{during the experiment}} \tag{3.13}$$

where G_0 is the gain at the start of the experiment. By rearranging Eq. 3.13, the tip-sample damping, γ_{tip}, becomes:

$$\gamma_{\text{tip}} = \gamma\left(\frac{\Lambda}{S(\omega)} - 1\right) \tag{3.14}$$

where $\Lambda \equiv |G|/|G_0|$ is a normalized excitation gain and S is defined as

$$S(\omega) = \left|\frac{X(\omega)}{X(\omega_0)}\right|^{-1} \left|\frac{\sin(\theta_C(\omega_0) - \Delta\theta_X(\omega))}{\sin(\theta_C(\omega_0))}\right|^{-1} \left(\frac{\omega}{\omega_0}\right)^{-1}. \tag{3.15}$$

As can be seen from Eq. 3.14, S is a dimensionless calibration factor that corrects for the frequency dependence of Λ due to the non-flat transfer function of the excitation system and allows recovery of true tip-sample dissipation[58].

3.2.3 Transfer function correction

To close this chapter, I now propose an elegant approach to recover the tip-sample dissipation, γ_{tip}, without knowing the transfer function of the excitation system $X(\omega)$. The idea is to measure a bias spectrum spanning both positive and negatives values of voltage to self-consistently calibrate spectra. Due to electrostatic interaction with the sample surface, the cantilever's resonance shifts proportionally to the square of the bias voltage, i.e. $\Delta\omega/2\pi \propto \Delta V^2$. This ensures that a given frequency shift is observed twice in a spectrum. By then plotting Λ versus the simultaneously acquired frequency shift, the features that are due to the non-flat transfer function of the excitation system will overlap allowing their easy identification. This calibration procedure is shown in Figure 3.12 on a bias spectrum acquired with a piezoacoustic system on a 5 nm gold nanoparticle on hexadecanedithiols at 4 K (see chapter 4 for details of the sample preparation). The spectrum exhibits clear single-electron charging peaks in Λ (top left panel) but they are overlaid on top of a large background which needs to be accounted for

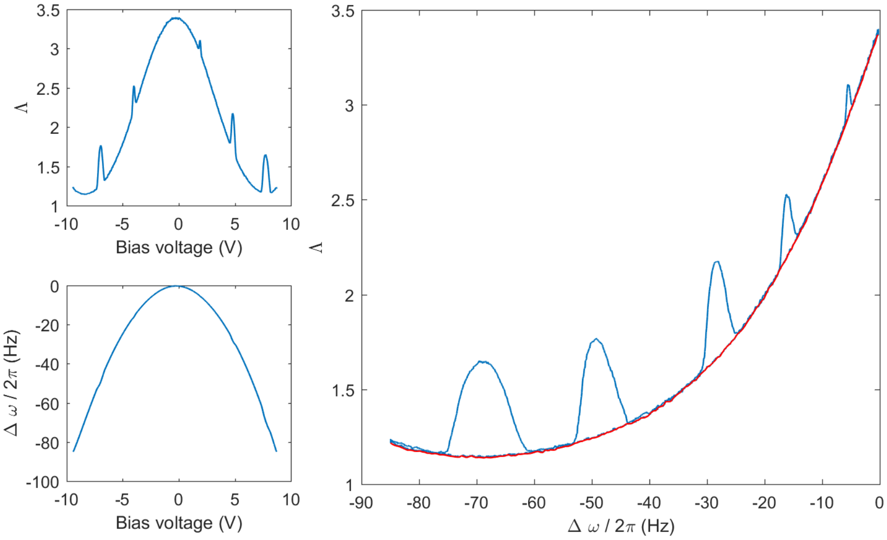

Figure 3.12: Bias spectrum acquired with a piezoacoustic system on 5 nm gold nanoparticles on hexadecanethiols at 4 K. Top left) Normalized excitation gain Λ versus bias voltage. Note that single-electron charging peaks are overlaid to a large background. Bottom left) Simultaneously acquired frequency shift versus bias voltage. Right) Normalized excitation gain versus frequency shift. A sliding window minimum algorithm is used to plot in red the minimum Λ versus frequency which corresponds to $S(\omega)$). Single-electron charging peaks can be accurately disentangled from the frequency-dependent background by using Eq. 3.14

to recover the accurate peak shape. By plotting Λ versus frequency shift (right panel), the background can easily be identified. A sliding window minimum algorithm can find the minimum value of Λ versus the frequency shift which essentially corresponds to $S(\omega)$. To improve the quality of the calibration, multiple spectra acquired at different position on the sample can be overlaid to progressively improve the measurement of $S(\omega)$. Finally, γ_{tip} can be computed with Eq. 3.14.

4

Preparation of self-assembled tunnel junctions

The measurement of single-electron charging of a QD with an AFM requires samples where QDs are sitting on a thin insulator above a back-electrode. Moreover, in order to obtain sufficient signal to noise ratio for adequate measurements, it is necessary that the tunneling rate, Γ, between the QD and the back-electrode matches or exceeds the resonance frequency, ω, of the cantilever (Figure 4.1). Since mechanical oscillators typically have a fixed ω, one usually needs to adjust the tunneling rate of the barrier to fulfill this condition. This can be achieved by controlling the thickness of the insulator.

Successful measurements of single-electron charging of QDs have been performed on junctions of different materials. For example, Cockins et al.[23] have measured the single-electron charging of InAs QDs sitting on a 20 nm InP insulating layer on top of a InGaAs two dimensional electron gas. Tekiel et al.[92] performed similar determinations on Au clusters sitting on a 1.7 nm insulating layer of NaCl above a Fe back-electrode. Sample preparations for these investigations were done by a technique in which material is evaporated under ultra-high vacuum while the growth of the condensed layer is monitored at the atomic scale. One of the limitations of this procedure, called molecular beam epitaxy, is that not every material can be evaporated without damage. For example, supramolecular assembly of Au NPs using DNA, which is an exciting new approach for the design of artificial molecules[3,102], does not tolerate heating. Consequently, alternative protocols need to be used to prepare sample junctions made of soft matter.

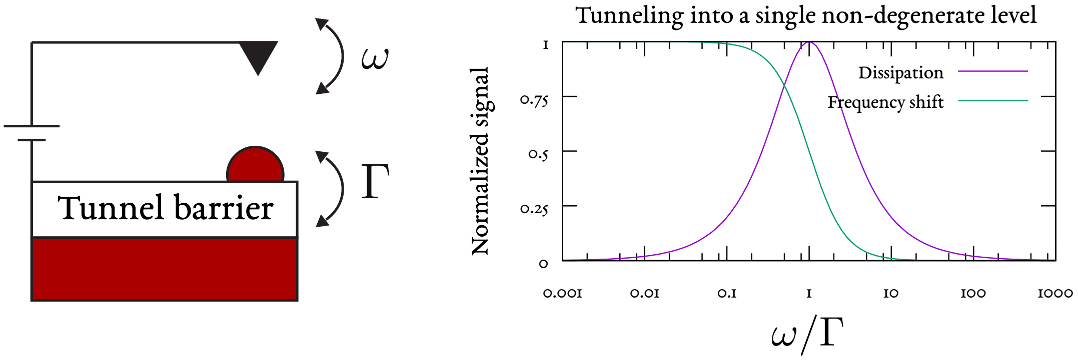

Figure 4.1: (a) Schematic of the oscillating cantilever with tip pushing electrons on and off a QD sitting on an insulator on top of a back-electrode. (b) Plot of the dissipation and resonance frequency shift response (in normalized units) versus the normalized tunneling rate (in units of the cantilever resonance frequency) in the case of tunneling into a single non-degenerate level.

In this chapter, I describe the low cost, wet lab approach adopted in the present work to electrically insulate Au NPs from a gold back-electrode by chemisorbing them on a self-assembled monolayer (SAM) of alkanethiols. The motivations behind the choice of these compounds were that they form a tunnel barrier whose tunneling rate depends exponentially with the length of the alkane chain[99,1], which can easily be adjusted during synthesis. Moreover, they offer a great potential for chemisorbing various types of nanostructures.

4.1 Gold thin films

Empirical observations have repeatedly revealed since the early 1980's that Au films provide an excellent support on which well-ordered SAMs form. As discussed by Love et al.[62], Au films have several characteristics making them attractive for the growth of SAMs. It is easy to obtain high purity Au and straightforward to prepare thin films by various deposition techniques, such as thermal evaporation, sputtering and electrodeposition. Gold binds strongly with thiols and permits the formation of SAMs that are stable for weeks with molecules having a thiol group. Gold is also a good conductor, thus allowing it to be used as a back-electrode. In this study, I prepared Au thin films by thermal evaporation under high vacuum (10^{-7} mbar) using a thin film deposition system (Thermionics Vacuum Products model VE-90) with an integrated quartz crystal deposition controller (Inficon XTC/2 from Leybold) and a specially designed heater to anneal the substrate during the formation of the Au film. A thermocouple positioned in the vicinity of the substrate was used to set the temperature using a CN9661 controller from Omega. The Au used for deposition was 99.99% pure.

To perform AFM experiments, it is crucial to prepare Au thin films with minimal surface roughness. Indeed, flat surfaces are desired for distinguishing Au NPs, or other deposited materials, from random height variations of the underlying surface. More importantly, a smooth surface is needed to grow well-ordered monolayers of molecules on

Au surfaces[61]. With the advent of STM/AFM in the late 1980's, the direct observation of surface morphology of metallic films became possible and spurred experimental efforts to produce flat Au surfaces (e.g., Vancea et al.[94]). The substrate on which the Au film is deposited is the first element to consider in preparing flat Au surfaces.

4.1.1 Direct evaporation on mica or glass

Mica is one of the favorite substrates for deposition of Au film because of the small mismatch with its crystal lattice which allows an epitactic growth of Au[50]. The first real-space images that resolve individual Au atoms on atomically flat terraces were notably obtained with mica by Hallmark et al.[44]. Subsequently, the effect of temperature on the surface roughness of Au on mica was investigated in several laboratories[19,29] and it was demonstrated that heating the substrate promotes larger crystallites with flatter tops as predicted by thermodynamic. It was found that atomically flat grains larger than 100 nm, which are suitable for our application, were obtained by heating the mica during the evaporation at 400°C.

Based on this literature, I thus initially set out to reproduce this result with mica that was freshly cleaved using a razor blade before being placed into the deposition chamber. However, AFM images of the resulting 100 nm thick films deposited at 0.1 nm s^{-1} did not exhibit large atomically flat grains as reported. The reproducibility of annealed Au film on mica was also questioned by Putnam et al.[71] and different thermal pre- or after-treatments of the samples have been recommended (e.g., Höpfner et al.[50]). Our observations also echo those of Hwang and Dubson[48] who couldn't produce smooth Au film on annealed mica at 500°C. These authors even observed that the optical appearance of the film could change when prepared at elevated temperatures. They suggested that this is likely due to mica undergoing dehydroxylation, a phenomenon whose importance may vary depending on the exact composition of the mica and that contributes to produce water under the growing film. Not only does mica has various compositions depending on its source[50], it is also difficult to consistently produce smooth and homogeneous substrates by cleaving mica under ambient conditions[94]. The unsatisfying results I got with mica led me to investigate other types of substrates for the deposition of Au film.

The use of glass as a substrate for the deposition of Au films is also common. Although it is an amorphous material, glass has been shown to produce Au surfaces with atomically flat terraces comparable to what was achieved with mica by Hwang and Dubson[48]. My attempts to use glass as a substrate were made with 0.15 mm thick glass cover slips (Corning no. 0211 cover glass) cut in small pieces of 1 cm^2 with a diamond saw. The pieces were cleaned by sonicating them in acetone, methanol and deionized water, and then blown dried with a stream of N_2. As expected, heating the glass during evaporation leads to the formation of much larger grains than what was achieved at ambient temperature. In Figure 4.2, the drastic effect that substrate heating has on the morphology of the Au surface is shown. Without heating, the diameter of the grains are smaller than about 50 nm, while heating the glass at 400°C during the evaporation allows to get atomically flat terraces larger than 200×200 nm^2 (0.04 μm^2).

However, because Au films deposited on glass are prone to delaminate when immersed in solutions for the growing of SAMs[30], it is necessary to have a 5–10 nm thick adhesive layer of Ti between the glass substrate and the Au film[89]. With this added layer, I observed the Au film degraded upon heating. In some cases, the color of the films became drastically different and exhibited very atypical low reflectivity in the visible spectrum. Moreover, x-ray photoelectron spectroscopy (XPS) measurements performed on the samples revealed clear peaks of Ti and TiO_2 at the surface. These observations

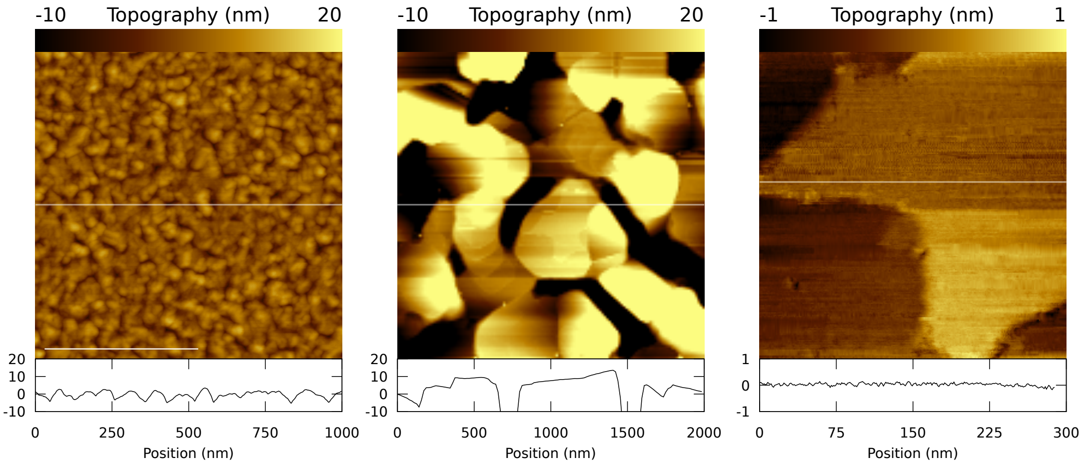

Figure 4.2: Atomic force microscopy images of a 100 nm thick Au film deposited on a glass substrate. Left panel (a) shows that the grains of the Au film deposited on a substrate that has not been heated are always $<$ 50 nm. Central panel (b) shows that the grains of the Au film formed on a 400°C substrate are significantly bigger ($>$200 nm). Right panel (c) is a zoomed in image of the central panel exhibiting an atomically flat terrace.

are consistent with those of Martinez et al.[64], who found that, at 250°C, Ti can fully migrate through a 260 nm polycrystalline Au layer and contaminate the surface when annealed for 10 hours. The diffusion of Ti into the gold layer therefore sets a clear constraint on the annealing temperature and time period needed to improve the flatness of the film.

4.1.2 Template stripping

Instead of optimizing the annealing procedure to avoid Au surface contamination, I turned my attention to the technique of template stripping (TS)[11,46,97,68,17,101,107]. This technique can produce flat Au with sub-nanometer roughness without the need for annealing. The idea of TS is to strip the Au film from the substrate and use bottom instead of top surface to grow SAMs (see Figure 4.3). If the Au evaporation is done on a flat substrate, the bottom surface of the Au layer should be similarly smooth. Although

Au can be template stripped from mica and glass, I decided to use Si wafers as done earlier[11,101] because this material can be mechanically and chemically polished at better than 0.1 nm roughness over the whole wafer and is convenient to manipulate.

A 100 nm thick Au film was thermally evaporated on the polished side of a Si wafer at room temperature. Before deposition, the wafer was ultra-sonicated in acetone, isopropanol and ethanol and subsequently blown dry using a strong stream of N_2. Evaporation was performed under vacuum (10^8 bar) at a rate of 0.1 nm s^{-1}. Another Si wafer was cut into small pieces (3 mm by 8 mm) to be used as supports that are epoxy-bonded to the Au surface. The pieces were cleaned using the procedure mentioned above. About 1 µL of Epotek 377 epoxy glue was placed onto the polished side of the Si supports using a micropipette. They were then placed on the Au coated Si wafer and the glue was cured at 150°C for 1 h. A razor blade is used to scrape the edges of an adhered Si support for the Si/epoxy/Au sandwich to pop off, resulting in the transfer of evaporated Au to the Si support. The transferred Au surfaces were imaged using a Veeco Nanoscope III STM and AFM in tapping mode. Sub-nanometer root-mean-square surface roughness was routinely obtained.

Examples of results obtained with the template stripping Au on Si are shown in Figure 4.4. Except for some large pits, the height variation of the surface is less than 2 nm per μm^2 (Figure 4.4a). Zooming in, we can clearly see atomic steps on the surface (Figure 4.4b). Although the global surface roughness is low, the size of atomically flat terraces is not as good as what was achieved on glass (Figure 4.2). Further post-treatment can be applied to improve the morphology of the template stripped Au surfaces. For example, I have observed that post-annealing the Au-coated wafer in air at 450°C for 4 min prior to stripping contributes to enlarge grain size as displayed in Figure 4.4c,d. However, it is unclear whether this treatment improves the roughness.

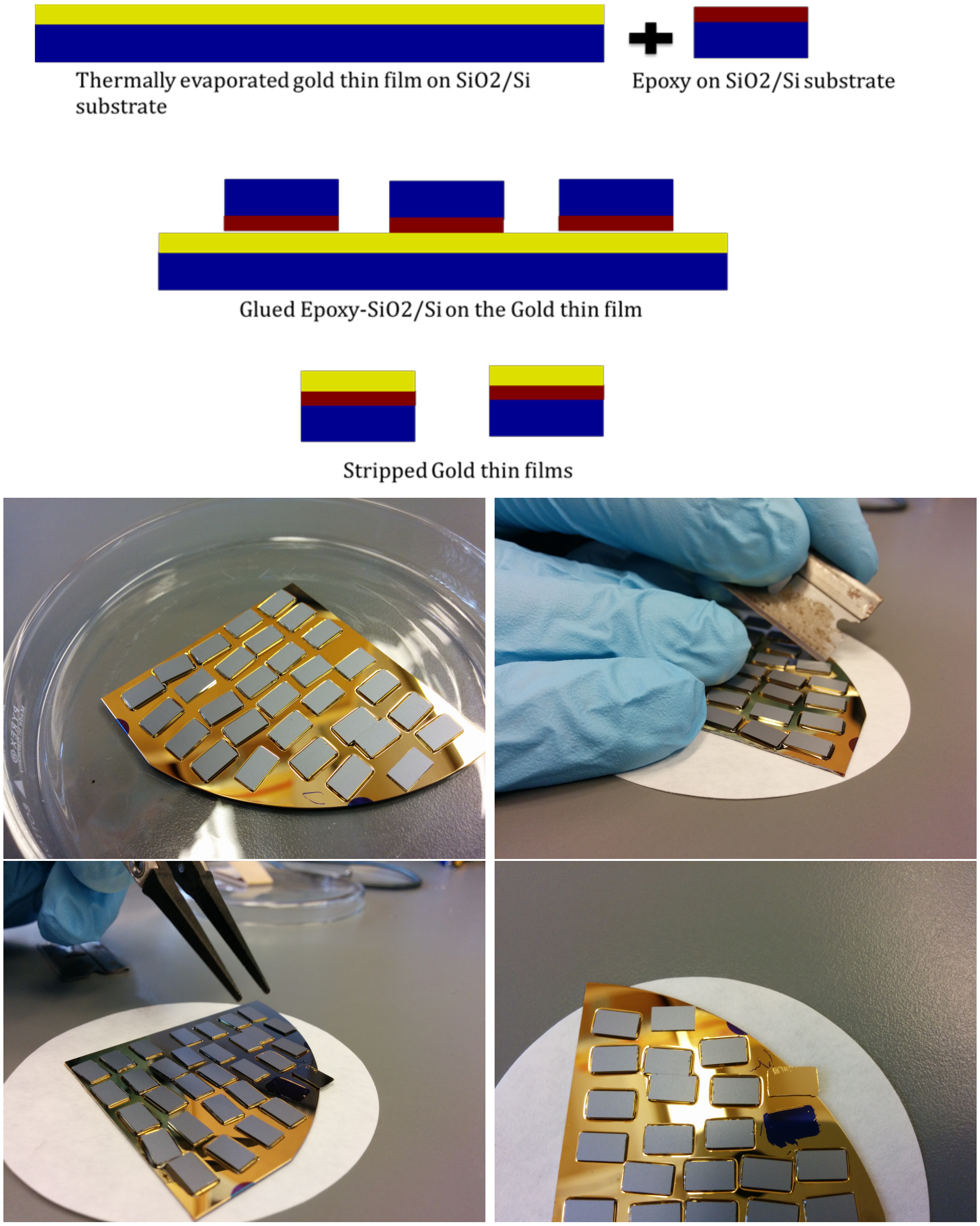

Figure 4.3: (A) Photos related to the protocol of template stripping Au: (a) Small Si pieces are epoxy-bonded to a Au-coated Si wafer; (b) The epoxy is cured in a furnace and small pieces stripped off with a razor blade; (c) Stripping off the small Si pieces transfers the Au film from the Si template to the small pieces; (d) A template-stripped Au surface ready for imaging. (B) Schematic illustrating the three important steps of the template stripping process: (a) Gold is evaporated onto a Si wafer and another one is cut into small pieces. (b) The small pieces are epoxy-bonded to the Au-coated wafer. (c) The small pieces are stripped off and the Au is transferred from the coated wafer to the small wafer pieces.

For instance, Banner et al.[11] reported lower roughness with annealing while Borukhin and Pokroy[16] reported higher roughness.

Electrochemical etching is a way to change the local roughness on an individual grain at the expense of deepening pits between grains.AFM images displayed in Figure 4.5 demonstrate how effective this process is. These images are those of an unannealed template stripped Au surface that was etched by sweeping four times the voltage from -0.2 V to 1.6 V at a rate of 20 mV s^{-1} in a 0.1 mM $HClO_4$ solution. As can be seen, there is a drastic reduction of the number of atomic steps on the top of the grains and atomically flat terraces larger than 200 nm are present.

However, this local reduction of roughness comes at the expense of a larger global roughness as the process digs trenches around the grains. A combination of annealing, which promotes larger grains, and electrochemical etching, which promotes atomically flat grains, has the potential of producing extremely large atomically flat terraces. As discussed in the next section, it turns out that a relatively low global roughness of template stripped Au was sufficient to grow insulating SAMs on which 5 nm and even 2 nm Au NPs can be attached and resolved with AFM. Therefore, electrochemical etching was not routinely included in our sample preparation procedure.

In conclusion, the advantages of the template stripping technique are numerous. First, the technique yields reproducible results as shown by AFM images in Figure 4.6 taken from two different samples prepared from different wafers. In addition to providing sub-nanometer surface roughness, samples can be stored for many months without oxidation and dust accumulation since the surface of interest is buried and unexposed to air. Lastly, a large number of samples can be produced in a single evaporation, thus reducing the turn-around time involved in preparing SAMs.

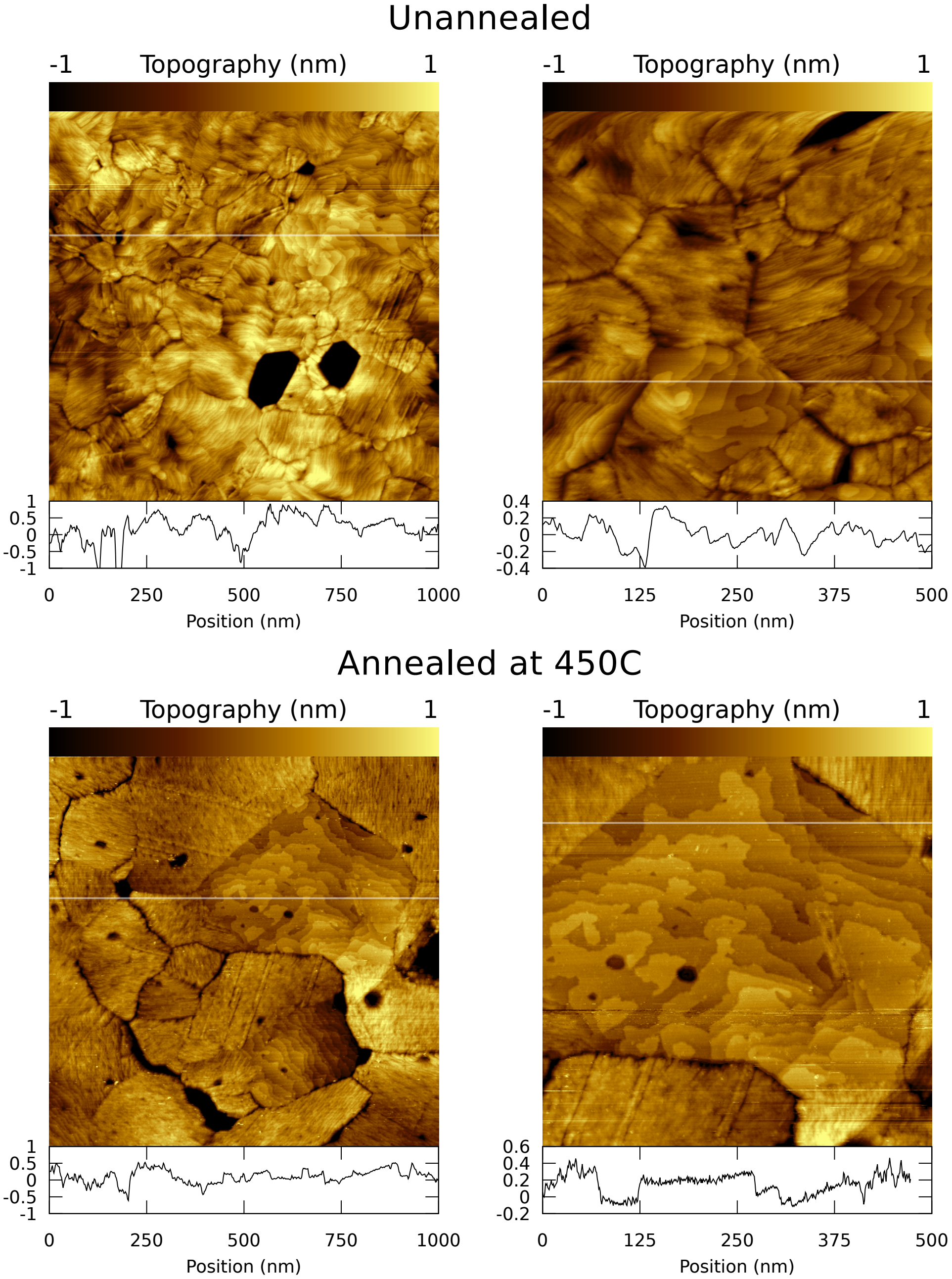

Figure 4.4: STM flattened images of template stripped Au. Panels (a) and (b) show an unannealed sample. Panels (c) and (d) show annealed sample at 450°C for 4 min. Images in lef and right panels cover sample areas of 1 μm^2 and 0.5 μm^2, respectively.

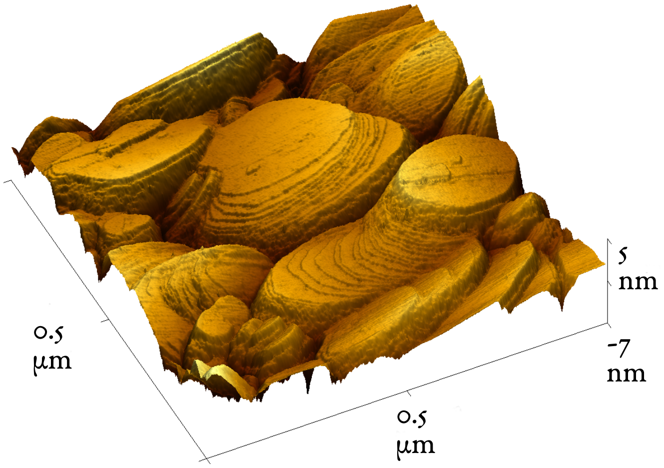

Figure 4.5: Tapping mode topographic images of template stripped Au electrochemically etched by sweeping four times the voltage from -0.2 V to 1.6 V at a rate of 20 mV s^{-1} in a 0.1 mM $HClO_4$ solution. Image representing a sample area of 0.25 $µm^2$.

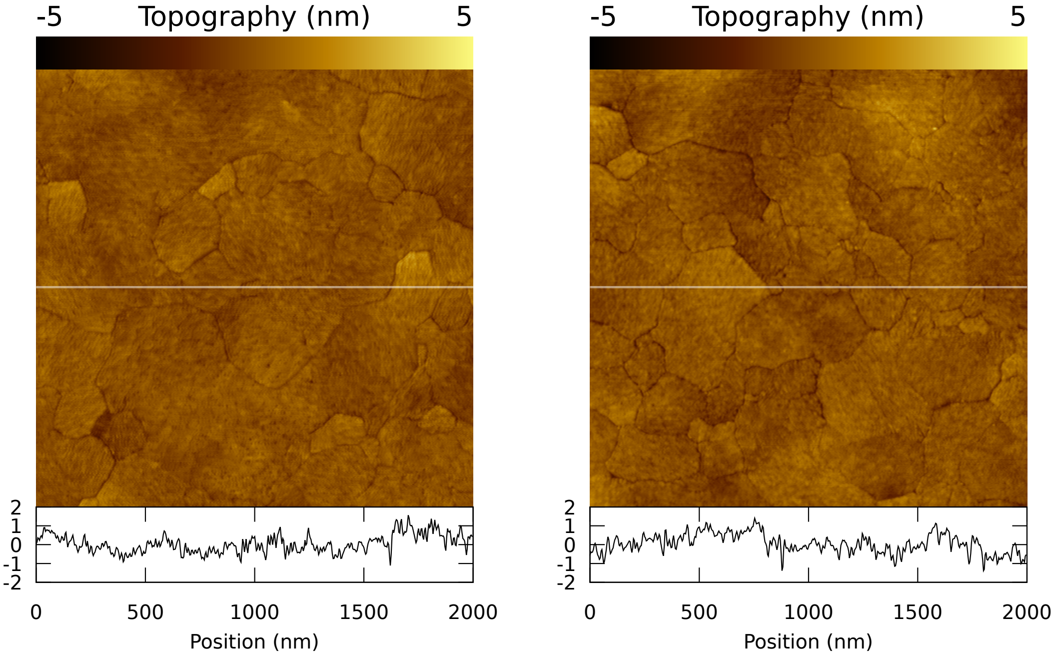

Figure 4.6: AFM images of template stripped Au annealed at 350°C for 3 h prepared from different wafers. The samples are similar with peak to peak height variation smaller than 3 nm

4.2 SELF-ASSEMBLED MONOLAYERS OF ALKANETHIOLS ON GOLD

Self-assembled monolayers of alkanethiols form on Au substrates by spontaneous adsorption from either liquid or vapor phase[62]. Deposition from solution of such organosulfur compounds is convenient and inexpensive. The most common protocol consists of immersing a freshly prepared and clean Au substrate into a dilute (1-10 mM) solution for hours to weeks[62,81]. This simple and widely used method provides organic interfaces with acceptable characteristics for many applications, including thin films acting as barrier to electron transport. Many precautions are nevertheless required to get surface topography of SAMs free of over layers of adsorbates at a micron scale allowing a clear distinction of the NPs subsequently deposited.

My initial experiments were performed at ambient condition as follow. A solution of alkanethiols in anhydrous ethnaol was vigorously mixed until complete dissolution. Typical concentrations of the solutions were in the range of 1 to 10 mM. All polyethylene containers utilized were previously rinsed three times with ethanol. Freshly cleaved template stripped Au substrates were immersed in small vials containing alkanethiols solutions for a certain period of time. The substrates were then taken out of the vial and rinsed by squirting ethanol for 15-30 s. A mixed SAM, consisting of different molecules, can also be grown by doing a two-steps incubation in which the substrate is immersed in a second solution and cleaned again. Finally, the samples were blown dried under a steady stream of N_2 and examined by AFM.

In Figure 4.7, AFM images of various samples prepared with this technique are presented. The left panel (a) is an image of a sample incubated in a 1 mM tetradecanethiol (C14S1) solution for 22 h showing aggregates that can be confounded with NPs. Additional samples prepared exactly the same way were subsequently incubated in 1 mM and

5 mM hexadecanedithiol (C16S2) solutions for 3.5 h. The resulting surfaces obtained are shown in panels (b) and (c) of Figure 4.7, respectively. Again, these surfaces show a high density of aggregates and are consequently less than ideal. Interestingly, the sample incubated at a concentration of 5 mM exhibits adsorbates shaped filaments, which suggest that alkanethiols are forming polymers. This indicates that when depositing long alkanethiols on Au film, solution concentrations below 5 mM should be preferred to hinder this effect. Although the deposition of SAMs from solutions may seem trivial, these deceiving results highlight the necessity to carefully control the experimental conditions in order to produce clean SAMs at the micron scale.

One important factor to consider, aside from ensuring the purity of the solution, is the potential that alkanethiols have to form multilayers on Au[62,70,52]. Although the mechanism by which this happen is unclear, Woodward et al.[106] observed the growth of alkanethiol bilayers islands, a result that I also noticed on some of my samples (Figure 4.8). Similarly to the finding of Woodward et al.[106], I found the presence on the Au film of many islands having a uniform height that is roughly twice the thickness of a monolayer, i.e. approximately 2 nm for a monolayer of C16S2[9,106]. Through controlled experiments, Woodward et al.[106] showed that the formation of such islands is associated with the oxidation of the Au surface, thus strongly suggesting that sample preparation under ambient conditions is problematic and should be avoided to prevent the growth of monolayers free of over layers. Consequently, based on my own observations and on the scientific literature in the field, I started performing all my sample preparations under an inert atmosphere. By cleaving the Au substrate and handling the solutions in an argon-filled glove-box, I was able to routinely produce clean SAMs. Figure 4.9 shows a typical example of such a sample obtained by incubating the substrate in a 1 mM C16S2 solution for 7 days. The exhibited images on this figure, which were taken at spots

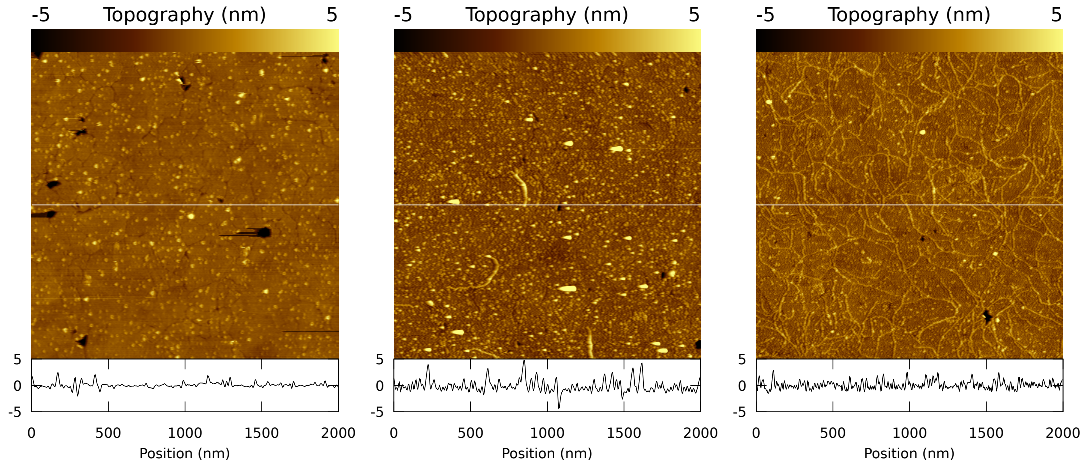

Figure 4.7: Left panel (a) shows an AFM image of template stripped Au incubated in a 1 mM C14S1 solution for 22 h. Middle panel (b) is an image of a sample prepared as that of panel (a), but that was subsequently incubated in a solution of 1mM C16S2 solution for 3.5 h. Right panel (c) is an image of a sample also prepared as that of panel (a) but subsequently incubated in a 5 mM C16S2 solution for 3.5 h.

mm away from each other, show flat surfaces with no aggregates. It should be noted that because the quality of the SAMs quickly degrades when exposed to air[104,59,80], my samples were maintained under an Ar atmosphere until AFM measurements were performed.

4.3 Deposition of Au NPs

Gold NPs have been used since ancient times for staining glass. Most notably, they conferred the 4th century Lycurgus Cup the property of changing color depending on the location of a light source[33]. In the modern world, they are widely used in research and technological applications for their unique optical and electronic properties[28]. Usually synthesized in a liquid phase, they form stable colloids when the van der Waals attraction is balanced by the electrostatic repulsion due to the so-called double layer of counterions as described by the classical Derjaguin-Landau-Verwey-Overbeek (DLVO)

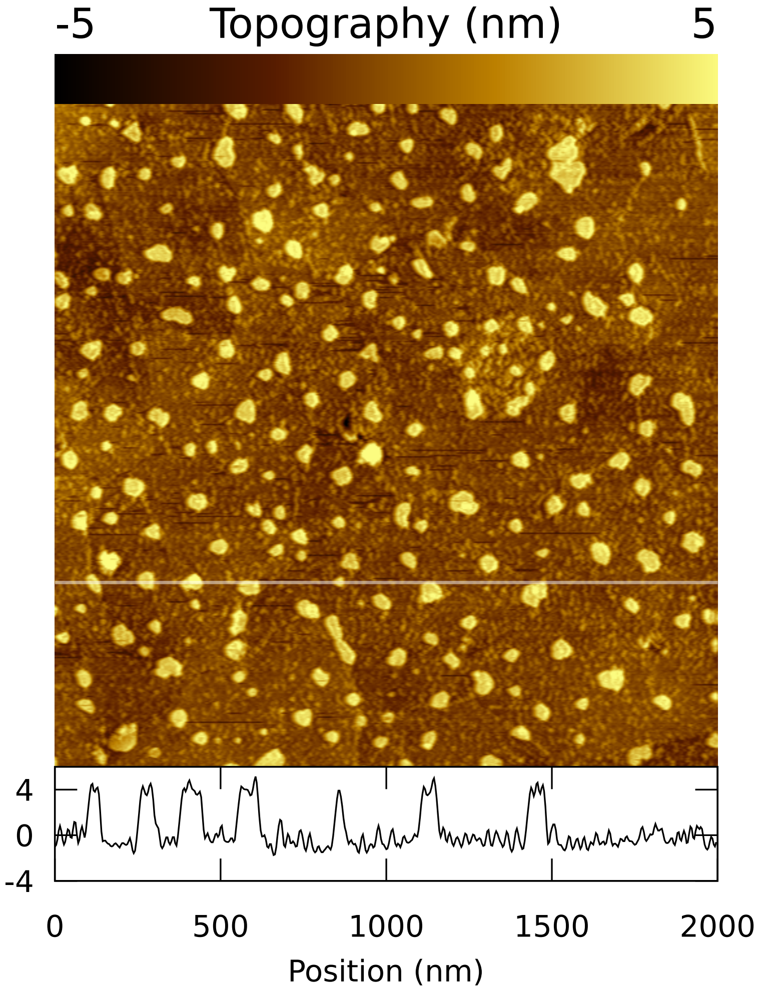

Figure 4.8: AFM image of a template stripped Au sample incubated in a 3 mM C14S1 solution for 24 h and then in a 1 mM C16S2 solution for 2 h. We see the formation of several islands of similar heights (4 nm).

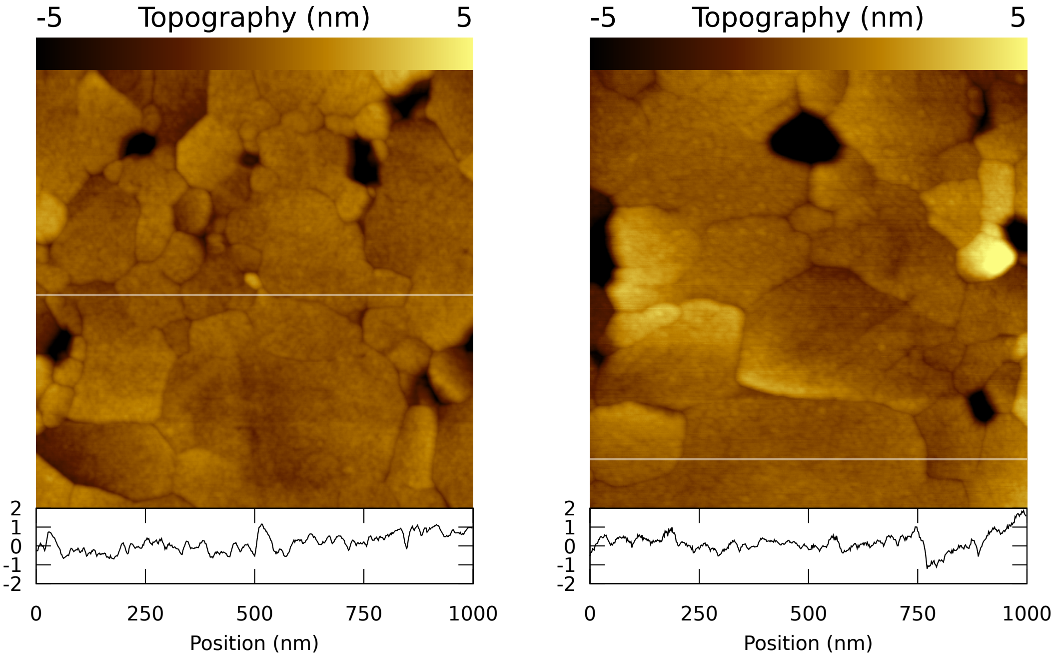

Figure 4.9: AFM images taken at two different locations millimeters away from one another of a template stripped Au sample incubated in a 1 mM C16S2 solution for 7 days.

theory[45]. In order to achieve this condition, one can tune the pH of the solution or coat the surface of the NPs with a stabilizing agent. Several well-established protocols[28] exist to produce and stabilize solutions of Au NPs of various sizes that are nowadays commercially available.

The deposition of Au NPs on SAMs of alkanedithiols is done by immersing the SAMs in a solution of Au NPs for them to adsorb on the surface[60]. The samples of Au NPs for which results are presented in this thesis were all prepared using a template stripped Au with a C16S2 SAM since they provide appropriate tunneling rate for our experiments as discussed in the next chapter. Due to thiol groups at both ends of the alkane chain, Au NPs form robust covalent bond, establishing stable electrical contact with the underlying molecules[27]. The deposition rate strongly depends on the pH of the solution and the coating of the NPs[39,109]. For example, I found that the deposition of 5 nm bare Au NPs (pH=5.97) and of 5 nm phosphine-coated Au NPs (pH=8.5) yielded strongly different numbers of deposited NPs for the same incubation time (24 h) and the same concentration of NPs in solution (80 nM). As shown in Figure 4.10, in the case of bare Au NPs, only two NPs were found in a µm^2. On the other hand, in the case of phosphine-coated NPs (4.10b), several NPs and even clusters of NPs were observed on the surface. As expected, the density of deposited NPs on the surface also depends on the incubation time and solution concentration of the NPs. For instance, I have found that the density of NPs decreased by a factor 10 when SAMs are incubated for 5 min instead of 1 h and that incubations for 1 h at a concentration of 8 nM instead of 80 nM yield a density of NPs 5 times smaller (Figure 4.11). As such, varying the incubation time and the concentration of the Au NPs provides a simple mean of controlling the density of deposited Au NPs.

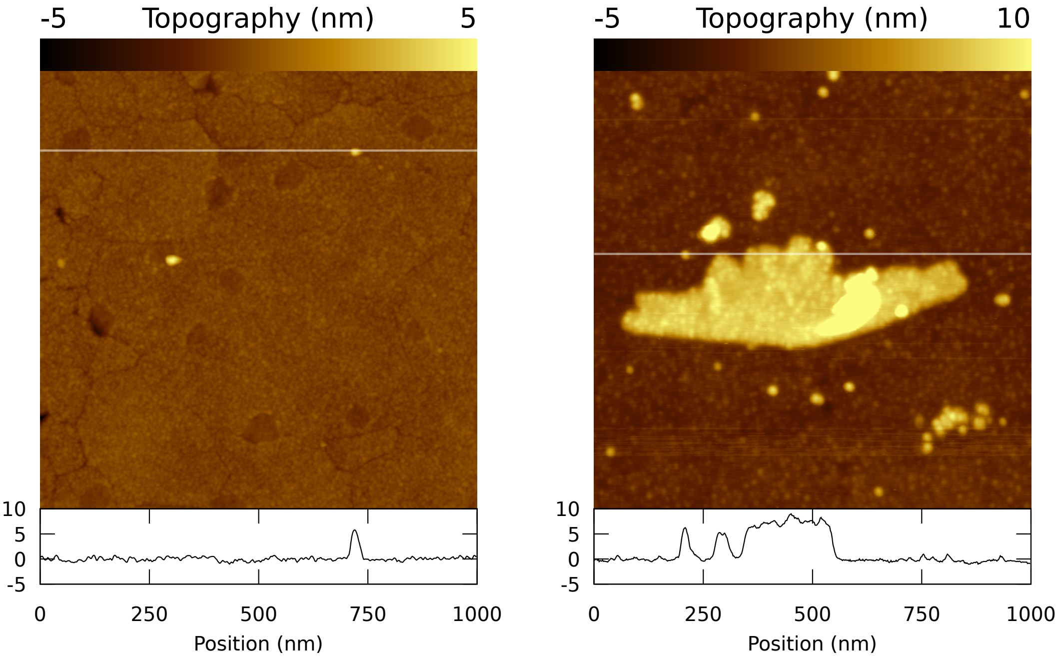

Figure 4.10: SAMs of C16S2 incubated in a 80 nM solution of 5 nm (a) bare Au NPs for 24 h and (b) phosphine coated Au NPs for 24 h.

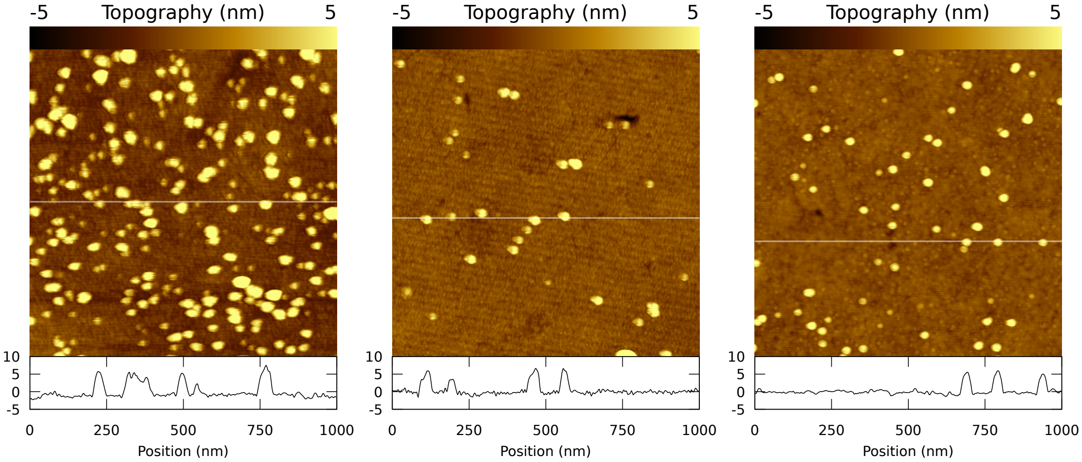

Figure 4.11: AFM images of C16S2 SAMs incubated in a solution of 5 nm phosphine coated NPs (a) 1 h at 80 nM, (b) 5 min at 80 nM and (c) 1 h at 8 nM.

4.4 Summary

The ideal sample for charging experiments should have a density of only few NPs per µm^2. Besides, the NPs have to be isolated from each other to facilitate measurements of individual particles. A good example of such a sample is given in Figure 4.12. The AFM image presented in this figure clearly shows 5 isolated NPs. Although the measured lateral size of these QDs is not accurate because of tip convolution, I can confirm from height profiles that the NPs have a diameter of roughly 5 nm as specified by the supplier. This density was obtained by incubating C16S2 SAMs in a 80 mM solution of bare 5 nm Au NPs for 48 h at a pH of 5.97. Interestingly, aside from the Au NPs, features of the underlying Au film are also captured in this AFM image. First, a deep pit is observed in the upper right corner of the image. This is commonly seen on template stripped Au surfaces on Si. Secondly, the grain boundaries of the polycrystalline Au film are also well resolved. The C16S2 SAM grown on the surface was obtained by incubating the Au substrate in a 1 mM C16S2 solution for a few days. At this concentration, Akkerman et al.[1] reported the presence of a looped phase where both thiol groups bind to the substrate. Shallow circular depressions seen throughout the image could point to the presence of such phase on the sample. Those defects in the insulating layer cover less than 15% of the surface and can easily be avoided. Extensive single-electron charging experiments were performed on this sample as discussed in the next chapter.

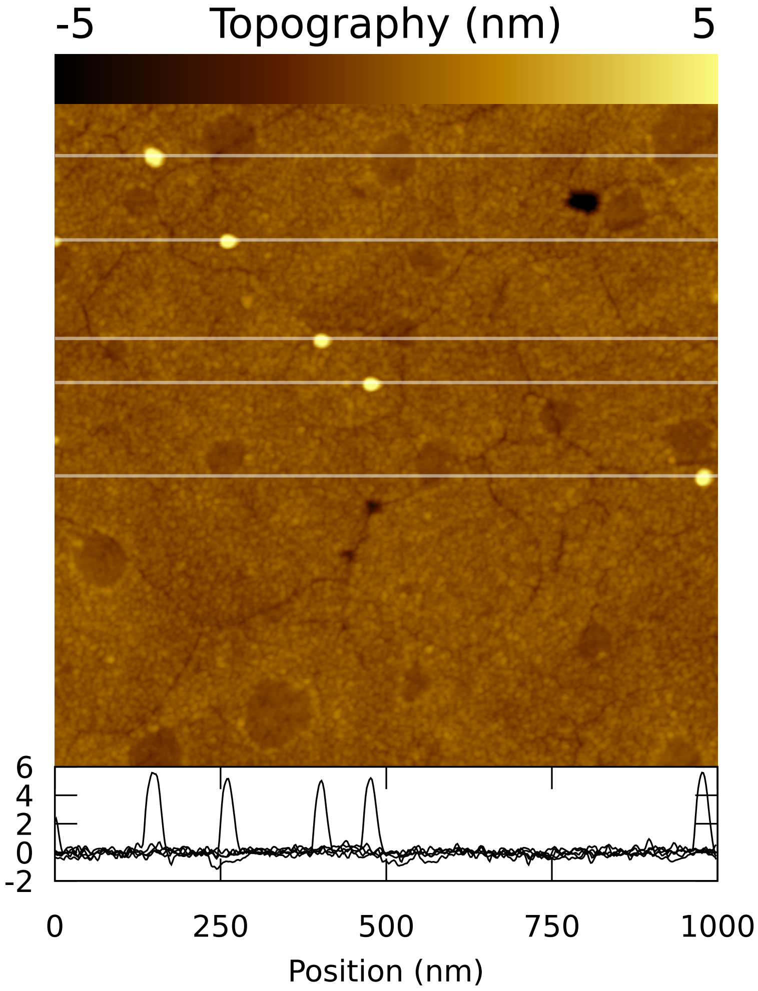

Figure 4.12: AFM image showing an ideal sample of 5 isolated NPs with diameters of roughly 5 nm. This sample was prepared by a C16S2 SAM in a 80 nM solution of bare 5 nm Au NPs for 48 h. Line profiles showing the height of each NPs (data taken along the white dashed horizontal lines).

5

Revealing energy level structure of individual quantum dots through tunneling rate spectroscopy

This chapter is based on

Revealing Energy Level Structure of Individual Quantum Dots by Tunneling Rate Measured by Single-Electron Sensitive Electrostatic Force Spectroscopy, Antoine Roy-Gobeil, Yoichi Miyahara, and Peter Grutter, *Nano Letters*, **15(4)**, pp 2324–2328, **2015**

Quantum dots have attracted a lot of interest in the past decades due to their novel electronic, optical and chemical properties. Of particular interest is their ability to control the number of confined electrons precisely when isolated by a tunnel barrier, which may lead to their incorporation in nanoelectronic devices[73].

Tremendous progress has been made to measure the electronic properties of various QDs such as electronic level structure and charging energy via various single-electron transport measurements including dc current measurement[54], charge sensing[?] and capacitance/admittance spectroscopy[5,26]. In these measurements, a series of peaks are observed in the measured signal versus gate voltage curves (Coulomb peaks). Although the separation of the peaks are indicative of the energy level structure, revealing the detail of electronic level structure such as identifying degenerate levels requires elaborate experiments which involve measurements with varying applied magnetic field[6,90] in order to separate the single-electron charging energy from the observed peak separations. Energy level spectroscopy has been possible only when the energy separation, $\Delta E_{\mathrm{level}}$, is much larger than thermal energy, $k_{\mathrm{B}}T$.

Scanning tunneling spectroscopy (STS) has also been successfully applied for energy level spectroscopy of colloidal QDs[65,10,95]. As such STS experiments need to be performed in double-barrier tunnel junction systems to measure a dc tunneling current, its applicability is thus limited to systems where a reliable tip-QD tunnel junction can be realized and the QD-substrate tunnel junction is transparent enough for a detectable tunneling current (typically > 1 pA). The former condition often requires a clean sample surface to be measured in ultra-high vacuum condition, limiting the kind of QDs which can be studied.

Electrostatic force microscopy with single-electron sensitivity (e-EFM) has been developed as an alternative way to probe single-electron transport in broader ranges of QDs such as epitaxially grown self-assembled and colloidal ones to which patterned electrodes are much more difficult to attach[108,22,91]. e-EFM technique alleviates this problem by using an oscillating AFM probe as a movable charge sensor as well as gate electrode. The technique yields peaks in the cantilever's resonance frequency shift and damping versus bias voltage curves (referred to as e-EFM spectra, hereafter) caused by single-electron tunneling, which carry the same information as Coulomb peaks measured in the above-mentioned transport measurements. Since it retains the imaging capabilities of AFM, it enables a systematic exploration of structure-property relationships, which is of central interest in nanotechnology.

In contrast with other single-electron charge detection experiments done by AFM[42,66] e-EFM technique provides not only the charge state of the sample but also the dynamics of tunneling single electrons, which enables quantitative spectroscopic measurement of energy level structure. For instance, Cockins *et al*[22] and Bennett *et al*[13] demonstrated that degenerate energy levels can be revealed by measuring the temperature-dependence or oscillation amplitude dependence of the e-EFM spectra. Excited energy levels have also been measured[25].

In this chapter, we show an alternative route to obtain such spectroscopic information by measuring the bias voltage dependent tunneling rate (tunneling rate spectrum), which can be measured easily by e-EFM technique. Fitting the experimental tunneling rate spectrum with the theoretical one using standard single-electron tunneling transport theory[12] has the potential to reveal the electronic energy level structure (density of states) of the QD even in the condition, $k_\mathrm{B}T \gg \Delta E_\mathrm{level}$ where the effect of ΔE_level on the peak separations are not discernible.

Measurements performed on 5 nm colloidal Au nanoparticles (Au NPs) at 77 K reveals a near continuous density of states. We then apply our analysis to already published data on self-assembled InAs QD measured at 4 K and show that degeneracies

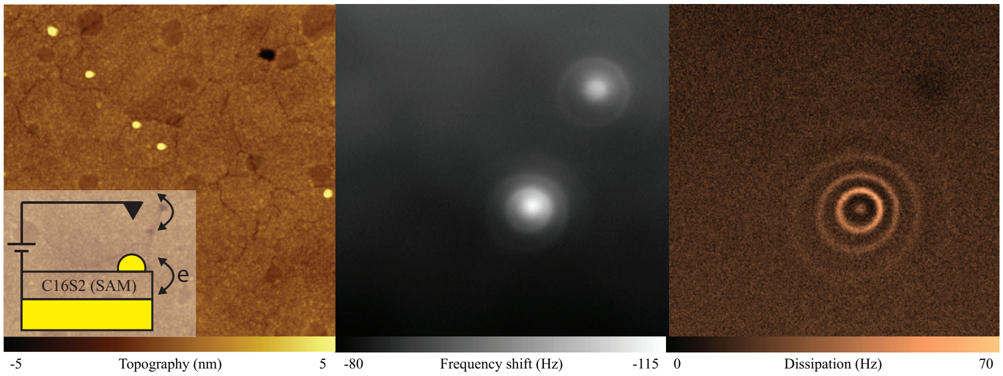

Figure 5.1: (Left) 1 $\mu\mathrm{m}^2$ tapping mode topography image of 5 nm Au colloidal nanoparticles on a self-assembled monolayer of 1,16-hexadecanedithiol (C16S2). (Inset) Schematic of the oscillating cantilever with tip pushing electrons on and off the QD when the bias voltage is enough to lift the Coulomb blockade. (Center and right) Simultaneously recorded frequency shift and dissipation images (200 nm by 200 nm) acquired at constant-height over two 5 nm Au nanoparticles with an applied tip bias of 7.7 V at 77 K. Peak-to-peak oscillation amplitude was 1 nm.

and shell-filling can be identified straightforwardly from a single tunneling-rate spectrum obtained from a single pair of frequency shift and dissipation peaks without performing variable temperature[22] or magnetic field experiments.

5.1 Theoretical model

In e-EFM, electron tunneling into and out of QDs happens through a single tunnel barrier while an AFM cantilever tip capacitively coupled to the QD is used both as a gate and charge sensor. Tunneling between the tip and QD is negligible because of their large separation (>10 nm). Tunneling between the back-electrode and QD is suppressed (Coulomb blockade) by the electrostatic energy cost (charging energy), E_{C}, of adding or removing an electron to the QD except near charge degeneracy points at which two successive charge states share the same energy.

A dc-bias voltage, V_{B}, is applied to the tip with respect to the grounded back-electrode (see inset of Figure 5.1, left panel) to overcome E_{C}. The potential drop, αV_{B}

($\alpha < 1$), across the tunnel barrier between the QD and the back-electrode determines the tunneling process and is only a fraction of V_B with lever arm, $\alpha(x, y, z) = C_\mathrm{tip}/C_\Sigma$, being a function of the tip-QD capacitance, $C_\mathrm{tip}(x, y, z)$, and total dot capacitance, $C_\Sigma = C_\mathrm{tip} + C_\mathrm{2DEG}$, where the coordinate, (x, y) and z, denotes the lateral and vertical position of the tip with respect to the QD, respectively.

For a small vertical cantilever tip motion compared to the average tip-QD distance, $C_\mathrm{tip}(x, y, z)$ varies linearly with z and we can write the charging Hamiltonian of the dot as[86]:

$$\begin{aligned} \mathcal{H} &= E_\mathrm{C}[(n - \mathcal{N})^2 - (1 - C_\mathrm{2DEG}/C_\mathrm{tip})\mathcal{N}^2] \\ &\simeq \mathcal{H}_{C,0} + Anz \end{aligned}$$

where $\mathcal{H}_{C,0}$ is an oscillator-independent part of the Hamiltonian, n is the number of electrons on the QD, $E_\mathrm{C} = e^2/2C_\Sigma$ is the charging energy, and $A = -(2E_\mathrm{C}V_\mathrm{B}/e)(1 - \alpha)\partial C_\mathrm{tip}/\partial z$ is the dot-cantilever coupling strength[22]. e-EFM experiments are performed in frequency modulation mode in which the cantilever oscillates at constant amplitude, a, and at its resonance frequency. In this mode, the oscillation of the cantilever tip modulates $\alpha(x, y, z)$ which leads to an effective oscillating gate voltage applied to the QD. At charge degeneracy points, this results in a modulation of the charge of the QD in response to the cantilever motion. The changes in the resonance frequency and dissipation, caused by the resultant ac electrostatic force can be measured with high sensitivity using frequency modulation techniques[2].

We model the time evolution of the charge state of the QD and the resulting back-action force in a regime where 0 or 1 extra electrons can reside on the QD with other charge states prohibited by Coulomb blockade. Within the orthodox model[32], its state can be described by the probability $P(t)$ of having an extra electron at time t. The evolution of this probability in time can be described by the following mean-field master equation[13]:

$$\partial_t \langle P \rangle = -\Gamma_-(\langle z \rangle)\langle P \rangle + \Gamma_+(\langle z \rangle)(1 - \langle P \rangle) \tag{5.1}$$

where Γ_+ (Γ_-) are z-dependent tunneling rates to add (remove) an electron to the QD. Due to the finite tunneling rate of electrons, $\langle P(t) \rangle$ is out of phase with respect to the cantilever oscillation, $\langle z(t) \rangle = a \cos \omega_0 t$, which results in a back-action force that causes a change in both its resonance frequency, $\Delta\omega/2\pi$, and its dissipation, $\Delta\gamma$, with magnitudes:

$$\Delta\omega = -\frac{\omega_0^2 A}{2\pi k_0 a} \int_0^{2\pi/\omega_0} dt \cos(\omega_0 t) \langle P(t) \rangle \tag{5.2}$$

$$\Delta\gamma = \frac{\omega_0^2 A}{\pi k_0 a} \int_0^{2\pi/\omega_0} dt \sin(\omega_0 t) \langle P(t) \rangle \tag{5.3}$$

where k_0 and ω_0 are the spring constant and resonance frequency of the cantilever, respectively and the values with $\langle\rangle$ denote their expectation value.

In the regime of weak coupling ($a \ll z_0$), tunneling rates vary linearly with z, and the above expressions reduce to:

$$\Delta\omega = -\frac{\omega_0 A^2}{2k_0} \frac{(\Gamma'_+ \Gamma_\Sigma - \Gamma_+ \Gamma'_\Sigma)}{(\Gamma_\Sigma^2 + \omega^2)} \tag{5.4}$$

$$\Delta\gamma = \frac{\omega_0^2 A^2}{k_0 \Gamma_\Sigma} \frac{(\Gamma'_+ \Gamma_\Sigma - \Gamma_+ \Gamma'_\Sigma)}{(\Gamma_\Sigma^2 + \omega^2)} \tag{5.5}$$

where $\Gamma_\Sigma = \Gamma_+ + \Gamma_-$ is the total tunneling rate and $'$ denotes derivative with respect to energy. The total tunneling rate between the QD and the back-electrode, Γ_Σ, can be directly measured as a function of the electrochemical potential detuning by noting that:

$$\Gamma_{\Sigma} = -2\omega_0 \frac{\Delta\omega}{\Delta\gamma} \tag{5.6}$$

It is by virtue of this relation that the measurement of the energy-dependent tunneling rate is straightforward with e-EFM technique, whereas the conventional transport measurement does not allow this measurement easily. To extract the electronic level structure of the QD from the experimentally obtained energy dependence of Γ_{Σ}, we rely on standard single-electron tunneling transport theory[12]. Using Fermi's golden rule, the electron tunneling rate between the QD and back-electrode are given by the following summations over all energy levels, k, of the QD with respective coupling strength to the electrode, Γ_k, and energy E_k :

$$\begin{aligned} \Gamma_+ &= \sum_k \Gamma_k \left[1 - F_{eq}(E_k|n-1)\right] f(E_k + \Delta E) & (5.7) \\ \Gamma_- &= \sum_k \Gamma_k F_{eq}(E_k|n) \left[1 - f(E_k + \Delta E)\right] & (5.8) \end{aligned}$$

where ΔE is the electrochemical potential difference between the QD and electrode is determined by αV_{B}. f is the Fermi distribution function and $F_{eq}(E_k|n)$ is the conditional probability of having level k occupied when n electrons are contained in the QD in equilibrium. Those expressions reduce to analytical solutions under certain conditions which we summarize in Table 5.1.

In the limit of high temperature ($k_{\mathrm{B}}T \gg \Delta E_{\mathrm{level}}$, classical regime), the discrete energy spectrum of the QD may be treated as a continuum of energy levels with density of states, ρ, and one may approximate $F_{eq}(E_k|n)$ by the Fermi-Dirac distribution[12].By neglecting the energy dependence of the density of states, ρ, and of the tunnel coupling

Case	Γ_+	Γ_-	Γ_Σ
Single non-degenerate level	$\Gamma f(\Delta E)$	$\Gamma(1 - f(\Delta E))$	Γ
Single degenerate level	$(\nu - n_{\text{shell}})\Gamma f(\Delta E)$	$(n_{\text{shell}} + 1)\Gamma(1 - f(\Delta E))$	$(\nu - n_{\text{shell}})\Gamma f(\Delta E)$ $+(n_{\text{shell}} + 1)\Gamma(1 - f(\Delta E))$
Continuous density of states	$\Gamma\rho\frac{1}{2}\frac{-\beta\Delta E}{1-e^{\beta\Delta E}}$	$\Gamma\rho\frac{1}{2}\frac{\beta\Delta E}{1-e^{-\beta\Delta E}}$	$\Gamma\rho\frac{1}{2}\beta\Delta E\coth(\frac{1}{2}\beta\Delta E)$

Table 5.1: Functional form of tunneling rate equations in limiting cases obtained from Eq. 5.7 and 5.8

.

strength, $\Gamma_k \equiv \Gamma$, the tunneling rates reduce to $\Gamma_\Sigma = \Gamma\rho\frac{1}{2}\beta\Delta E\coth(\frac{1}{2}\beta\Delta E)$ where $\beta = 1/k_{\text{B}}T$. The calculation also greatly simplifies in the limit of low temperature, ($k_{\text{B}}T \ll \Delta E_{\text{level}}$, quantum regime), where electrons fill the QD up to the Fermi level and $F_{eq}(E_n|n) = 1$. In this case, the total tunneling rate $\Gamma_\Sigma = \Gamma_+ + \Gamma_-$ is constant for a single non-degenerate energy level. Table 5.1 also contains formulas for the tunneling rates involved with ν-fold degenerate levels with shell-filling n_{shell} assuming constant Γ_k[22]. The expected total tunneling rate for cases relevant to our measurements are plotted in Figure 5.2.

We stress that although the expressions for the tunneling rate greatly simplify for those cases, the utility of the technique is not limited to them. On the contrary, by tuning the parameters of Eqs. 5.7-5.8 and numerically computing the associated tunneling rates, more accurate and detailed energy level structure can be obtained from the measurements. For example, measuring the transition from high to low temperature limit has the potential of revealing the electron distribution, $F_{eq}(E_k|n)$, at intermediate temperatures[12].

Experimentally, in order to achieve sufficient signal-to-noise ratio, it is ideal to operate in a regime where the cantilever's response is evenly split between $\Delta\omega$ and $\Delta\gamma$. This condition is met when the effective tunneling rate matches the resonance frequency of the cantilever[108,91].Since mechanical oscillators typically have a fixed ω_0, one usually

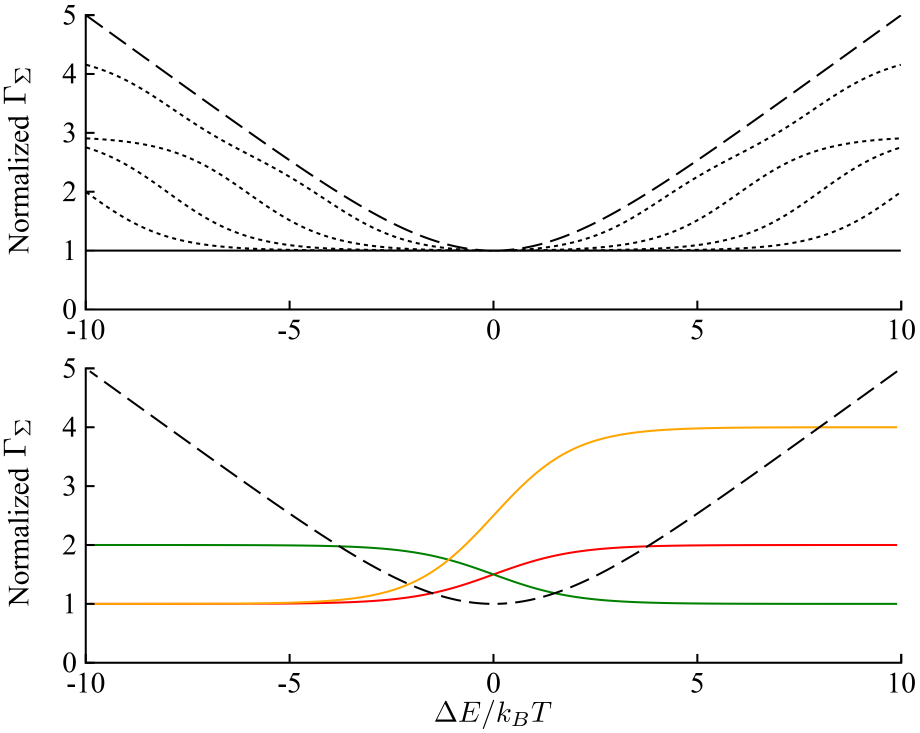

Figure 5.2: Theoretical total tunneling rate as a function of electrochemical potential detuning ΔE. (Top) QD with an infinite number of equally spaced non-degenerate energy levels. The solid line is for a single non-degenerate level (flat) and the long-dashed line is for a continuous density of states with $\rho = 1$. Short-dashed lines are numerically evaluated for energy level spacing of 4,6,8 and 10 $k_{\mathrm{B}}T$ assuming $F_{eq}(E_k|n) = f$ for simplicity. (Bottom) QD with a single degenerate level. A two-fold degenerate level yields the red and green curves with respective shell-filling, n_{shell}, equals to 0 and 1. The orange curve is for a four-fold degenerate level with $n_{\text{shell}} = 0$.

needs to adjust the tunneling rate of the barrier to achieve this condition.

5.2 METHODS

For the study of Au NPs, alkanethiol molecules are a perfect candidate for the design of such barrier because of an exponential dependence of tunneling rate on the molecular length[98] and their high affinity for gold on which they are known to grow self-assembled monolayers (see chapter 4). In this experiment, we show that a SAM of

1,16-hexadecanedithiol (C16S2) separating 5 nm Au NPs from a Au back-electrode provides a tunneling rate that roughly matches the resonance frequency of our cantilever, $\omega_0/2\pi = 160$ kHz. The sample was prepared as described in chapter 4 by immersing a flat gold substrate in a solution of C16S2 at 1 mM for a few days. Finally, the substrate was immersed in a solution of 5 nm Au NPs for them to chemisorb on the SAM.

e-EFM experiment were performed with a home-built low temperature AFM[75]. The spring constant of the cantilever, k_0, is about 40 N/m and its quality factor (Q) varies between 15,000 and 50,000 depending on the temperature. The cantilever is self-excited at its resonant frequency by feeding back its deflection signal into a piezoelectric excitation system via an oscillation control electronics. The oscillation amplitude is kept constant by controlling the amplitude of the cantilever excitation signal, A_{exc}, with a proportional integral controller. To compare acquired spectra to theory, the parabolic background due to the capacitive force between the tip and the back-electrode is subtracted from the experimental frequency shift versus bias voltage curve. For the dissipation measurements, the measured excitation amplitude is first compensated for the crosstalk due to the effect of the piezoacoustic transfer function by using the curves taken off the QDs[58] and then is converted to units of hertz via $\frac{\omega_0}{Q}(\frac{A_{\mathrm{exc}}}{A_{\mathrm{exc0}}} - 1)$ where A_{exc0} is the excitation amplitude with no tip-sample interaction (See more detail of the conversion in Appendix A).

5.3 Results and discussion

Scanning the tip over the Au NPs/C16S2/Au sample at constant height and with a fixed bias voltage shows rings of constant αV_{B} in frequency shift images (Figure 5.1, center panel) and dissipation (Figure 5.1, right panel) that are due to single-electron tunneling through the C16S2 SAM layer. The circular ring shape originates from the fact that the lever arm, $\alpha(x, y, z)$, which determines chemical potential detuning, ΔE, is just a function of the distance between the QD and tip, $r = \sqrt{x^2 + y^2 + z^2}$, such as $\alpha(x, y, z) = \alpha(r)$[22]. A pair of frequency shift and dissipation images such as Figure 5.1 (center and right panels) can provide the tunneling rate of each individual Au NP. Out of 9 Au NPs which we measured, 8 Au NPs exhibit the rings both in $\Delta\omega$ and $\Delta\gamma$, which show the tunneling rate ranging from 110 kHz to 830 kHz.(See Appendix A for more detail.) The top Au NP imaged in Figure 5.1 (center and right panels) shows a rare but instructive instance in which dissipation rings are too faint to be detected, which is indicative of a tunneling rate > 10 MHz. Estimated from the dissipation noise. This may be the result of the Au NP sitting on a thinner and more transparent barrier which could indicate the presence of defects in the SAM. This demonstrates the ability of e-EFM technique to measure the tunneling rate of each individual QD just by taking a pair of $\Delta\omega$ and $\Delta\gamma$ images and using the relation shown in Eq. 5.6.

Spectrum acquired at 77 K on 5 nm Au NPs shows single-electron tunneling events in both dissipation and frequency shift (see Figure 5.3). By fitting peaks with Eqs. 5.4 and 5.5, we obtain the lever-arm, α, of 0.064 and we measure a charging energy of 35 meV from the peak separation. The extracted total tunneling rate (Figure 5.3 Bottom) shows a clear signature of tunneling involving multiple levels in the QD as shown in Figure 5.2 and is in a good agreement with the analytical expression assuming a continuous density of states.

In order to demonstrate the generality and simplicity of this spectroscopy technique, we present similar measurements performed on epitaxially grown self-assembled InAs QDs on InP at 4 K (see[22] for experimental details and Appendix A for AFM images). In this case, the total tunneling rate (Figure 5.4 Bottom) shows a qualitatively different signature than in the classical regime. Looking at Figure 5.2 Bottom, we can easily tell

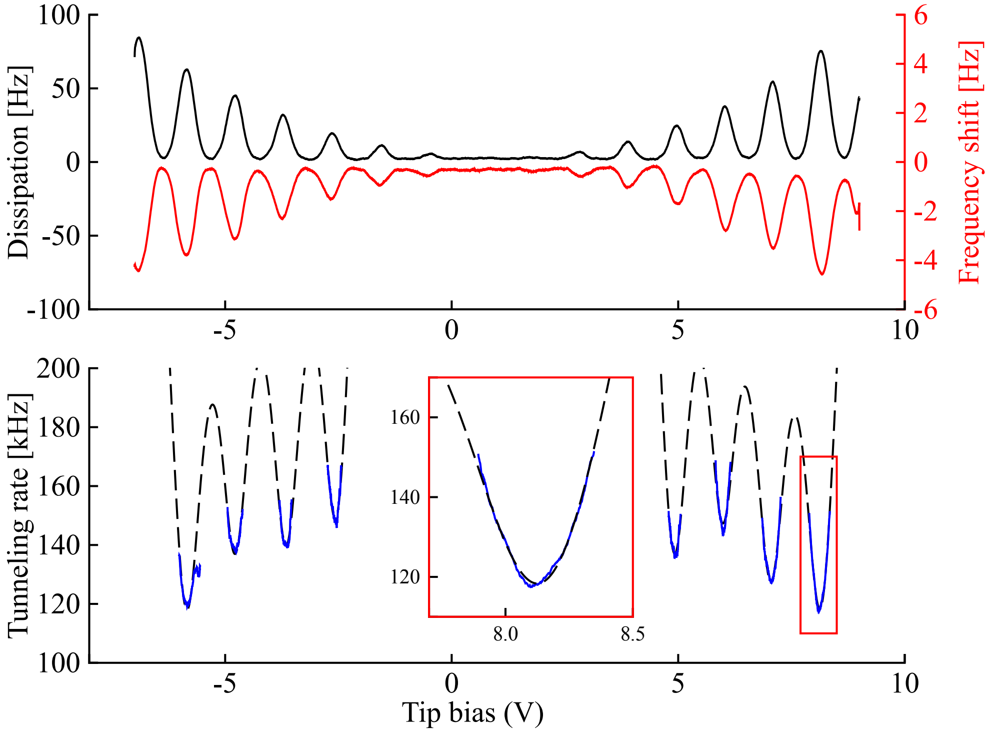

Figure 5.3: (Top) Experimental dissipation and frequency shift spectrum for 5 nm Au NP measured at 77 K. (Bottom) Extracted tunneling rate data (blue) superimposed with a fit to the analytical expression for a continuous density of states (dashed line).

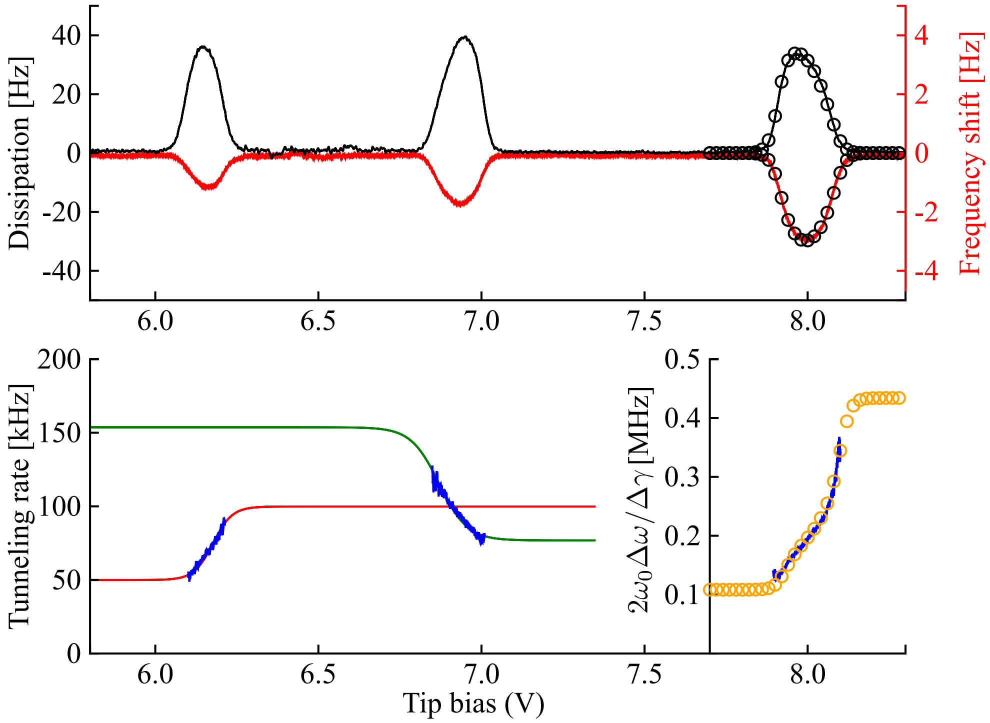

Figure 5.4: (Top) Experimental dissipation and frequency shift spectrum for InAs QD measured at 4 K. (Bottom) Corresponding tunneling rate data (blue) obtained from the data above superimposed with fits to tunneling rate expressions for two-fold degenerate levels (color scheme from Figure 5.2 is reused). Circles are a best fit solution assuming tunneling into an empty four-fold degenerate level and accounting for the effect of strong coupling.

it is indicative of electron tunneling into a single degenerate level of the QD. By fitting the data with the corresponding expression from Table 5.1, we find that the degeneracy, ν, has to be equal to 2 in order to properly fit the slope of Γ_Σ while the shell-filling, n_{shell}, is readily identified by the sign of the slope. This is in agreement with the results of a much more complicated measurement of a temperature-dependent level repulsion of peaks specific to this system[22]. At higher voltage, the weak coupling approximation start to break down and the ratio $2\omega_0\Delta\omega/\Delta\gamma$ is no longer equal to the tunneling rate Γ_Σ. Nevertheless, by looking at the slope of this ratio for the third peak, we can identify that tunneling occurs into an empty four-fold degenerate level but to properly fit the data, we had to numerically solve Eqs. 5.1-5.3 to account for the effect of strong coupling[13]. The method described here enables to extract such valuable information just by analyzing a single pair of peaks.

5.4 CONCLUSION

We have shown that by performing tunneling rate spectroscopy, AFM can be used to measure the density of states or the electronic structure of individual QDs. The system is simpler than double barrier scanning tunneling spectroscopy as only a single tunnel junction is involved. Moreover, since tunneling only occurs between the QD and back-electrode, this technique does not require a clean surface. Samples can be exposed to air, which greatly relaxes the constraints associated with sample preparation and ultimately collaboration with other labs. Finally, we note that the results presented here can be applied to other capacitance/admittance spectroscopy techniques which are recently emerging[5,6,26,35] and the presented theoretical analysis is applicable to the other tunneling rate measurements by single-electron counting technique[69].

6

Measuring reorganization energy of molecules

6.1 Introduction and goal

Single electron charging of molecules through various interfaces has been performed with STM/AFM tip in numerous laboratories (e.g., Gross et al.[41]), thus opening the way for studies of the effect of the environment (e.g., neighbouring molecules, interface defects) on electron transfer. In particular, Kocić et al.[53] demonstrated the periodic charging of individual molecules coupled to the motion of an AFM tip. However, not much information about the electronic properties of the molecules is extracted from their measurements. Interesting properties, such as the reorganization of the molecule's structure upon charging have yet to be taken into consideration and observed using AFM. The reorganization energy is particularly important since it plays a critical role in setting the electron transfer rates in various biochemical systems and is therefore a key parameter to measure[18]. In this chapter, I show how the reorganization energy can be measured with AFM and submit preliminary results supporting the approach.

6.2 THEORY

I consider the effect of the reorganization energy, λ, in a molecule where the energy level spacing is much larger than the thermal energy ($\Delta E_{level} \gg k_B T$). Upon adding an electron on the molecule, its energy level structure reorganizes and its energy levels are shifted down. Therefore, if λ is much larger than the thermal energy $k_B T$, an extra electron on the molecule cannot tunnel out because there is no energy level available in the electrode well below its Fermi level (Figure 6.1).

For simplicity, I take into account the reorganization energy λ in the framework of the classical Marcus theory[63]. To compute the tunneling rates in, Γ_+, and out, Γ_- of the molecule, I use Chidsey's formulation of the Marcus relationship which considers electron transfer with a metallic electrode[18,83,93]:

$$\Gamma_+ = \frac{\Gamma\rho}{\sqrt{4\pi\lambda^*}} \int_{-\infty}^{+\infty} - \exp\left(\frac{-[x-(\lambda^*+\Delta E^*)]^2}{4\lambda^*}\right) f(x)\,dx \tag{6.1}$$

$$\Gamma_- = \frac{\Gamma\rho}{\sqrt{4\pi\lambda^*}} \int_{-\infty}^{+\infty} - \exp\left(\frac{-[x-(\lambda^*-\Delta E^*)]^2}{4\lambda^*}\right) f(x)\,dx \tag{6.2}$$

where $\lambda^* = \lambda/k_B T$, $\Delta E^* = \Delta E/k_B T$, ρ is density of states in the electrode and Γ is the tunnel coupling strength. In Figure 6.2, the dependence of the tunneling rates with respect to the electrochemical potential difference ΔE, which equals $E_k - \mu_{res}$,

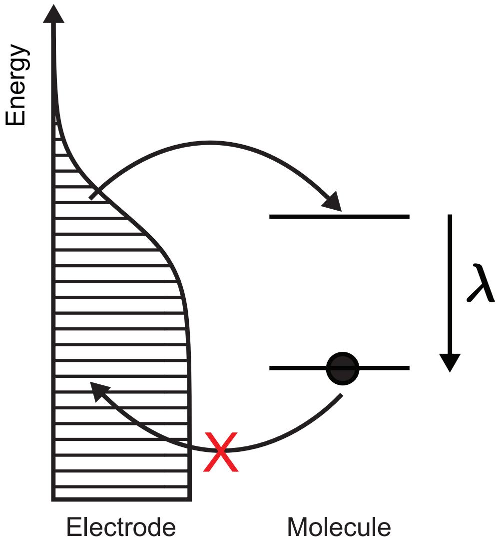

Figure 6.1: Illustration of electron tunneling between an electrode and a molecule. Upon charging, the level is shifted down by λ thus preventing an extra electron to tunnel out if λ is larger than k_BT.

is plotted for several values of λ. The total tunneling rate, $\Gamma_\Sigma = \Gamma_+ + \Gamma_-$, which is measured in experiments, has a distinctive shape depending on the value of λ. By doing tunneling rate spectroscopy as demonstrated in the previous chapter, one could measure the reorganization energy. However, if its effect is negligible, we expect to measure a constant Γ_Σ (see Figure 6.2).

The reorganization energy λ affects the measured frequency shift, $\Delta\omega$, and dissipation, $\Delta\gamma$, of the cantilever since they both depend on the tunneling rates. In the regime of linear response, they are simply given by[77]:

$$\Delta\omega = -\frac{\omega_0 A^2}{2k_0}\frac{(\Gamma'_+\Gamma_\Sigma - \Gamma_+\Gamma'_\Sigma)}{(\Gamma_\Sigma^2 + \omega^2)} \tag{6.3}$$

$$\Delta\gamma = \frac{\omega_0^2 A^2}{k_0\Gamma_\Sigma}\frac{(\Gamma'_+\Gamma_\Sigma - \Gamma_+\Gamma'_\Sigma)}{(\Gamma_\Sigma^2 + \omega^2)} \tag{6.4}$$

By using the tunneling rate expressions 6.1-6.2, we can numerically evaluate equations

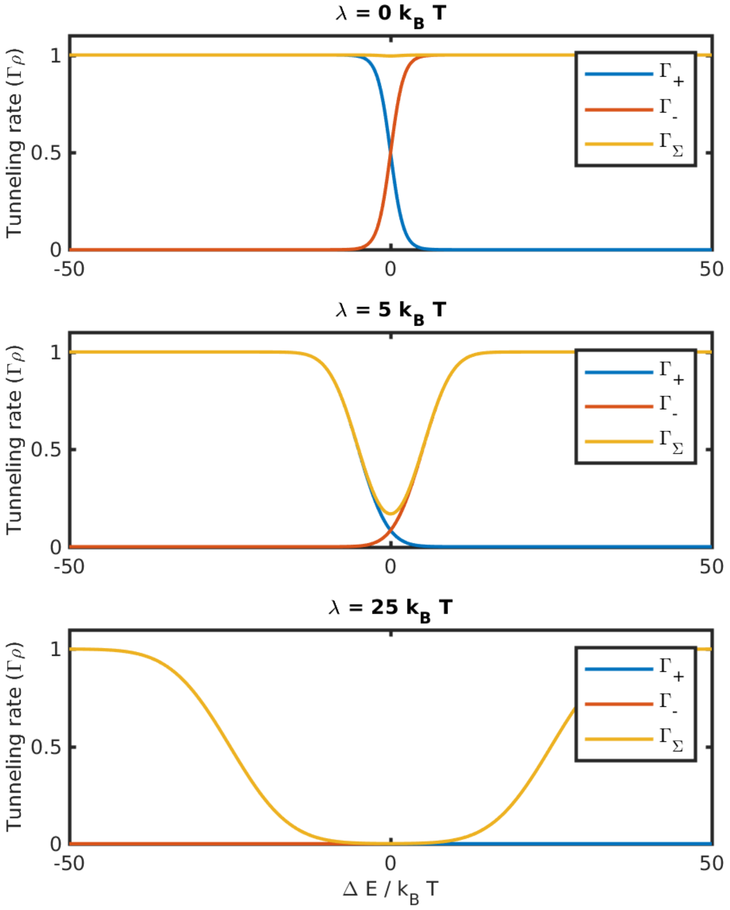

Figure 6.2: Tunneling rate in (Γ_+) and out (Γ_-) of a single non-degenerate level for different reorganization energy λ. The total tunneling rate $(\Gamma_\Sigma = \Gamma_+ + \Gamma_-)$ is also plotted and converges to $(\Gamma\rho)$ for large electrochemical potential difference ΔE.

6.3-6.4 to obtain $\Delta\omega$ and $\Delta\gamma$. As can be seen in Figure 6.3, molecules with large reorganization energy $(\lambda \gg k_B T)$ will yield extremely small signal because electrons cannot tunnel back to the electrode as described before.

The other key parameter that affects the tunneling rates beside λ, is the tunnel coupling strength of the level involved in the transport Γ_k. The computed maximum

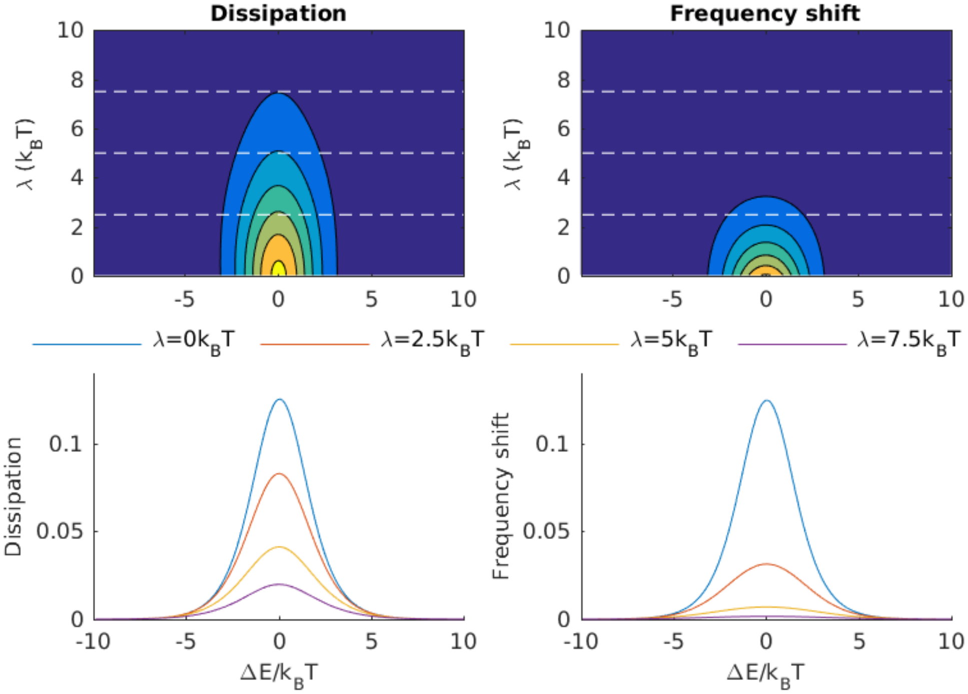

Figure 6.3: Frequency shift, $\Delta\omega$, and dissipation, $\Delta\gamma$, expected for tunneling into a single non-degenerate level for different reorganization energy λ. To generate the figures, the tunnel coupling, Γ, was set equal to the resonance frequency of the cantilever ω_0.

dissipation signal for different values of Γ_k and λ is plotted in Figure 6.4a. It can be seen that a non-zero reorganization energy can lead to a larger dissipation signal provided the tunnel barrier Γ_k is properly tuned.

6.2.1 Strong coupling

The tunnel barrier Γ_k can be tuned by changing the tunnel barrier but this is rather cumbersome. A simpler approach is to increase the oscillation amplitude, a, of the cantilever to enlarge the modulation of the electrochemical potential ΔE:

$$\Delta E = \Delta E_{dc} + Aa\cos(\omega t) \tag{6.5}$$

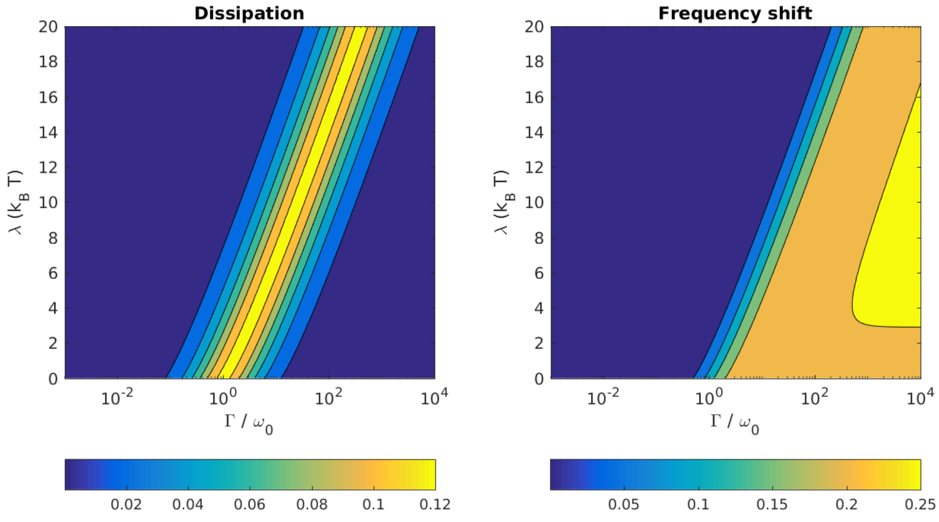

Figure 6.4: a) Maximum dissipation signal with respect to λ and Γ. b) Frequency shift at the associated electrochemical potential difference.

where $A = \partial_z \Delta E$ is the cantilever-molecule coupling strength. By swinging the cantilever hard enough, we may shift the Fermi level of the electrode low enough for an extra electron to tunnel back.

Using this approach, significant signal can be obtained even for non-zero λ values as shown in Figure 6.5. For the case of a λ value much smaller than the thermal energy, $k_B T$, increasing the oscillation amplitude, a, reduces the dissipation and frequency shift signal (Figure 6.5, top panel). In this case, minimizing a is recommended for measurements. However, when λ is larger than the thermal energy, increasing a enhance the signal. Indeed, there is an optimal oscillation amplitude that maximizes the signal (Figure 6.5, middle panel). Moreover, in the case of very large reorganization energy ($\lambda \gg k_B T$), using high oscillation amplitude is mandatory to get any signal (Figure 6.5, bottom panel).

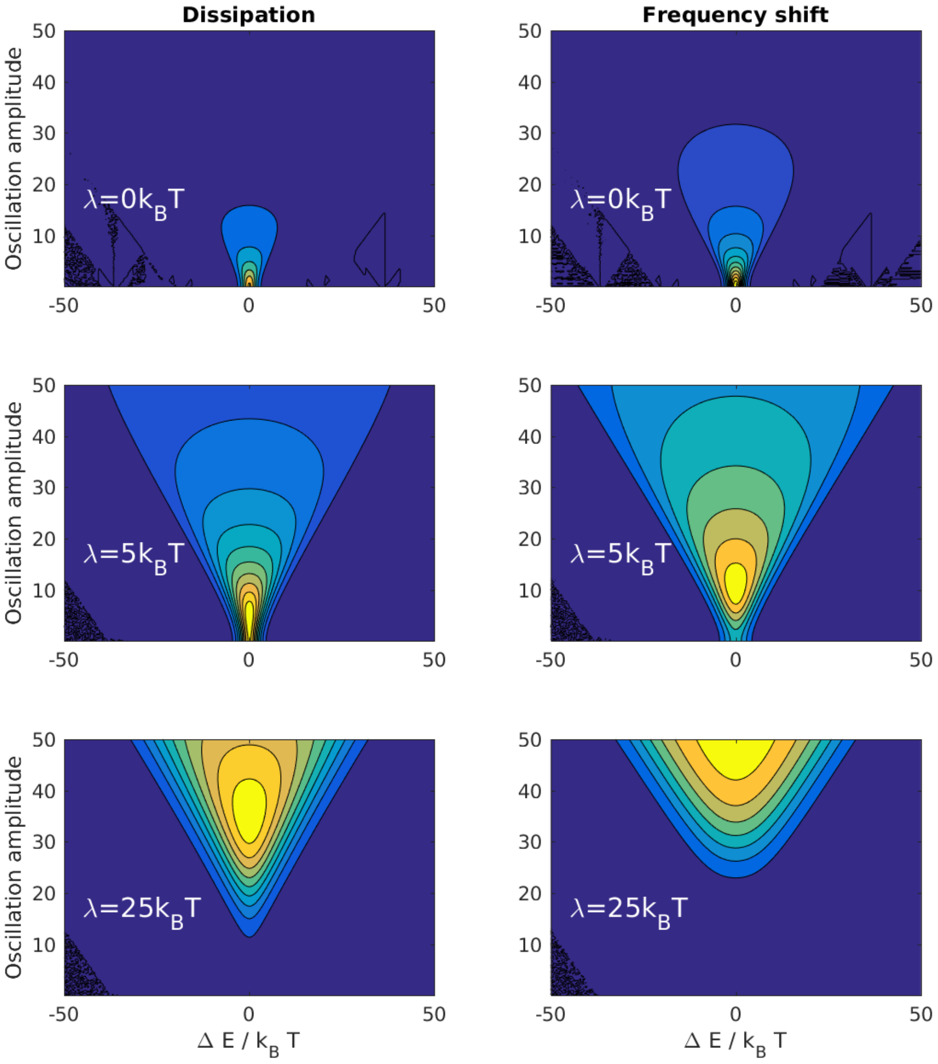

Figure 6.5: Dissipation (left column) and frequency shift (right column) as a function of electrochemical potential difference and oscillation amplitude normalized by k_BT. When $\lambda = 0$ (top), increasing the oscillation amplitude broaden the peak and reduce its maximum amplitude. For $\lambda = 25k_BT$ (middle), increasing the oscillation amplitude initially increases the peak amplitude before reducing it. Finally, when $\lambda = 50k_BT$ (bottom), a large oscillation amplitude is necessary to get appreciable signal.

6.3 PRELIMINARY RESULTS

Figure 6.6 illustrates a sequence of dissipation spectra acquired at different amplitudes on ferrocene ($Fe(C_5H_5)_2$) molecules attached to hexadecanethiols ($C_{16}S_1$) prepared through self-assembly of a monolayer on gold following the procedure described in Chapter 4. As one can see, the maximum dissipation signal is obtained for an amplitude of 150 pm which is both higher and larger than the spectrum acquired at 100 pm. This is a clear signature of non-zero reorganization energy, similarly to the trend theoretically predicted (Figure 6.5, middle panel). These preliminary results suggest that the reorganization energy of molecules upon charging can be measured by AFM.

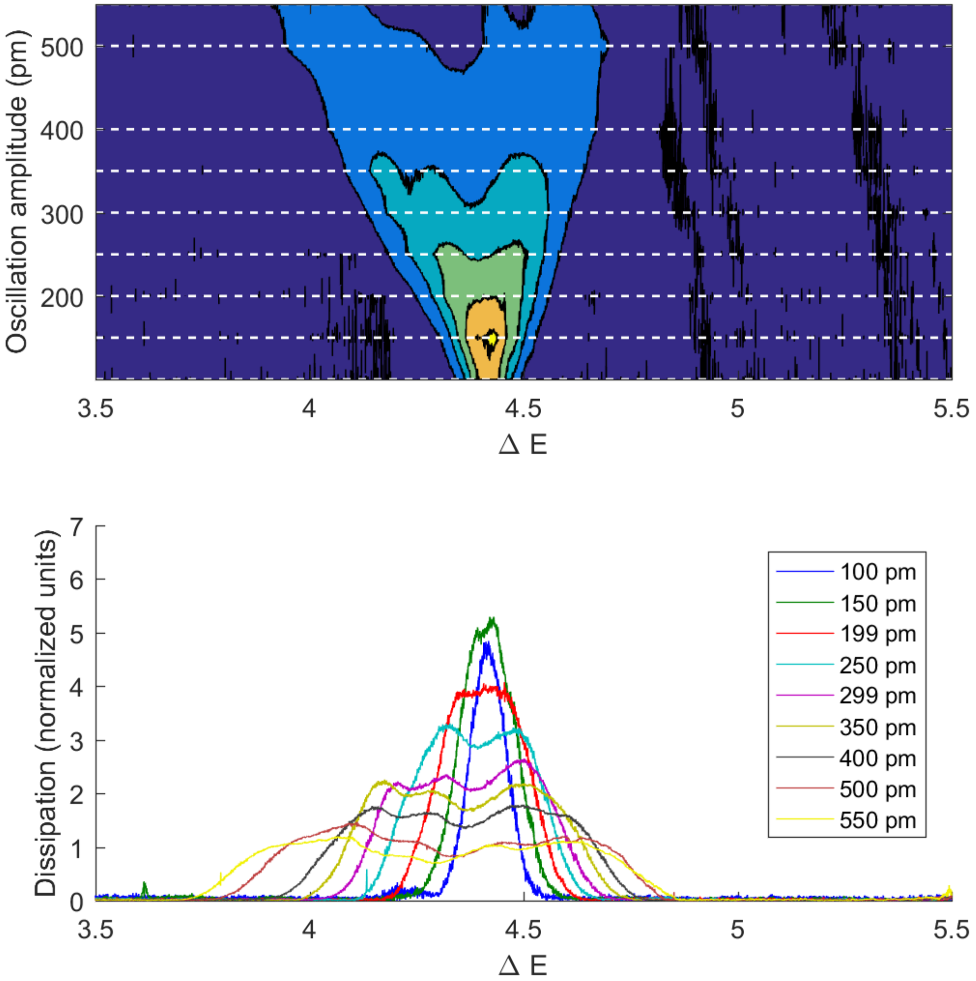

Figure 6.6: Set of dissipation spectra acquired with increasing oscillation amplitude on a ferrocene ($Fe(C_5H_5)_2$) molecules attached to hexadecanethiols ($C_{16}S_1$). The maximum signal is not obtained at the lowest oscillation amplitude. This indicates a non-zero reorganization as illustrated in Figure 6.5 (middle panel).

7

Conclusion

Due to its capability to image individual atoms in both organic and inorganic materials, atomic force microscope was already recognized before I initiated this thesis as a premiere characterization tool in nanotechnology. However, the ability of this instrument to quantify electronic properties of QDs and molecules was not, and is still not, fully appreciated by the scientific community.

In this thesis, I show how AFM can be used to perform spectroscopy of the electronic properties of nanostructures of various sizes through single-electron charging. This was achieved by measuring sequential tunnelling of electrons between a nanostructure of interest and a metallic back-electrode that forms a single-electron box with the AFM tip. I demonstrated that a linear response theory of the quantum nano-electromechanical system formed provides a straightforward way of interpreting experimental data. In particular, when using small tip oscillation amplitudes, the total tunneling rate is directly obtained from the ratio between the change in resonance frequency and the dissipation energy of the cantilever. This finding can be used to perform energy-dependent tunneling rate spectroscopy to reveal the electronic structure of a nanomaterial of interest. Although results obtained at larger tip oscillation amplitudes are more complex to interpret, I am also providing in this thesis an algorithm that allows computing promptly the response of the coupled electro-mechanical system. By using this algorithm, I notably report results that illustrate how the effect of large oscillation amplitudes can be used to measure the reorganization energy of organometallic molecules.

In order to obtain the aforementioned results, I have overcome critical experimental challenges. First, to accurately measure tip-sample dissipation, the non-flat transfer function of the excitation system was corrected. This important point is often overlooked by the AFM community with the consequence that results of dissipation measurements are often convoluted and extremely hard to analyze. This is likely one of the reasons why most publications in the field solely focus on frequency shift data and do not provide tunneling rate values. In this thesis, I have proposed the use of photothermal excitation to reduce apparent dissipation in experimental data, as well as a straightforward procedure to calibrate dissipation data in post-processing. Another important challenge for the measurement of tunneling rates using AFM is the attainment of a high quality signal to noise ratio in both measured frequency shift and dissipation. In the present doctoral research, I have demonstrated that this can be achieved by tuning the thickness of the insulating layer during the sample preparation. I showed that this can be accomplished at low-cost by using self-assembly.

Despite remarkable progress in recent years, there is still a lot of exciting opportunities to be seized and of experiments to be done in the field of single-electron charging using AFM. For instance, while this thesis has solely provided measurements of incoherent electron tunneling, AFM could be used to explore a wider range of quantum transport phenomena. In particular, AFM could be used to probe coherent tunneling in double quantum dots, thus opening the way to the exploration of the correspondence between assemblies of QDs and artificial molecules. Another potentially interesting research avenue would be to explore the properties of various exotic materials, such as supramolecular assembly of Au NPs using DNA, which could be deposited following the principles of sample preparation described in this thesis.

A

Chapter 5 - Supplementary information

A.1 STATISTICS OF MEASURED TUNNELING RATE

At 77K, we have seen charging rings in both frequency shift and dissipation images on 8 out of 9 nanoparticles observed (See an example image in Fig. S1).

For each NP, the tunneling rate associated with the most clearly resolved frequency shift/dissipation peaks is listed in Table 1.

Note that most values fall between 100 kHz and 1000 kHz.

Similarly, at 4 K, we have seen chargings ring on 5 different NPs. They all showed signal in both frequency shift and dissipation which again is indicative of a tunneling rate roughly matching the resonance frequency of the cantilever.

GNP	Tunneling rate, Γ (kHz)
1	110 ± 10
2	730 ± 20
3	170 ± 10
4	830 ± 50
5	210 ± 10
6	210 ± 10
7	240 ± 10
8	140 ± 10
9	>10000

Table S1: Measured tunneling rate of GNPs at 77 K using the most clearly resolved conductance peak.

A.2 CONVERSION OF DISSIPATION IN DIFFERENT UNITS

The unit of ω_0/Q is Hertz as Q is defined as follows:

$$Q = 2\pi \frac{E_{\mathrm{canti}}}{\Delta E_{\mathrm{loss}}} = 2\pi f_0 \frac{E_{\mathrm{canti}}}{\Delta E_{\mathrm{loss}} f_0} = \omega_0 \frac{E_{\mathrm{canti}}}{P_{\mathrm{loss}}} \tag{S1}$$

where

E_{canti} : Energy of oscillating cantilever [J]

ΔE_{loss} : Energy loss per one oscillation cycle [J/cycle]

P_{loss} : Energy loss per second (power loss) [J/s].

Recalling the definition of dissipation, γ_0,

$$\gamma_0 \equiv \frac{\omega_0}{Q} = \frac{P_{\mathrm{loss}}}{E_{\mathrm{canti}}}\,[1/\mathrm{s}] = \frac{P_{\mathrm{loss}}}{E_{\mathrm{canti}}}\,[\mathrm{Hz}] \tag{S2}$$

Dissipation in this notation means a fractional energy loss per second (fractional power loss). From Eq. S2, dissipation in Watts can be expressed as follows:

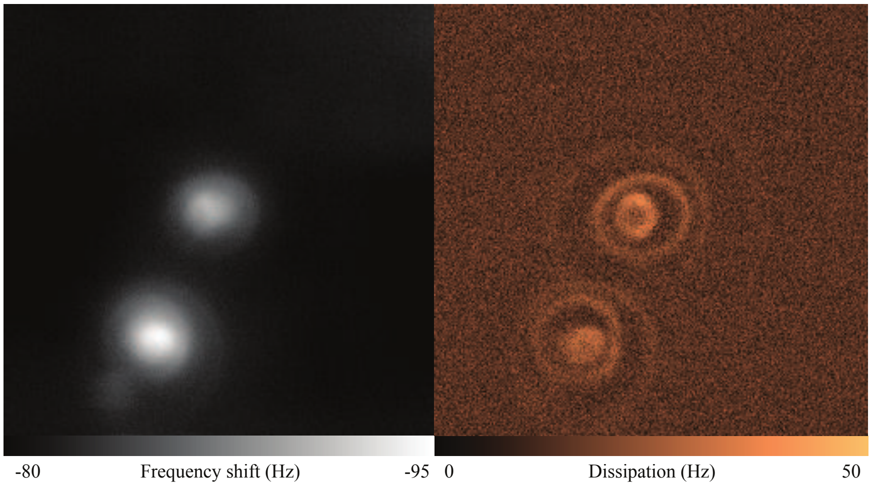

Figure S1: Another example of frequency shift and dissipation images taken at 77 K on other GNPs on the same sample discussed in the body text. Scanned size is 200 × 200 nm. Oscillation amplitude: 1.0 nm, $V_\mathrm{B} = 6.5$ V.

$$P_\mathrm{loss} = \frac{\omega_0}{Q} E_\mathrm{canti} = \gamma_0 E_\mathrm{canti} = \gamma_0 \frac{1}{2} k_0 a^2 \text{ [W]} \tag{S3}$$

where

k_0 : spring constant of cantilever [N/m]

a : cantilever oscillation amplitude [m]

The conversion factor from γ_0 [Hz] to P_loss [W] is thus E_canti.

In the same manner, dissipation per cycle can be expressed as follows:

$$\Delta E_\mathrm{loss} = \frac{P_\mathrm{loss}}{f_0} = \frac{E_\mathrm{canti}}{f_0} \gamma_0 \tag{S4}$$

The conversion factor from γ_0 [Hz] to P_loss [W] is E_canti/f_0.

For a cantilever with $f_0 = 160$ [kHz], $k_0 = 40$ [N/m], $a = 1$ [nm], the conversion factors are:

$E_\mathrm{canti} = 2.00 \times 10^{-17}$ [J] $= 1.25 \times 10^2$ [eV] and

$E_{\mathrm{canti}}/f_0 = 1.25 \times 10^{-22}$ [J/Hz] $= 7.80 \times 10^{-4}$ [eV/Hz].

A.3 FREQUENCY SHIFT AND DISSIPATION IMAGES TAKEN ON InAs QDs

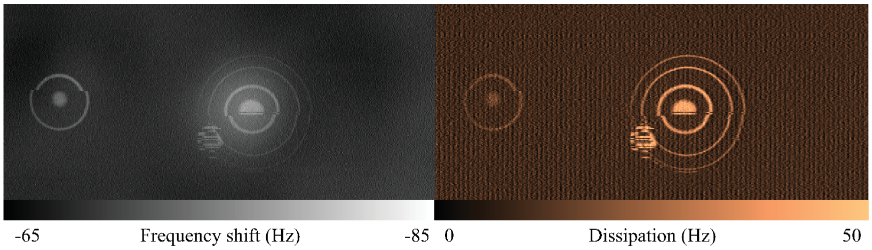

Figure S2: Frequency shift and dissipation images taken on InAs QDs at 4 K. Scanned size is 320 × 320 nm. Oscillation amplitude: 0.5 nm, $V_{\mathrm{B}} = -8$ V.

References

[1] Hylke B. Akkerman, Auke J. Kronemeijer, Paul A. van Hal, Dago M. de Leeuw, Paul W. M. Blom, and Bert de Boer. Self-assembled-monolayer formation of long alkanedithiols in molecular junctions. *Small*, 4(1):100–104, jan 2008. doi: 10.1002/smll.200700623. URL `http://dx.doi.org/10.1002/smll.200700623`.

[2] T. R. Albrecht, P. Grütter, D. Horne, and D. Rugar. Frequency modulation detection using high-q cantilevers for enhanced force microscope sensitivity. *J. Appl. Phys.*, 69(2):668, 1991. doi: 10.1063/1.347347. URL `http://dx.doi.org/10.1063/1.347347`.

[3] F. A. Aldaye, A. L. Palmer, and H. F. Sleiman. Assembling materials with DNA as the guide. *Science*, 321(5897):1795–1799, sep 2008. doi: 10.1126/science.1154533. URL `http://dx.doi.org/10.1126/science.1154533`.

[4] E. Anderson, Z. Bai, C. Bischof, S. Blackford, J. Demmel, J. Dongarra, J. Du Croz, A. Greenbaum, S. Hammarling, A. McKenney, and D. Sorensen. *LAPACK Users' Guide*. Society for Industrial and Applied Mathematics, Philadelphia, PA, third edition, 1999. ISBN 0-89871-447-8 (paperback).

[5] R. C. Ashoori, H. L. Stormer, J. S. Weiner, L. N. Pfeiffer, S. J. Pearton, K. W. Baldwin, and K. W. West. Single-electron capacitance spectroscopy of discrete quantum levels. *Phys. Rev. Lett.*, 68(20):3088–3091, may 1992. doi: 10.1103/physrevlett.68.3088. URL `http://dx.doi.org/10.1103/PhysRevLett.68.3088`.

[6] R. C. Ashoori, H. L. Stormer, J. S. Weiner, L. N. Pfeiffer, K. W. Baldwin, and K. W. West. N -electron ground state energies of a quantum dot in magnetic field. *Phys. Rev. Lett.*, 71(4):613–616, jul 1993. doi: 10.1103/physrevlett.71.613. URL `http://dx.doi.org/10.1103/PhysRevLett.71.613`.

[7] D. V. Averin, A. N. Korotkov, and K. K. Likharev. Theory of single-electron charging of quantum wells and dots. *Phys. Rev. B*, 44(12):6199–6211, sep 1991.

doi: 10.1103/physrevb.44.6199. URL `http://dx.doi.org/10.1103/PhysRevB.44.6199`.

[8] D.V. AVERIN and K.K. LIKHAREV. Single electronics: A correlated transfer of single electrons and cooper pairs in systems of small tunnel junctions. In *Mesoscopic Phenomena in Solids*, pages 173–271. Elsevier BV, 1991. doi: 10.1016/b978-0-444-88454-1.50012-7. URL `http://dx.doi.org/10.1016/B978-0-444-88454-1.50012-7`.

[9] Colin D. Bain, E. Barry Troughton, Yu Tai Tao, Joseph Evall, George M. Whitesides, and Ralph G. Nuzzo. Formation of monolayer films by the spontaneous assembly of organic thiols from solution onto gold. *J. Am. Chem. Soc.*, 111(1): 321–335, jan 1989. doi: 10.1021/ja00183a049. URL `http://dx.doi.org/10.1021/ja00183a049`.

[10] Uri Banin and Oded Millo. T UNNELING AND o PTICAL s PECTROSCOPY OF s EMICONDUCTOR n ANOCRYSTALS. *Annual Review of Physical Chemistry*, 54(1):465–492, oct 2003. doi: 10.1146/annurev.physchem.54.011002.103838. URL `http://dx.doi.org/10.1146/annurev.physchem.54.011002.103838`.

[11] L. Todd Banner, Andrew Richter, and Eugene Pinkhassik. Pinhole-free large-grained atomically smooth au(111) substrates prepared by flame-annealed template stripping. *Surface and Interface Analysis*, 41(1):49–55, jan 2009. doi: 10.1002/sia.2977. URL `http://dx.doi.org/10.1002/sia.2977`.

[12] C. W. J. Beenakker. Theory of coulomb-blockade oscillations in the conductance of a quantum dot. *Phys. Rev. B*, 44(4):1646–1656, jul 1991. doi: 10.1103/physrevb.44.1646. URL `http://dx.doi.org/10.1103/PhysRevB.44.1646`.

[13] Steven D. Bennett, Lynda Cockins, Yoichi Miyahara, Peter Grütter, and Aashish A. Clerk. Strong electromechanical coupling of an atomic force microscope cantilever to a quantum dot. *Phys. Rev. Lett.*, 104(1), jan 2010. doi: 10.1103/physrevlett.104.017203. URL `http://dx.doi.org/10.1103/PhysRevLett.104.017203`.

[14] G. Binnig, H. Rohrer, Ch. Gerber, and E. Weibel. Surface studies by scanning tunneling microscopy. *Phys. Rev. Lett.*, 49(1):57–61, jul 1982. doi: 10.1103/physrevlett.49.57. URL `http://dx.doi.org/10.1103/PhysRevLett.49.57`.

[15] G. Binnig, C. F. Quate, and Ch. Gerber. Atomic force microscope. *Phys. Rev. Lett.*, 56(9):930–933, mar 1986. doi: 10.1103/physrevlett.56.930. URL `http://dx.doi.org/10.1103/PhysRevLett.56.930`.

[16] Shirly Borukhin and Boaz Pokroy. Formation and elimination of surface nanodefects on ultraflat metal surfaces produced by template stripping. *Langmuir*, 27(22):13415–13419, nov 2011. doi: 10.1021/la203596p. URL `http://dx.doi.org/10.1021/la203596p`.

[17] Liraz Chai and Jacob Klein. Large area, molecularly smooth (0.2 nm rms) gold films for surface forces and other studies. *Langmuir*, 23(14):7777–7783, jul 2007. doi: 10.1021/la063738o. URL `http://dx.doi.org/10.1021/la063738o`.

[18] C. E. D. CHIDSEY. Free energy and temperature dependence of electron transfer at the metal-electrolyte interface. *Science*, 251(4996):919–922, feb 1991. doi: 10.1126/science.251.4996.919. URL `http://dx.doi.org/10.1126/science.251.4996.919`.

[19] Christopher E.D. Chidsey, Dominic N. Loiacono, Tycho Sleator, and Sho Nakahara. STM study of the surface morphology of gold on mica. *Surface Science*, 200(1):45–66, jan 1988. doi: 10.1016/0039-6028(88)90432-3. URL `http://dx.doi.org/10.1016/0039-6028(88)90432-3`.

[20] A. A. Clerk. Quantum-limited position detection and amplification: A linear response perspective. *Phys. Rev. B*, 70(24), dec 2004. doi: 10.1103/physrevb.70.245306. URL `http://dx.doi.org/10.1103/PhysRevB.70.245306`.

[21] Aashish A Clerk and Steven Bennett. Quantum nanoelectromechanics with electrons, quasi-particles and cooper pairs: effective bath descriptions and strong feedback effects. *New Journal of Physics*, 7:238–238, nov 2005. doi: 10.1088/1367-2630/7/1/238. URL `http://dx.doi.org/10.1088/1367-2630/7/1/238`.

[22] L. Cockins, Y. Miyahara, S. D. Bennett, A. A. Clerk, S. Studenikin, P. Poole, A. Sachrajda, and P. Grutter. Energy levels of few-electron quantum dots imaged and characterized by atomic force microscopy. *Proceedings of the National Academy of Sciences*, 107(21):9496–9501, may 2010. doi: 10.1073/pnas.0912716107. URL `http://dx.doi.org/10.1073/pnas.0912716107`.

[23] L. Cockins, Y. Miyahara, S. D. Bennett, A. A. Clerk, S. Studenikin, P. Poole, A. Sachrajda, and P. Grutter. Energy levels of few-electron quantum dots imaged and characterized by atomic force microscopy. *Proceedings of the National Academy of Sciences*, 107(21):9496–9501, may 2010. doi: 10.1073/pnas.0912716107. URL `http://dx.doi.org/10.1073/pnas.0912716107`.

[24] Lynda Cockins. *Atomic force microscopy studies on the electrostatic environment and energy levels of self-assembled quantum dots*. PhD thesis, McGill University, 2010.

[25] Lynda Cockins, Yoichi Miyahara, Steven D. Bennett, Aashish A. Clerk, and Peter Grutter. Excited-state spectroscopy on an individual quantum dot using atomic force microscopy. *Nano Letters*, 12(2):709–713, feb 2012. doi: 10.1021/nl2036222. URL `http://dx.doi.org/10.1021/nl2036222`.

[26] J. I. Colless, A. C. Mahoney, J. M. Hornibrook, A. C. Doherty, H. Lu, A. C. Gossard, and D. J. Reilly. Dispersive readout of a few-electron double quantum dot with fast rf gate sensors. *Phys. Rev. Lett.*, 110(4), jan 2013. doi: 10.1103/physrevlett.110.046805. URL `http://dx.doi.org/10.1103/PhysRevLett.110.046805`.

[27] X. D. Cui. Reproducible measurement of single-molecule conductivity. *Science*, 294(5542):571–574, oct 2001. doi: 10.1126/science.1064354. URL `http://dx.doi.org/10.1126/science.1064354`.

[28] Marie-Christine Daniel and Didier Astruc. Gold nanoparticles: assembly, supramolecular chemistry, quantum-size-related properties, and applications toward biology, catalysis, and nanotechnology. *Chemical Reviews*, 104(1):293–346, 2004. doi: 10.1021/cr030698+. URL `http://dx.doi.org/10.1021/cr030698+`. PMID: 14719978.

[29] J.A. DeRose, T. Thundat, L.A. Nagahara, and S.M. Lindsay. Gold grown epitaxially on mica: conditions for large area flat faces. *Surface Science*, 256(1-2): 102–108, oct 1991. doi: 10.1016/0039-6028(91)91204-b. URL `http://dx.doi.org/10.1016/0039-6028(91)91204-B`.

[30] Mark H. Dishner. Preparation of gold thin films by epitaxial growth on mica and the effect of flame annealing. *Journal of Vacuum Science & Technology A:*

Vacuum, Surfaces, and Films, 16(6):3295, nov 1998. doi: 10.1116/1.581536. URL `http://dx.doi.org/10.1116/1.581536`.

[31] U. Dürig, H. R. Steinauer, and N. Blanc. Dynamic force microscopy by means of the phase-controlled oscillator method. *J. Appl. Phys.*, 82(8):3641, 1997. doi: 10.1063/1.365726. URL `http://dx.doi.org/10.1063/1.365726`.

[32] David K Ferry, Stephen M Goodnick, and Jonathan Bird. *Transport in nanostructures*. Cambridge University Press, 2009.

[33] Ian Freestone, Nigel Meeks, Margaret Sax, and Catherine Higgitt. The lycurgus cup — a roman nanotechnology. *Gold Bulletin*, 40(4):270–277, dec 2007. doi: 10.1007/bf03215599. URL `http://dx.doi.org/10.1007/BF03215599`.

[34] A.P. French. *Vibrations and Waves*. W. W. Norton & Company, 1971.

[35] T. Frey, P. J. Leek, M. Beck, J. Faist, A. Wallraff, K. Ensslin, T. Ihn, and M. Büttiker. Quantum dot admittance probed at microwave frequencies with an on-chip resonator. *Phys. Rev. B*, 86(11), sep 2012. doi: 10.1103/physrevb.86.115303. URL `http://dx.doi.org/10.1103/PhysRevB.86.115303`.

[36] R García. Dynamic atomic force microscopy methods. *Surface Science Reports*, 47(6-8):197–301, sep 2002. doi: 10.1016/s0167-5729(02)00077-8. URL `http://dx.doi.org/10.1016/S0167-5729(02)00077-8`.

[37] Franz J. Giessibl. Advances in atomic force microscopy. *Reviews of Modern Physics*, 75(3):949–983, jul 2003. doi: 10.1103/revmodphys.75.949. URL `http://dx.doi.org/10.1103/RevModPhys.75.949`.

[38] C.J Gorter. A possible explanation of the increase of the electrical resistance of thin metal films at low temperatures and small field strengths. *Physica*, 17(8): 777–780, aug 1951. doi: 10.1016/0031-8914(51)90098-5. URL `http://dx.doi.org/10.1016/0031-8914(51)90098-5`.

[39] Katherine C. Grabar, Patrick C. Smith, Michael D. Musick, Jennifer A. Davis, Daniel G. Walter, Michael A. Jackson, Andrea P. Guthrie, , and Michael J. Natan. Kinetic control of interparticle spacing in au colloid-based surfaces: rational nanometer-scale architecture. *Journal of the American Chemical Society*,

118(5):1148–1153, 1996. doi: 10.1021/ja952233+. URL http://dx.doi.org/10.1021/ja952233+.

[40] Hermann Grabert and Michel H. Devoret, editors. *Single Charge Tunneling*. Springer US, 1992. doi: 10.1007/978-1-4757-2166-9. URL http://dx.doi.org/10.1007/978-1-4757-2166-9.

[41] L. Gross, F. Mohn, P. Liljeroth, J. Repp, F. J. Giessibl, and G. Meyer. Measuring the charge state of an adatom with noncontact atomic force microscopy. *Science*, 324(5933):1428–1431, jun 2009. doi: 10.1126/science.1172273. URL http://dx.doi.org/10.1126/science.1172273.

[42] L. Gross, F. Mohn, N. Moll, P. Liljeroth, and G. Meyer. The chemical structure of a molecule resolved by atomic force microscopy. *Science*, 325(5944):1110–1114, aug 2009. doi: 10.1126/science.1176210. URL http://dx.doi.org/10.1126/science.1176210.

[43] Leo Gross. Recent advances in submolecular resolution with scanning probe microscopy. *Nature Chemistry*, 3(4):273–278, apr 2011. doi: 10.1038/nchem.1008. URL http://dx.doi.org/10.1038/nchem.1008.

[44] V. M. Hallmark, S. Chiang, J. F. Rabolt, J. D. Swalen, and R. J. Wilson. Observation of atomic corrugation on au(111) by scanning tunneling microscopy. *Phys. Rev. Lett.*, 59(25):2879–2882, dec 1987. doi: 10.1103/physrevlett.59.2879. URL http://dx.doi.org/10.1103/PhysRevLett.59.2879.

[45] Kimberly Hamad-Schifferli. Stability of dispersions and interactions in nanostructured fluids. In *Colloidal Foundations of Nanoscience*, pages 33–46. Elsevier BV, 2014. doi: 10.1016/b978-0-444-59541-6.00002-3. URL http://dx.doi.org/10.1016/B978-0-444-59541-6.00002-3.

[46] Martin Hegner, Peter Wagner, and Giorgio Semenza. Ultralarge atomically flat template-stripped au surfaces for scanning probe microscopy. *Surface Science*, 291(1-2):39–46, jul 1993. doi: 10.1016/0039-6028(93)91474-4. URL http://dx.doi.org/10.1016/0039-6028(93)91474-4.

[47] B. W. Hoogenboom, P. L. T. M. Frederix, J. L. Yang, S. Martin, Y. Pellmont, M. Steinacher, S. Zäch, E. Langenbach, H.-J. Heimbeck, A. Engel, and H. J. Hug.

A fabry–perot interferometer for micrometer-sized cantilevers. *Appl. Phys. Lett.*, 86(7):074101, 2005. doi: 10.1063/1.1866229. URL `http://dx.doi.org/10.1063/1.1866229`.

[48] Jeeseong Hwang and M. A. Dubson. Atomically flat gold films grown on hot glass. *J. Appl. Phys.*, 72(5):1852, 1992. doi: 10.1063/1.351657. URL `http://dx.doi.org/10.1063/1.351657`.

[49] H. Hölscher, B. Gotsmann, W. Allers, U. Schwarz, H. Fuchs, and R. Wiesendanger. Measurement of conservative and dissipative tip-sample interaction forces with a dynamic force microscope using the frequency modulation technique. *Phys. Rev. B*, 64(7), jul 2001. doi: 10.1103/physrevb.64.075402. URL `http://dx.doi.org/10.1103/PhysRevB.64.075402`.

[50] U Höpfner, Helmut Hehl, and Ludwig Brehmer. Preparation of ordered thin gold films. *Applied Surface Science*, 152(3-4):259–265, nov 1999. doi: 10.1016/s0169-4332(99)00324-4. URL `http://dx.doi.org/10.1016/S0169-4332(99)00324-4`.

[51] L. N. Kantorovich and T. Trevethan. General theory of microscopic dynamical response in surface probe microscopy: From imaging to dissipation. *Phys. Rev. Lett.*, 93(23), nov 2004. doi: 10.1103/physrevlett.93.236102. URL `http://dx.doi.org/10.1103/PhysRevLett.93.236102`.

[52] Yeon Taik Kim, Robin L. McCarley, and Allen J. Bard. Observation of n-octadecanethiol multilayer formation from solution onto gold. *Langmuir*, 9(8):1941–1944, aug 1993. doi: 10.1021/la00032a001. URL `http://dx.doi.org/10.1021/la00032a001`.

[53] N. Kocić, P. Weiderer, S. Keller, S. Decurtins, S.-X. Liu, and J. Repp. Periodic charging of individual molecules coupled to the motion of an atomic force microscopy tip. *Nano Letters*, 15(7):4406–4411, jul 2015. doi: 10.1021/acs.nanolett.5b00711. URL `http://dx.doi.org/10.1021/acs.nanolett.5b00711`.

[54] L. P. Kouwenhoven, A. T. Johnson, N. C. van der Vaart, C. J. P. M. Harmans, and C. T. Foxon. Quantized current in a quantum-dot turnstile using oscillating tunnel barriers. *Phys. Rev. Lett.*, 67(12):1626–1629, sep 1991. doi: 10.1103/physrevlett.67.1626. URL `http://dx.doi.org/10.1103/PhysRevLett.67.1626`.

[55] Leo P. Kouwenhoven, Gerd Schön, and Lydia L. Sohn. Introduction to mesoscopic electron transport. In *Mesoscopic Electron Transport*, pages 1–44. Springer Science + Business Media, 1997. doi: 10.1007/978-94-015-8839-3_1. URL http://dx.doi.org/10.1007/978-94-015-8839-3_1.

[56] A. Labuda, K. Kobayashi, D. Kiracofe, K. Suzuki, P. H. Grütter, and H. Yamada. Comparison of photothermal and piezoacoustic excitation methods for frequency and phase modulation atomic force microscopy in liquid environments. *AIP Advances*, 1(2):022136, 2011. doi: 10.1063/1.3601872. URL http://dx.doi.org/10.1063/1.3601872.

[57] A. Labuda, P. Grutter, Y. Miyahara, W. Paul, and A. ROY-GOBEIL. Methods and systems for optimizing frequency modulation atomic force microscopy, January 21 2015. URL https://www.google.com/patents/EP2825894A1?cl=en. EP Patent App. EP20,130,761,511.

[58] Aleksander Labuda, Yoichi Miyahara, Lynda Cockins, and Peter H. Grütter. Decoupling conservative and dissipative forces in frequency modulation atomic force microscopy. *Phys. Rev. B*, 84(12), sep 2011. doi: 10.1103/physrevb.84.125433. URL http://dx.doi.org/10.1103/PhysRevB.84.125433.

[59] Mong-Tung Lee, Chen-Chan Hsueh, Michael S. Freund, and Gregory S. Ferguson. Air oxidation of self-assembled monolayers on polycrystalline gold: the role of the gold substrate. *Langmuir*, 14(22):6419–6423, oct 1998. doi: 10.1021/la980724c. URL http://dx.doi.org/10.1021/la980724c.

[60] Xinheng Li, Yuhsuke Yasutake, Keijiro Kono, Masayuki Kanehara, Toshiharu Teranishi, and Yutaka Majima. Au nanoparticles chemisorbed by dithiol molecules inserted in alkanethiol self-assembled monolayers characterized by scanning tunneling microscopy. *Jpn. J. Appl. Phys.*, 48(4):04C180, apr 2009. doi: 10.1143/jjap.48.04c180. URL http://dx.doi.org/10.1143/JJAP.48.04C180.

[61] D. Losic, J. G. Shapter, and J. J. Gooding. Influence of surface topography on alkanethiol SAMs assembled from solution and by microcontact printing. *Langmuir*, 17(11):3307–3316, may 2001. doi: 10.1021/la001462t. URL http://dx.doi.org/10.1021/la001462t.

[62] J. Christopher Love, Lara A. Estroff, Jennah K. Kriebel, Ralph G. Nuzzo, and George M. Whitesides. Self-assembled monolayers of thiolates on metals as a form of nanotechnology. *Chemical Reviews*, 105(4):1103–1170, apr 2005. doi: 10.1021/cr0300789. URL `http://dx.doi.org/10.1021/cr0300789`.

[63] Rudolph A. Marcus. Electron transfer reactions in chemistry. theory and experiment. *Reviews of Modern Physics*, 65(3):599–610, jul 1993. doi: 10.1103/revmodphys.65.599. URL `http://dx.doi.org/10.1103/RevModPhys.65.599`.

[64] William E. Martinez, Giuliano Gregori, and Thomas Mates. Titanium diffusion in gold thin films. *Thin Solid Films*, 518(10):2585–2591, mar 2010. doi: 10.1016/j.tsf.2009.07.187. URL `http://dx.doi.org/10.1016/j.tsf.2009.07.187`.

[65] Oded Millo, Uri Banin, YunWei Cao, and David Katz. *Nature*, 400(6744):542–544, aug 1999. doi: 10.1038/22979. URL `http://dx.doi.org/10.1038/22979`.

[66] Fabian Mohn, Leo Gross, Nikolaj Moll, and Gerhard Meyer. Imaging the charge distribution within a single molecule. *Nature Nanotech*, 7(4):227–231, feb 2012. doi: 10.1038/nnano.2012.20. URL `http://dx.doi.org/10.1038/nnano.2012.20`.

[67] Seizo Morita, Franz J. Giessibl, Ernst Meyer, and Roland Wiesendanger, editors. *Noncontact Atomic Force Microscopy*. Springer International Publishing, 2015. doi: 10.1007/978-3-319-15588-3. URL `http://dx.doi.org/10.1007/978-3-319-15588-3`.

[68] David W. Mosley, Brian Y. Chow, and Joseph M. Jacobson. Solid-state bonding technique for template-stripped ultraflat gold substrates. *Langmuir*, 22(6):2437–2440, mar 2006. doi: 10.1021/la052650s. URL `http://dx.doi.org/10.1021/la052650s`.

[69] T. Müller, J. Güttinger, D. Bischoff, S. Hellmüller, K. Ensslin, and T. Ihn. Fast detection of single-charge tunneling to a graphene quantum dot in a multi-level regime. *Appl. Phys. Lett.*, 101(1):012104, 2012. doi: 10.1063/1.4733613. URL `http://dx.doi.org/10.1063/1.4733613`.

[70] Kevin A. Peterlinz and R. Georgiadis. In situ kinetics of self-assembly by surface plasmon resonance spectroscopy. *Langmuir*, 12(20):4731–4740, jan 1996. doi: 10.1021/la9508452. URL `http://dx.doi.org/10.1021/la9508452`.

[71] Albert Putnam, B.L. Blackford, M.H. Jericho, and M.O. Watanabe. Surface topography study of gold deposited on mica using scanning tunneling microscopy: Effect of mica temperature. *Surface Science*, 217(1-2):276–288, jul 1989. doi: 10.1016/0039-6028(89)90549-9. URL `http://dx.doi.org/10.1016/0039-6028(89)90549-9`.

[72] Glenn C. Ratcliff, Dorothy A. Erie, and Richard Superfine. Photothermal modulation for oscillating mode atomic force microscopy in solution. *Appl. Phys. Lett.*, 72(15):1911, 1998. doi: 10.1063/1.121224. URL `http://dx.doi.org/10.1063/1.121224`.

[73] Vishva Ray, Ramkumar Subramanian, Pradeep Bhadrachalam, Liang-Chieh Ma, Choong-Un Kim, and Seong Jin Koh. CMOS-compatible fabrication of room-temperature single-electron devices. *Nature Nanotech*, 3(10):603–608, sep 2008. doi: 10.1038/nnano.2008.267. URL `http://dx.doi.org/10.1038/nnano.2008.267`.

[74] F. Reif. *Fundamentals of statistical and thermal physics*. McGraw-Hill, 1965.

[75] M. Roseman and P. Grütter. Cryogenic magnetic force microscope. *Rev. Sci. Instrum.*, 71(10):3782, 2000. doi: 10.1063/1.1290039. URL `http://dx.doi.org/10.1063/1.1290039`.

[76] Mark Roseman. *Cryogenic magnetic force microscope*. PhD thesis, McGill University, 2000.

[77] Antoine Roy-Gobeil, Yoichi Miyahara, and Peter Grutter. Revealing energy level structure of individual quantum dots by tunneling rate measured by single-electron sensitive electrostatic force spectroscopy. *Nano Letters*, 15(4):2324–2328, apr 2015. doi: 10.1021/nl504468a. URL `http://dx.doi.org/10.1021/nl504468a`.

[78] D. Rugar, H. J. Mamin, and P. Guethner. Improved fiber-optic interferometer for atomic force microscopy. *Appl. Phys. Lett.*, 55(25):2588, 1989. doi: 10.1063/1.101987. URL `http://dx.doi.org/10.1063/1.101987`.

[79] Dmitry A. Ryndyk. *Theory of Quantum Transport at Nanoscale*. Springer International Publishing, 2016. doi: 10.1007/978-3-319-24088-6. URL `http://dx.doi.org/10.1007/978-3-319-24088-6`.

[80] Mark H. Schoenfisch and Jeanne E. Pemberton. Air stability of alkanethiol self-assembled monolayers on silver and gold surfaces. *J. Am. Chem. Soc.*, 120(18):4502–4513, may 1998. doi: 10.1021/ja974301t. URL `http://dx.doi.org/10.1021/ja974301t`.

[81] Frank Schreiber. Structure and growth of self-assembling monolayers. *Progress in Surface Science*, 65(5-8):151–257, nov 2000. doi: 10.1016/s0079-6816(00)00024-1. URL `http://dx.doi.org/10.1016/S0079-6816(00)00024-1`.

[82] C. Schönenberger and S. F. Alvarado. Observation of single charge carriers by force microscopy. *Phys. Rev. Lett.*, 65(25):3162–3164, dec 1990. doi: 10.1103/physrevlett.65.3162. URL `http://dx.doi.org/10.1103/PhysRevLett.65.3162`.

[83] John F. Smalley, Stephen W. Feldberg, Christopher E. D. Chidsey, Matthew R. Linford, Marshall D. Newton, and Yi-Ping Liu. The kinetics of electron transfer through ferrocene-terminated alkanethiol monolayers on gold. *The Journal of Physical Chemistry*, 99(35):13141–13149, aug 1995. doi: 10.1021/j100035a016. URL `http://dx.doi.org/10.1021/j100035a016`.

[84] Lydia L. Sohn, Leo P. Kouwenhoven, and Gerd Schön, editors. *Mesoscopic Electron Transport*. Springer Science + Business Media, 1997. doi: 10.1007/978-94-015-8839-3. URL `http://dx.doi.org/10.1007/978-94-015-8839-3`.

[85] Romain Stomp. *Dissipative and Electrostatic Force Spectroscopy of InAs Quantum Dots by Non-contact Atomic Force Microscopy*. PhD thesis, McGill University, 2005.

[86] Romain Stomp, Yoichi Miyahara, Sacha Schaer, Qingfeng Sun, Hong Guo, Peter Grutter, Sergei Studenikin, Philip Poole, and Andy Sachrajda. Detection of single-electron charging in an individual InAs quantum dot by noncontact atomic-force

microscopy. *Phys. Rev. Lett.*, 94(5), feb 2005. doi: 10.1103/physrevlett.94.056802. URL `http://dx.doi.org/10.1103/PhysRevLett.94.056802`.

[87] Romain Stomp, Yoichi Miyahara, Sacha Schaer, Qingfeng Sun, Hong Guo, Peter Grutter, Sergei Studenikin, Philip Poole, and Andy Sachrajda. Detection of single-electron charging in an individual InAs quantum dot by noncontact atomic-force microscopy. *Phys. Rev. Lett.*, 94(5), feb 2005. doi: 10.1103/physrevlett.94.056802. URL `http://dx.doi.org/10.1103/PhysRevLett.94.056802`.

[88] Venkatesh Subba-Rao, Chandran Sudakar, Jason Esmacher, Mircea Pantea, Ratna Naik, and Peter M. Hoffmann. Improving a high-resolution fiber-optic interferometer through deposition of a TiO[sub 2] reflective coating by simple dip-coating. *Rev. Sci. Instrum.*, 80(11):115104, 2009. doi: 10.1063/1.3244088. URL `http://dx.doi.org/10.1063/1.3244088`.

[89] P. Tangyunyong, R.C. Thomas, J.E. Houston, T.A. Michalske, R.M. Crooks, and A.J. Howard. Substrate effects on the nanometer-scale mechanics of gold films. *Journal of Adhesion Science and Technology*, 8(8):897–912, jan 1994. doi: 10.1163/156856194x00519. URL `http://dx.doi.org/10.1163/156856194X00519`.

[90] S. Tarucha, D. G. Austing, T. Honda, R. J. van der Hage, and L. P. Kouwenhoven. Shell filling and spin effects in a few electron quantum dot. *Phys. Rev. Lett.*, 77(17):3613–3616, oct 1996. doi: 10.1103/physrevlett.77.3613. URL `http://dx.doi.org/10.1103/PhysRevLett.77.3613`.

[91] Antoni Tekiel, Yoichi Miyahara, Jessica M. Topple, and Peter Grutter. Room-temperature single-electron charging detected by electrostatic force microscopy. *ACS Nano*, 7(5):4683–4690, may 2013. doi: 10.1021/nn401840n. URL `http://dx.doi.org/10.1021/nn401840n`.

[92] Antoni Tekiel, Yoichi Miyahara, Jessica M. Topple, and Peter Grutter. Room-temperature single-electron charging detected by electrostatic force microscopy. *ACS Nano*, 7(5):4683–4690, may 2013. doi: 10.1021/nn401840n. URL `http://dx.doi.org/10.1021/nn401840n`.

[93] Leonard. Tender, Michael T. Carter, and Royce W. Murray. Cyclic voltammetric analysis of ferrocene alkanethiol monolayer electrode kinetics based on marcus the-

ory. *Analytical Chemistry*, 66(19):3173–3181, oct 1994. doi: 10.1021/ac00091a028. URL `http://dx.doi.org/10.1021/ac00091a028`.

[94] J. Vancea, G. Reiss, F. Schneider, K. Bauer, and H. Hoffmann. Substrate effects on the surface topography of evaporated gold films—a scanning tunnelling microscopy investigation. *Surface Science*, 218(1):108–126, aug 1989. doi: 10.1016/0039-6028(89)90622-5. URL `http://dx.doi.org/10.1016/0039-6028(89)90622-5`.

[95] Daniel Vanmaekelbergh and Marianna Casavola. Single-dot microscopy and spectroscopy for comprehensive study of colloidal nanocrystals. *J. Phys. Chem. Lett.*, 2(16):2024–2031, aug 2011. doi: 10.1021/jz200713j. URL `http://dx.doi.org/10.1021/jz200713j`.

[96] A. von Schmidsfeld and M. Reichling. Controlling the opto-mechanics of a cantilever in an interferometer via cavity loss. *Appl. Phys. Lett.*, 107(12):123111, sep 2015. doi: 10.1063/1.4931702. URL `http://dx.doi.org/10.1063/1.4931702`.

[97] Peter Wagner, Martin Hegner, Hans-Joachim Guentherodt, and Giorgio Semenza. Formation and in situ modification of monolayers chemisorbed on ultraflat template-stripped gold surfaces. *Langmuir*, 11(10):3867–3875, oct 1995. doi: 10.1021/la00010a043. URL `http://dx.doi.org/10.1021/la00010a043`.

[98] Wenyong Wang, Takhee Lee, and M. A. Reed. Mechanism of electron conduction in self-assembled alkanethiol monolayer devices. *Phys. Rev. B*, 68(3), jul 2003. doi: 10.1103/physrevb.68.035416. URL `http://dx.doi.org/10.1103/PhysRevB.68.035416`.

[99] Wenyong Wang, Takhee Lee, and M. A. Reed. Mechanism of electron conduction in self-assembled alkanethiol monolayer devices. *Phys. Rev. B*, 68(3), jul 2003. doi: 10.1103/physrevb.68.035416. URL `http://dx.doi.org/10.1103/PhysRevB.68.035416`.

[100] Christoph Wasshuber. *Computational Single-Electronics*. Springer Vienna, 2001. doi: 10.1007/978-3-7091-6257-6. URL `http://dx.doi.org/10.1007/978-3-7091-6257-6`.

[101] Emily A. Weiss, George K. Kaufman, Jennah K. Kriebel, Zhefeng Li, Richard Schalek, and George M. Whitesides. Si/SiO 2 -templated formation of ultraflat metal surfaces on glass, polymer, and solder supports: their use as substrates for self-assembled monolayers. *Langmuir*, 23(19):9686–9694, sep 2007. doi: 10.1021/la701919r. URL `http://dx.doi.org/10.1021/la701919r`.

[102] Yongqiang Wen, Christopher K. McLaughlin, Pik Kwan Lo, Hua Yang, and Hanadi F. Sleiman. Stable gold nanoparticle conjugation to internal DNA positions: Facile generation of discrete gold nanoparticle-DNA assemblies. *Bioconjugate Chem.*, 21(8):1413–1416, aug 2010. doi: 10.1021/bc100160k. URL `http://dx.doi.org/10.1021/bc100160k`.

[103] Paul R. Wilkinson and Jon R. Pratt. Analytical model for low finesse, external cavity, fiber fabry–perot interferometers including multiple reflections and angular misalignment. *Appl. Opt.*, 50(23):4671, aug 2011. doi: 10.1364/ao.50.004671. URL `http://dx.doi.org/10.1364/AO.50.004671`.

[104] Trevor M. Willey, Andrew L. Vance, T. van Buuren, C. Bostedt, L.J. Terminello, and C.S. Fadley. Rapid degradation of alkanethiol-based self-assembled monolayers on gold in ambient laboratory conditions. *Surface Science*, 576(1-3):188–196, feb 2005. doi: 10.1016/j.susc.2004.12.022. URL `http://dx.doi.org/10.1016/j.susc.2004.12.022`.

[105] M. T. Woodside. Scanned probe imaging of single-electron charge states in nanotube quantum dots. *Science*, 296(5570):1098–1101, may 2002. doi: 10.1126/science.1069923. URL `http://dx.doi.org/10.1126/science.1069923`.

[106] John T. Woodward, Marlon L. Walker, Curtis W. Meuse, David J. Vanderah, G. E. Poirier, and Anne L. Plant. Effect of an oxidized gold substrate on alkanethiol self-assembly. *Langmuir*, 16(12):5347–5353, 2000. doi: 10.1021/la991672+. URL `http://dx.doi.org/10.1021/la991672+`.

[107] Shinya Yoshida, Takahito Ono, and Masayoshi Esashi. Formation of a flat conductive polymer film using template-stripped gold (TSG) surface and surface-graft polymerization for scanning multiprobe data storage. *e-Journal of Surface Science and Nanotechnology*, 6:202–208, 2008. doi: 10.1380/ejssnt.2008.202. URL `http://dx.doi.org/10.1380/ejssnt.2008.202`.

[108] Jun Zhu, Markus Brink, and Paul L. McEuen. Single-electron force readout of nanoparticle electrometers attached to carbon nanotubes. *Nano Letters*, 8(8): 2399–2404, aug 2008. doi: 10.1021/nl801295y. URL `http://dx.doi.org/10.1021/nl801295y`.

[109] Tao Zhu, Xiaoyi Fu, Tao Mu, Jian Wang, and Zhongfan Liu. pH-dependent adsorption of gold nanoparticles on p -aminothiophenol-modified gold substrates. *Langmuir*, 15(16):5197–5199, aug 1999. doi: 10.1021/la990081g. URL `http://dx.doi.org/10.1021/la990081g`.